

## LOW-SPEED STEEP DESCENT

DANIEL J. DiCARLO

- June 1971

Dr. H. C. Curtiss, Jr.,  
Professor, Dept. of Aerospace  
and Mechanical Sciences

**1174-32439**



## SUMMARY

Lateral-directional dynamic stability derivatives are presented for a 0.1-scale model of the XC-142A tilt-wing transport. The stability derivatives were determined from experiments conducted in the Princeton University Dynamic Track with a dynamically similar model. The tests involved various descending flight conditions achieved at constant speed and wing incidence by varying the vehicle angle of attack. The propeller blade angle and the speed were also changed in the steepest descent case.

The experimental data were analyzed assuming that the dynamic motions of the vehicle may be described by linearized equations, with the lateral-directional characteristics of the full-scale aircraft also presented and discussed. Results from this experimental investigation indicated that the full-scale aircraft would have a stable lateral-directional motion in level flight, with the dynamic motion becoming less stable as the descent angle was increased. No improvement in the dynamics was noted when the propeller blade angle was reduced during the steepest descent, although a subsequent increase in airspeed caused a further degradation in the lateral-directional stability which was characterized by an unstable Dutch-roll oscillation.

## TABLE OF CONTENTS

	Page
SUMMARY . . . . .	ii
ACKNOWLEDGMENT . . . . .	iv
LIST OF FIGURES . . . . .	v
LIST OF SYMBOLS . . . . .	ix
INTRODUCTION . . . . .	1
DESCRIPTION OF APPARATUS AND EXPERIMENTS . . . . .	3
EXPERIMENTAL RESULTS . . . . .	7
FULL-SCALE AIRCRAFT DYNAMICS . . . . .	13
CONCLUSIONS . . . . .	22
APPENDICES	
I. ANALYSIS OF DATA . . . . .	23
II. FULL-SCALE CONVERSION . . . . .	38
REFERENCES . . . . .	46

## ACKNOWLEDGMENT

The author wishes to express his gratitude to Professor H. C. Curtiss, Jr. for his technical advice, stimulating influence, and continual encouragement during the pursuit of this research. Appreciation is also extended to the personnel of the Dynamic Model Track, particularly Messrs. W. F. Putman and J. V. Lebacqz, for their most useful and capable advice. In addition, the author is grateful for the NASA grant and the Princeton University Assistantship in Research which made possible his graduate studies.

## LIST OF FIGURES

	Page
1 Full scale stability derivatives . . . . .	62
2 Princeton Dynamic Model Track longitudinal mount with one-tenth scale dynamically similar model . . . . .	65
3 Princeton Dynamic Model Track lateral/directional mount with one-tenth scale dynamically similar model . . . . .	66
4 Schematic representation of lateral carriage system, model support, and gimbal arrangement . . . . .	67
5 0.10 scale dynamic model of XC-142A tilt-wing V/STOL aircraft . . . . .	68
6 General arrangement, 0.10 scale XC-142A model . . . . .	69
7 Model wing airfoil section, showing slat, flap, and aileron arrangement . . . . .	70
8 Diagram for resolution of model forces from static test data . . . . .	71
9 Static test data; descent condition determination. Ramp input to roll attitude-hold loop. $\beta_{.75R} = 13.5^\circ$ , $\delta_a = 0$ , and $\Delta\beta = 0$ . . . . .	72
10 Static test data; descent condition determination. Ramp input to pitch attitude-hold loop. $\beta_{.75R} = 13.5^\circ$ , $\delta_a = 0$ , and $\Delta\beta = 0$ . . . . .	73
11 Static test data; descent condition determination. Ramp velocity input. $\beta_{.75R} = 11.5^\circ$ , $\delta_a = 0$ , and $\Delta\beta = 0$ . . . . .	74
12 Dynamic test data; directional transient response. One degree-of-freedom, $\psi$ . $\theta = 0$ , $\beta_{.75R} = 13.5^\circ$ , and $\gamma = 0$ ( $U_f = 17.8$ and 0 ft/sec for runs 91 and 92, respectively). . . . .	75

## LIST OF FIGURES (Continued)

	Page
13 Dynamic test data; directional transient response. One degree-of-freedom, $\psi, \theta = 0$ , $\beta_{.75R} = 13.5^\circ$ , $\gamma = 0$ , and $U_f = 19.4$ ft/sec . . . . .	76
14 Dynamic test data; lateral/directional transient response. Two degrees-of-freedom, $\phi-\psi$ . $\theta = 0$ , $\beta_{.75R} = 13.5^\circ$ , $\gamma = 0$ , and $U_f = 17.6$ ft/sec . . . . .	77
15 Dynamic test data; lateral/directional transient response. Two degrees-of-freedom, $\phi-v_f$ . $\theta = 0$ , $\beta_{.75R} = 13.5^\circ$ , $\gamma = 0$ , and $U_f = 18.4$ ft/sec . . . . .	78
16 Dynamic test data; lateral/directional transient response. Three degrees-of-freedom, $\phi-\psi-v_f$ . $\theta = 0$ , $\beta_{.75R} = 13.5^\circ$ , $\gamma = 0$ , and $U_f = 17.9$ ft/sec . . . . .	79
17 Dynamic test data; lateral/directional transient response. One degree-of-freedom, $\psi$ . $\theta = 10^\circ$ , $\beta_{.75R} = 13.5^\circ$ , $\gamma = -5^\circ$ , and $U_f = 17.8$ ft/sec . . . . .	80
18 Dynamic test data; lateral/directional transient response. Two degrees-of-freedom, $\phi-\psi$ . $\theta = 10^\circ$ , $\beta_{.75R} = 13.5^\circ$ , $\gamma = -5^\circ$ , and $U_f = 17.7$ ft/sec . . . . .	81
19 Dynamic test data; lateral/directional transient response. Two degrees-of-freedom, $\phi-v_f$ . $\theta = 10^\circ$ , $\beta_{.75R} = 13.5^\circ$ , $\gamma = -5^\circ$ , and $U_f = 17.6$ ft/sec . . . . .	82
20 Dynamic test data; lateral/directional transient response. Three degrees-of-freedom, $\phi-\psi-v_f$ . $\theta = 10^\circ$ , $\beta_{.75R} = 13.5^\circ$ , $\gamma = -5^\circ$ , and $U_f = 18.4$ ft/sec . . . . .	83
21 Dynamic test data; lateral/directional transient response. One degree-of-freedom, $\psi$ . $\theta = 20^\circ$ , $\beta_{.75R} = 13.5^\circ$ , $\gamma = -11^\circ$ , and $U_f = 18.6$ ft/sec . . . . .	84
22 Dynamic test data; lateral/directional transient response. Two degrees-of-freedom, $\phi-\psi$ . $\theta = 20^\circ$ , $\beta_{.75R} = 13.5^\circ$ , $\gamma = -11^\circ$ , and $U_f = 18.6$ ft/sec . . . . .	85
23 Dynamic test data; lateral/directional transient response. Two degrees-of-freedom, $\phi-v_f$ . $\theta = 20^\circ$ , $\beta_{.75R} = 13.5^\circ$ , $\gamma = -11^\circ$ , and $U_f = 18.4$ ft/sec . . . . .	86

## LIST OF FIGURES (continued)

	Page
24 Dynamic test data; lateral/directional transient response. Three degrees-of-freedom, $\phi$ - $\psi$ - $v_f$ . $\theta = 20^\circ$ , $\beta_{.75R} = 13.5^\circ$ , $\gamma = -11^\circ$ , and $U_f = 18.4$ ft/sec . . . . .	87
25 Dynamic test data; lateral/directional transient response. One degree-of-freedom, $\psi$ . $\theta = 20^\circ$ , $\beta_{.75R} = 11.5^\circ$ , $\gamma = -11^\circ$ , and $U_f = 18.1$ ft/sec . . . . .	88
26 Dynamic test data; lateral/directional transient response. Two degrees-of-freedom, $\phi$ - $\psi$ . $\theta = 20^\circ$ , $\beta_{.75R} = 11.5^\circ$ , $\gamma = -11^\circ$ , and $U_f = 18.8$ ft/sec . . . . .	89
27 Dynamic test data; lateral/directional transient response. Two degrees-of-freedom, $\phi$ - $v_f$ . $\theta = 20^\circ$ , $\beta_{.75R} = 11.5^\circ$ , $\gamma = -11^\circ$ , and $U_f = 18.4$ ft/sec . . . . .	90
28 Dynamic test data; lateral/directional transient response. One degree-of-freedom, $\psi$ . $\theta = 20^\circ$ , $\beta_{.75R} = 11.5^\circ$ , $\gamma = -11^\circ$ , and $U_f = 23.5$ ft/sec . . . . .	91
29 Dynamic test data; lateral/directional transient response. Two degrees-of-freedom, $\phi$ - $\psi$ . $\theta = 20^\circ$ , $\beta_{.75R} = 11.5^\circ$ , $\gamma = -11^\circ$ , and $U_f = 24$ ft/sec . . . . .	92
30 Dynamic test data; lateral/directional transient response. Two degrees-of-freedom, $\phi$ - $v_f$ . $\theta = 20^\circ$ , $\beta_{.75R} = 11.5^\circ$ , $\gamma = -11^\circ$ , and $U_f = 23.6$ ft/sec . . . . .	93
31 Dynamic test data; lateral/directional transient response. Three degrees-of-freedom, $\phi$ - $\psi$ - $v_f$ . $\theta = 20^\circ$ , $\beta_{.75R} = 11.5^\circ$ , $\gamma = -11^\circ$ , and $U_f = 23.6$ ft/sec . . . . .	94
32 Summary of model transient response data. ( $\sigma + j\omega_d$ only root shown.) . . . . .	95
33 Model axes systems and variables for lateral/directional descent tests . . . . .	96
34 Transformation of linear velocities from space-fixed to stability axis system for tilt-wing model gimbal system . . . . .	97
35 Relationship between the $\phi$ and $\psi$ time vectors and their derivatives for case 1. $\theta = 0$ , $\beta_{.75R} = 13.5^\circ$ , $\gamma = 0$ , and $U_f = 17.6$ ft/sec . . . . .	98

## LIST OF FIGURES (continued)

	Page
36 Yawing moment vector polygon (Dutch-roll oscillation) representing two degrees-of-freedom ( $\phi$ - $\psi$ ) model data for case 1. $\theta = 0$ , $\beta_{.75R} = 13.5^\circ$ , $\gamma = 0$ , and $U_f = 17.6$ ft/sec . . . . .	99
37 Rolling moment vector polygon (Dutch-roll oscillation) representing two degrees-of-freedom ( $\phi$ - $\psi$ ) model data for case 1. $\theta = 0$ , $\beta_{.75R} = 13.5^\circ$ , $\gamma = 0$ , and $U_f = 17.6$ ft/sec . . . . .	100
38 Characteristic roots of the full-scale aircraft motion for each test case . . . . .	101



## LIST OF SYMBOLS

$A_T$	lift curve slope of vertical tail, per radian
cg	aircraft center-of-gravity location
F.S.	fuselage station (horizontal reference), inches
$g$	acceleration due to gravity, feet per second squared
$i_w, i_t$	wing incidence and tail incidence, respectively, degrees
$I_x$	moment of inertia in roll about principal axis, slug-feet squared
$I_z$	moment of inertia in yaw about principal axis, slug-feet squared
$I_{xz}$	product of inertia with respect to roll and yaw principal axes, slug-feet squared
$I_x'$	moment of inertia in roll about gimbal axis, slug-feet squared
$I_z'$	moment of inertia in yaw about gimbal axis, slug-feet squared
$j$	$= \sqrt{-1}$
$K_{\psi_m}$	mechanical spring constant in yaw, foot-pounds per radian (negative for normal spring restoring moment sense)
$l_T$	distance from c.g. to vertical tail, feet
$L$	aerodynamic rolling moment, foot-pounds
$L_{\dot{\psi}}, L_{\dot{\phi}}, L_{\dot{\psi}}, L_{\dot{\phi}}$	rate of change of gimbal axis rolling moment with respect to variable indicated in subscript, divided by $I_x'$
$L_v, L_p, L_r$	rate of change of body axis rolling moment with respect to variable indicated in subscript, divided by $I_x$
$M$	aerodynamic pitching moment, foot-pounds
MAC	mean aerodynamic chord of the wing

$m$	general aerodynamic mass term, slugs
$m'$	equivalent aerodynamic mass of the model, $\left(-\frac{Z}{g}\right)$ , slugs
$m_l$	mass of lateral travel link, slugs ( $m_l = 0.17$ slugs)
$m_p$	pivot mass of model, slugs. ( $m_p = 1.42$ slugs)
$m_t$	total traveling mass of the model, slugs ( $m_t = m_p + m_l$ )
$N$	aerodynamic yawing moment, foot-pounds
$N_{V_f}, N_{\phi}, N_{\dot{\phi}},$ $N_{\psi}, N_{\dot{\psi}}$	rate of change of gimbal axis yawing moment with respect to variable indicated in subscript, divided by $I_z'$
$N_v, N_p, N_r$	rate of change of body axis yawing moment with respect to variable indicated in subscript, divided by $I_z$
$P_{xz}$	product of inertia with respect to roll and yaw gimbal axes, slug-feet squared
$p$	roll rate about body axis, radians per second
$q$	pitch rate about body axis, radians per second or, dynamic pressure, $= \frac{1}{2} \rho U_{of}^2$
$r$	yaw rate about body axis, radians per second
rpm	model propeller rotational speed, revolutions per minute
$S_T$	tail wing area, square feet
$S$	$= \sigma \pm j\omega_d$ , root of characteristic equation, per second
$T_2$	time required for exponential function to double amplitude, seconds
$T_{1/2}$	time for exponential function to half its amplitude, seconds
$U$	aircraft velocity along principal X-axis, feet per second
$U_f$	aircraft horizontal velocity (space-fixed axis system), feet per second

$U_0$	aircraft initial velocity along principal X-axis, feet per second
$U_{0f}$	aircraft initial horizontal velocity (space-fixed axis system), feet per second
$u$	aircraft horizontal perturbation velocity (principal axis system), feet per second
$u_f$	aircraft horizontal perturbation velocity (space-fixed axis system), feet per second
$V$	aircraft lateral velocity along principal Y-axis, feet per second
$V_f$	aircraft lateral velocity (space-fixed axis system), feet per second
$V_0$	aircraft initial lateral velocity along principal Y-axis, feet per second
$V_{0f}$	aircraft initial lateral velocity (space-fixed axis system), feet per second
$v$	aircraft lateral perturbation velocity (principal axis system), feet per second
$v_f$	aircraft lateral perturbation velocity (space-fixed axis system), feet per second
$W$	model weight, pounds; or aircraft velocity along principal Z-axis, feet per second
$W_f$	aircraft vertical velocity (space-fixed axis system), feet per second
$W_0$	aircraft initial vertical velocity along principal Z-axis, feet per second
$W_{0f}$	aircraft initial vertical velocity (space-fixed axis system), feet per second
$W_p$	model pivot weight, pounds ( $W_p = 45.9$ pounds)
$w$	aircraft vertical perturbation velocity (principal axis system), feet per second
$w_f$	aircraft vertical perturbation velocity (space-fixed axis system), feet per second

X	longitudinal force measured by strain gage, pounds
X"	body fixed longitudinal axis, after second Euler rotation, that coincides with model gimbal axis
X <sub>f</sub>	longitudinal horizontal axis (space-fixed axis system)
$\bar{X}$	longitudinal principal body axis, after final Eulerian transformation
X <sub>cg</sub>	longitudinal position of model c.g., percent mean aerodynamic chord
Y	sideforce measured by strain gage, pounds
Y"	body fixed lateral axis after second Euler rotation
Y <sub>f</sub>	lateral axis (space-fixed axis system)
$\bar{Y}$	lateral principal body axis
Z	vertical aerodynamic force in steady flight, pounds
Z"	body fixed vertical axis after second Euler rotation
Z <sub>f</sub>	vertical space axis that coincides with model gimbal axis
Z <sub>cg</sub>	vertical distance of model c.g. from wing
$\bar{Z}$	vertical principal body axis
$\alpha$	model angle of attack (equals model space-axis pitch angle, $\theta$ ) degrees
$\beta$	local collective propeller blade angle, degrees
$\beta_{.75R}$	average collective blade pitch angle, for four propellers measured at the three-quarter radius, degrees
$\gamma$	descent angle, degrees (positive for climbing flight)
$\delta_{a_p}, \delta_{a_s}$	port and starboard aileron deflection, degrees (positive for aileron trailing edge forward with $i_v = 90^\circ$ )
$\delta_f$	flap deflection, degrees

$\Delta\beta_p, \Delta\beta_s$	differential collective pitch on port and starboard propellers, respectively, degrees (averaged for two propellers)
$\zeta$	damping ratio, or angle between model principal and gimbal axes, degrees (Note: $\zeta = \theta$ , when $\eta = 0$ )
$\eta$	angle between model principal axis and fuselage reference line, degree (assumed = 0)
$\theta$	pitch angle about the model gimbal pitch axis (equal to model $\alpha$ ) degrees, or radians
$\theta_a$	aerodynamic pitch attitude, relative to the fictitious horizon that results from the test procedure, degrees or radians
$\lambda$	linear scale factor, $\lambda = \frac{\text{model length}}{\text{full-scale length}}$
$\rho$	air density, slugs per cubic foot
$\sigma$	real part of "S" (damping), per second
$\phi$	roll angle about the model gimbal roll axis, degrees or radians
$\psi$	yaw angle about model gimbal yaw axis, degrees or radians
$\omega_d$	imaginary part of "S" (damped frequency), per second
$(\dot{\phantom{x}})$	differentiation with respect to time
$(\phantom{x})', (\phantom{x})''$	perturbed locations of axes
$(\phantom{x})_B, (\phantom{x})_G$	body and gimbal axis value, respectively

## INTRODUCTION

During the past decade, there has been an ever-increasing interest in the V/STOL type of aircraft, not only because of their unique and intriguing addition to the field of aerodynamics, but also because of the potential offered by these aircraft in a commercial and military role. An assortment of V/STOL configurations have been tunnel tested, including tilt-prop, compound, jet-lift, tilt-wing, and many other concepts (refs. 1 through 9). Such configurations offering promise, either have been built and flight tested, or are currently involved in a flight research program (refs. 10 through 18). Most of this work, though, has been of a general exploratory nature, directed towards either pure aerodynamics or establishing the overall feasibility of the various concepts. Investigations to document the classical stability derivatives, which are a prime ingredient affecting the so-called handling qualities of the vehicle, have been limited.

To make this stability derivative data available, a number of V/STOL configurations have been tunnel tested in the Princeton University Dynamic Model Track (refs. 5 to 7, and 19 to 21). One of the more recent vehicles tested has been a 0.1-scale model of the four-propeller XC-142A tilt-wing transport. Experimental results have included the first quantitative information published on the lateral-directional dynamic derivatives of a tilt-wing V/STOL aircraft at low forward speed (see ref. 19) and the longitudinal dynamic stability characteristics (see ref. 20).

The purpose of this study was to extend the information presented

in the previous Princeton University reports dealing with the XC-142A. Direct quantitative measurements were made of the lateral-directional transient response time histories for various trim conditions simulating low-speed, descending flight. These data were taken at five test conditions representing various combinations of pitch attitude ( $\theta$ ), forward velocity ( $U_F$ ), and propeller blade angle ( $\beta$ ). The wing incidence and wing flap angle were fixed at  $40^\circ$  and  $60^\circ$ , respectively, throughout the entire investigation. The results presented in this report thus represent the first documentation of the stability derivatives for a tilt-wing V/STOL transport in descending flight.

The servo-analysis techniques used to determine the stability derivatives from the data available are described in appendix I. Conversion of the data to full-scale values is discussed in appendix II, with the results shown in figure 1. Additional information regarding the static characteristics and control effectiveness for the configuration tested, are presented in reference 22.

## DESCRIPTION OF APPARATUS AND EXPERIMENTS

TEST FACILITY

The Princeton University Dynamic Model Track Facility was designed explicitly for the study of the dynamic stability and control of helicopter and V/STOL models for speeds ranging from hover through transition. Integral components of the test facility include: a 750-foot track, servo-drive carriage, model mounts, measuring transducers and recording equipment, all of which are located in a building with a test cross section of 30 by 30 feet. The dynamic carriage, which can follow the longitudinal velocity excursions of the model, has an acceleration potential of 0.6g and a maximum speed of 40 feet per second. A detailed description of the facility and testing techniques employed may be found in reference 23.

Two of the various methods used to mount models to the carriage permit separate measurement of the classical longitudinal and lateral-directional degrees of dynamic motion. The longitudinal mount, shown in figure 2, permits horizontal and vertical motions of the model relative to the carriage and allows the model to rotate in the plane determined by these directions. The horizontal motion is sensed and used to command the carriage to follow the model in a closed-loop fashion. Similarly, the vertical displacement of the model commands the boom to follow in the vertical direction. The lateral-directional mount which was used for this study is shown in figure 3. This mount permits relative motion between the model support linkage and the



lateral servo-driven carriage to be sensed and used to position the lateral carriage along the lateral boom. A maximum sideward excursion of 8 feet is permitted by this arrangement. The yaw degree-of-freedom is provided by a pivot mounting which allows angular rotation of the vertical tube supporting the model relative to the lateral servo-driven carriage. Roll freedom is achieved by a pivot mounting located within the fuselage of the model itself which permits the angular motion in roll relative to the fixed vertical support tube. A schematic drawing of the lateral-directional mount is shown in figure 4. Overall, the model support and gimbal system allows particular degrees of angular freedom to be selected. Those not under investigation are locked by a braking system which also serves to arrest the model motions at the end of a test run. The gimbal and support systems also serve as references for measurement of the model motions. This system is similar to the one used in reference 19, with the roll and yaw axes fixed to the lateral error linkage; the roll axis yaws but does not pitch with the model, while the pitch axis remains fixed to the model. For the present study, the descent conditions were simulated by altering the pitch attitude of the model with respect to the carriage. This adjustment results in an increased aircraft angle of attack since the carriage velocity is always horizontal. The exact expressions for the variables and the appropriate equations of motion for this axis system are presented in appendix I.

The dynamic experiments conducted during this study were, for the most part, two degree-of-freedom motions achieved by use of the

lateral-directional mount. These tests included single degree-of-freedom in yaw ( $\psi$ ) and two degree-of-freedom in roll and yaw ( $\phi - \psi$ ) angular motions, and roll angle and sideward velocity ( $\phi - v_f$ ) motions for selected combinations of pitch attitude ( $\theta$ ), forward velocity ( $U_f$ ) and propeller blade angle ( $\beta$ ). Three degree-of-freedom cases ( $\phi - \psi - v_f$ ) were also conducted to analyze the complete lateral-directional motions of the aircraft.

The Princeton Model Track Facility can also be used to measure static stability derivatives. The model is mounted rigidly to the carriage permitting the forces and moments acting on the model to be measured with strain gauges. Continuous changes in the variables of interest can be achieved by programming the model or carriage motions. Although similar to wind-tunnel testing, a uniform air velocity, free from turbulence, is offered in the 30 by 30 foot test section. Precise control of speed is available over a wide range, which includes not only forward flight but hover and rearward flight as well.

#### MODEL

The 0.10 scale dynamically similar model constructed for this experiment is shown in figure 5; drawings of the general arrangement and of the airfoil section of the model are shown in figures 6 and 7. The model is the one used for the lateral-directional study of reference 19, with several modifications. These modifications of the model, and descriptions of the lateral-directional control system, geometric characteristics of the model propellers, ailerons, and other pertinent information are presented in reference 22.

INSTRUMENTATION

The basic test instrumentation, employing telemetering and magnetic tape recordings, was similar to that used in reference 19. However, several additions and refinements were made to the model instrumentation: these changes are also noted in the data report relating to this experiment (ref. 22).

## EXPERIMENTAL RESULTS

STATIC DATA

Measurements of the horizontal force (parallel to the free-stream) and the vertical force (perpendicular to the free-stream) were made to determine the descent conditions realized during this program. All data were taken in the forward flight mode for a constant wing incidence,  $i_w = 40^\circ$ , and constant flap deflection,  $\delta_f = 60^\circ$ .

Generally, the aerodynamic forces are functions of the forward velocity ( $U_f$ ), vertical velocity ( $W_f$ ), pitch angle ( $\theta$ ), blade collective pitch angle ( $\beta$ ), and the control inputs. However, for the XC-142A model, there was no cyclic pitch control and, the ailerons, differential collective, etc., were assumed to affect only the lateral-directional equilibrium. Therefore, for a space-fixed axis system, the force equations for steady level trimmed flight are:

$$\left. \begin{aligned} X_f(U_f, W_f, \theta, \beta) &= 0 \\ Z_f(U_f, W_f, \theta, \beta) &= mg \end{aligned} \right\} \quad (1)$$

Since a space-fixed axis system is being considered, the descent angle ( $\gamma$ ) is defined by:

$$\tan \gamma = \frac{W_f}{U_f} \quad (2)$$

However, because of the mechanization of the testing apparatus, it was not possible to program descent velocities into the model, that is,  $W_f = 0$ .

Therefore, the descent conditions were simulated by rotating the model about its pitch axis, thus stipulating that the test or true model pitch attitude ( $\theta$ ) was precisely the model angle of attack ( $\alpha$ ), as shown on figure 8. For each of the test cases studies, this pitch attitude remained constant. Force balance considerations were then used to define the actual descent angle, by,

$$Z_F \sin \gamma = X_F \cos \gamma \quad (3)$$

or

$$\tan \gamma = \frac{X_F}{Z_F}$$

Since the horizontal velocity of the model is determined by programming the carriage, it is not necessary in the model tests that the horizontal forces be in balance.

It should be noted that the model was constrained to fly parallel to the horizon along the space X-axis, (i.e., the test track), thus, simulating an inclined horizon as shown on figure 8, rather than an actual descending flight path. Since the horizon is so inclined, an aerodynamic pitch attitude ( $\theta_a$ ) can be defined as the angle between this artificial horizon and the body principal X-axis, again noted on figure 8. This will be the pitch angle of the aircraft in descending flight.

The space axis longitudinal force ( $X_F$ ) was measured directly by a strain gauge, thus known for the various combinations of  $U_F$ ,  $\theta$ , and  $\beta$ . Direct measurement of the space-axis vertical force ( $Z_F$ ) was

not available. To determine  $Z_f$ , the model was rolled through  $\phi$  degrees as shown in figure 8, and the horizon referenced side force ( $Y$ ) measured. The relationship for obtaining the space vertical force is then

$$Z_f = \frac{Y}{\sin \phi} = \frac{Y}{\phi} \quad \begin{array}{l} \text{(for small angle} \\ \text{approximation)} \end{array} \quad (4)$$

When substituted into the descent angle equation, this yields:

$$\gamma = \tan^{-1} \frac{X_f}{Y} (U_f, \theta, \beta) \phi \quad (5)$$

Samples of the static data used to determine the horizontal and vertical forces, and thus the descent angles, for each test case are shown in figures 9 through 11. A summary of the test conditions, including the descent angles computed by the above equation, and the aerodynamic pitch angle ( $\theta_a$ ) are presented in table I, with the model geometric and inertia characteristics outlined in table II. The details of other pertinent procedures and testing techniques applicable to this study, regarding the stability augmentation used on the model, model trim, and aileron effectiveness, are discussed in reference 22.

#### DYNAMIC DATA

##### Single-Degree-of-Freedom

Single-degree-of-freedom dynamic responses were evaluated for each of the five cases to determine the yaw damping ( $N_{\dot{\psi}}$ ) and the moment of inertia about the yaw axis ( $I_z$ ). For these runs, the model

was locked in roll. Mechanical springs were attached between the model and support tube to provide a restoring moment about the yaw axis. The equation of motion for the rigid-body oscillation of the model in yaw, with mechanical springs, aerodynamic damping, and mounting friction is:

$$I_z \ddot{\psi} + \left( \frac{\partial N}{\partial \dot{\psi}} + \text{friction} \right) \dot{\psi} + \frac{\partial N}{\partial \psi} \psi = 0 \quad (6)$$

For these experiments, the model mounting friction was determined from power-off tests. The mechanical spring contribution,  $\frac{\partial N}{\partial \psi} = K_{\psi m}$ , was calibrated separately and found to be (-31.7 ft-lb/rad). Spring-restrained single-degree-of-freedom runs were also performed with the model motors off and the carriage velocity equal to zero ( $U_f = \text{rpm} = 0$ ) to determine the model yaw moment of inertia. The yaw damping runs were conducted by releasing the model, with propellers running, from an initial yaw angle offset. An example of the resulting time history plus one for the model motors off are shown in figure 12. These time histories, along with the knowledge of the spring constant and moment of inertia, provided the total aerodynamic plus mechanical spring damping. The mechanical damping, as determined from model motors off data, was simply subtracted out, resulting in the true aerodynamic damping for the first case. Since the model exhibited stable directional stability in the first test condition, the mechanical springs were not used during the remaining descent cases. It should be noted that no single-degree-of-freedom runs were made to determine the roll damping and roll moment of inertia. As an approximation, therefore, the ratio of the moment of inertia in yaw for this experiment to that

of reference 19 was used to determine the roll moment of inertia. Furthermore, the roll damping moment for the level flight case of this investigation was assumed to be equal to the value determined in the level case ( $i_w = 30^\circ$ ) of reference 19, resulting in the slightly lower ratio of roll damping to inertia (hereafter simply the roll angular rate damping). A summary of the single-degree-of-freedom data for the test runs analyzed for each case is presented in table III.

#### Multiple Degree of Freedom

For each of the descent cases, lateral-directional transient response measurements were conducted for the following degrees of freedom: two degrees of freedom in roll and yaw ( $\phi - \psi$ ); two degrees of freedom in roll and sideward velocity ( $\phi - v_f$ ); three degrees of freedom in roll, yaw and sideward velocity ( $\phi - \psi - v_f$ ). The equations of motion for each of these conditions are presented in appendix I. No mechanical springs were used for any of the multiple-degree-of-freedom tests, and for the data presented, only pitching motions were stability augmented.

The procedure followed during one of these multiple-degree-of-freedom tests was to bring the model motors up to speed with the model locked, relative to the boom, on the stationary carriage. The carriage was accelerated to the trim speed, and timers were used to unlock the mechanical restraints of the desired degrees of freedom. The model was then permitted to fly freely in any desired combination of degrees of freedom. For some of the runs, either a roll or heading offset, or control deflections were used as an input to excite the



model's response, though in some cases a small random disturbance was sufficient to start the motion due to the unstable nature of the dynamics.

Sample results of the lateral-directional dynamic tests for the five cases, which include level flight, are presented in figures 12 through 31 as time histories of the transient response of the model. The period of the motion and the damping ratio for each of the multiple-degree-of-freedom runs analyzed is presented for each case in table IV, with the corresponding roots of the model transient responses summarized in figure 32.

## FULL-SCALE AIRCRAFT DYNAMICS

The analysis of the experimental results, as discussed in appendix I, along with the application of the scale factors discussed in appendix II, permitted the full-scale, body axes stability derivatives to be determined. These stability derivatives are presented in figure 1 as a function of descent angle. The dashed curves indicate the probable trends of the derivatives, as determined from test cases 1, 2, and 3. The effects of a change in the propeller blade angle ( $\beta$ ), case 4, and subsequent change in the forward velocity ( $U_f$ ), case 5, are also shown in figure 1, by the rectangular and triangular symbols respectively. Also noted in figure 1 are the results from reference 25, which will be discussed later as applied to the level flight case. The data resulting from descent angle changes, cases 1, 2, and 3, will be discussed separately from the data representing aerodynamic changes, cases 4 and 5.

DESCENDING FLIGHT RESULTS

The descending flight results were those obtained from cases 1 through 3. The descent angle obtained by varying fuselage angle of attack was the only variable for these three cases and were:  $0^\circ$  (level),  $-5^\circ$ ,  $-11^\circ$ , respectively. From the data analyzed, the body axis stability derivatives were computed and the following may be noted for each.

Roll Damping ( $L_p$ )

A mathematical approximation was employed to determine the roll angular rate damping of the model, as a function of descent angle, because no single-degree-of-freedom roll data was available. It was

not known whether the roll damping would increase or decrease as the descent angle steepened, therefore, variations in both directions were analyzed. The results showed that an increase in the space axis roll damping (as would have been measured from the track data) caused the body axis values to increase unrealistically for the higher descent angles. On the other hand, a reduction in the space axis roll damping, for higher descent angles, resulted in a slight increase in the final body axis value, as shown in figure 1, cases 1 to 3. This trend in the roll rate damping was acceptable because these values, along with the other stability derivatives involved, were consistent with the dynamic motions measured for these descent cases. Such a variation in the roll damping was also considered reasonable because it can be attributed to an increase in lift on the wings, at the higher angles of attack associated with these steeper descent angles, a condition that would be expected prior to wing stall.

#### Yaw Moment Due to Roll Rate ( $N_p$ )

This cross derivative is negative - the sign generally associated with conventional aircraft (ref. 24) - resulting from the unsymmetric lift distribution on the wings while the aircraft is rolling. The magnitude remains somewhat constant, though falls off slightly at the higher descent angle. This reduction may be attributed to a smaller tail contribution and/or unsymmetrical stall effects on a tilt-wing configuration that is rolling during descending flight.

### Yaw Damping ( $N_r$ )

This stability derivative is stable for level flight and becomes less stable as the descent angle increases. For the largest descent angle, in fact, the damping becomes very slightly unstable (positive) which arises, most likely, from interference on the vertical tail particularly at the low speeds being investigated.

### Roll Moment Due to Yaw Rate ( $L_r$ )

The rolling moment due to yaw rate is another cross derivative which has a sign (positive) that is typical for conventional aircraft (ref. 24). The value of the derivative decreases for the first descent case ( $-5^\circ$ ) but increases positively for the higher descent case. The explanation of this trend appears somewhat difficult and is probably the result of the complex airflow interplay between the wing and tail surfaces.

### Dihedral Effect ( $L_v$ )

This stability derivative exhibited a stable (negative) tendency for all the descent cases analyzed. Its value is large for the level flight case - comparable to that found in reference 19 and becomes less stable as the descent angle increases. This trend may be caused by an onset of stall on the advancing wing, permitting the opposite wing's lift to become more effective with descent angle.

### Directional Stability ( $N_v$ )

The sign of this stability derivative indicates the aircraft is directionally stable (positive) over the range of test conditions. The magnitude appears to remain constant with a slight increase in

stability noted for the larger descent angles. The value of  $N_V$  for the level flight case is in good agreement with the value calculated from the approximation based on the fact that the free-stream velocity on the vertical tail is the primary factor contributing to this derivative. From reference 24, assuming negligible sidewash, and a vertical tail efficiency factor of one, the directional stability can be written as:

$$N_V \approx \frac{q S_T A_T l_T}{I_Z U_{Of}}$$

and was computed using the following

$$A_T = 2 \text{ per radian}$$

$$I_Z = 270,000 \text{ slug-feet squared}$$

$$l_T = 23.5 \text{ feet}$$

$$S_T = 130 \text{ square feet}$$

$$U_{Of} = 57.8 \text{ feet per second}$$

resulting in

$$N_V = 0.0016 \text{ per foot-second}$$

#### Sideforce Due to Lateral Velocity ( $Y_V$ )

This stability derivative was found to be small and also remained fairly constant throughout the range of test conditions.

For the above descent cases, the data indicated that the dynamic motion of the full-scale aircraft in level flight was stable. The rolling mode would be convergent, with a time to one-half amplitude of 0.91 second, while the spiral mode would also be stable having a time to one-half amplitude of 49.3 seconds. The Dutch-roll

oscillation would be approximately neutral with a period of 8.4 seconds and a time to one-half amplitude of 138.0 seconds. The results for the second and third descent cases indicate the dynamic motion of the full-scale aircraft was similar. That is, both cases exhibited a spiral divergence, a rolling convergence, and a stable Dutch-roll oscillation. Specifically, for the  $5^\circ$  descent (case 2), the period of the Dutch-roll mode would be 7.9 seconds and a time to one-half amplitude of 53.0 seconds. The rolling convergence would have a time to one-half amplitude of 0.9 second, while the time to double amplitude of the divergent spiral mode would be 8.4 seconds. For the  $11^\circ$  descent (case 3) the data indicated the Dutch-roll period would be 8.4 seconds with a time to one-half amplitude of 8.1 seconds. The rolling convergence would have a time to one-half amplitude of 0.9 second, while the time to double amplitude for the spiral divergence would be 2.4 seconds.

#### AERODYNAMIC CHANGES

The test conditions of cases 4 and 5 were added to determine the effects of very limited aerodynamic changes for a particular descent case. Specifically, a reduction in the collective blade angle ( $\beta$ ), from  $13.5^\circ$  to  $11.5^\circ$ , was the only change made for case 4; further, at this new blade angle setting, the model test velocity ( $U_F$ ) for case 5 was increased from approximately 18.5 feet per second to 24 feet per second. The equivalent full-scale velocity for these two values are 58.5 fps (34.5 knots) and 76 fps (45 knots), respectively.

The stability derivatives calculated for the last two cases are compared to those of the descent cases on figure 1. Generally, the

results indicate that very little change, if any, was realized for the reduced blade angle setting case. Increasing the velocity shows that the effect on the stability derivatives was in the same direction as compared to case 4, though, for the most part, resulting in a much larger magnitude change. The only exceptions were those trends indicated for the dihedral effect and the sideforce derivative which were opposite to those realized in case 4.

The forward velocity effects, particularly regarding the side-velocity derivatives, are at best very difficult to explain. This is so because of the unknown interaction between the body, wing, and tail airloads, as affected by the free-stream and/or slipstream, particularly for a descending tilt-wing configuration. For example, a variation in lift, which may explain one stability derivative change would not necessarily explain a change in a different stability derivative. Generally, it can be said that the decrease in  $N_v$  is caused by a wake turbulence or interruption of the flow at the vertical tail - for the steep descent cases. An increase in the sideforce derivative can be attributed to fuselage impingement, while the larger negative value of  $L_v$  results from the change in lift experienced on each wing.

The dynamic motion of the full-scale aircraft computed for case 4 was almost identical to that of case 3. Apparently, as discussed above, a change in the blade collective pitch setting alone did not greatly alter the dynamics. The model results indicate that the full-scale aircraft would exhibit a stable Dutch-roll oscillation with a period of 8.1 seconds and a time to one-half amplitude of 9.1 seconds. The

rolling convergence would have a time to one-half amplitude of 1.0 second, while the spiral mode would be divergent, with a time to double amplitude of 2.6 seconds. The model results for case 5 indicate that the full-scale aircraft would exhibit quite a different dynamic motion. Specifically, an unstable Dutch-roll type oscillation was displayed, one that would have a period of 8.2 seconds and a time to double amplitude of 49.0 seconds. The rolling mode remained convergent, and would have a time to one-half amplitude of 0.9 second, while the spiral mode would be less divergent with a time to double amplitude of 9.6 seconds.

The results for the level flight case are, for the most part, in good agreement with the level flight results of reference 19. The only stability derivative that differs noticeably is the yaw moment due to roll rate ( $N_p$ ). The value found in the present study is of much larger magnitude and different in sign, that normally exhibited by conventional aircraft (i.e., negative). It is this term that apparently contributes to the slightly stable spiral mode, noted herein, another result that differed with the level flight case of reference 19.

These differences would be attributed to:

(a) The slight alterations in the testing procedure used during these investigations are noted in reference 22.

(b) The configuration of the model used in the present study to achieve level flight, particularly  $i_w = 40^\circ$ , as compared to the  $i_w = 30^\circ$  configuration used in reference 19.



The overall descent results appear to lend themselves to the discussion on descending flight in transition found in reference 2. Similar to the descent results noted in this reference, no wing buffet was encountered throughout the descent angle range of the present study and, by this fact, the feasibility of much higher descent angles is not known. It is believed, however, that any additional descent angle capability would be slight, because of the proximity of wing stall and the onset of poorer dynamics indicated by case 5.

It is also interesting to note that for direct data comparisons the computed stability derivatives presented herein compare favorably to those reported in reference 25. For the appropriate wing angle case ( $i_w = 40^\circ$ ) that is comparable to the level case of the present result, all the stability derivatives are in close agreement with the exception of  $N_v$  and  $L_r$ . These differences are evident in figure 1 and may be attributed to the variation in the testing techniques between the two studies. In addition, the trends in the roll and yaw damping stability derivatives as a function of descent angle, noted in reference 25, are in good agreement with the present results, again when the testing procedures are considered. Specifically, the descent conditions of reference 25 were achieved by changing the propeller rpm for a constant model angle of attack and wing incidence. This was not the procedure used to simulate descent for this study; therefore, it is fair to say that the descent cases per se are not directly comparable. The test conditions of the present investigation that are more in line with those of reference 25, are simply those for which the

angle of attack was held constant while some other parameter related to a change in thrust was varied. Clearly, this type of change is represented by cases 3 to 5. Comparison of the stability derivatives for these cases with those of reference 25, that is, yaw damping, roll damping, and directional stability, indicate that the results are in close agreement both in magnitude and trend. The only exception is that the yaw damping results do not agree. Again, this difference may be accounted for by the testing technique used, in that the damping term found during the forced oscillation tests of reference 25 was  $(N_r - N_{\dot{\beta}})$ , from which the yaw damping ( $N_r$ ) can not be separated. (Note,  $N_{\dot{\beta}}$  results from the yaw moment due to the rate of change of sideslip angle.)

## CONCLUSIONS

A 0.1-scale model of the XC-142A V/STOL transport was tested in the Princeton University Dynamic Model Track while in low-speed level and descending flight. The test cases included various descent angles at constant speed, and two conditions incorporating aerodynamic changes at the steepest descent. On the basis of the model results, the full-scale aircraft in level flight would be dynamically stable. A degradation in the aircraft's dynamics would be experienced as the descent angle is increased, to a point that for an  $11^\circ$  descent, the motion would be made up of a rolling convergence, and a lightly damped Dutch-roll oscillation and a spiral divergence with a time to double amplitude of 2.4 seconds.

The first aerodynamic variable change, consisting of a propeller blade angle change for an  $11^\circ$  descent, did not significantly alter the aircraft's dynamic motion, as compared to the original  $11^\circ$  descent case. However, for the second aerodynamic variable change, which consisted of increasing the airspeed in the reduced blade angle condition, the lateral-directional dynamics become more unstable, characterized by an unstable Dutch-roll oscillation with a time to double amplitude of 49.0 seconds.

Generally, the overall results appear consistent with the theory used for the analysis and computation of the stability derivatives. In addition, the results and trends are in good agreement with the limited data available from similar studies previously conducted.

## APPENDIX I

## ANALYSIS OF DATA

AXIS SYSTEM AND EQUATIONS OF MOTION

Model motions were measured with respect to a moving carriage; therefore, it is more convenient to use a space-fixed axis system to analyze these motions rather than the more conventional stability axis system. The  $X_F$ -axis is located along the direction of the motion of the carriage, with the  $Z_F$ -axis perpendicular to it, positive downward; the origin of the axis system is placed at the pivot point where the model is attached to the vertical link. The general body axis and space axis relationship is shown in figure 33. For the analysis presented herein,  $\eta$ , the angle between the model principal axis and fuselage reference, is assumed to be zero. Thus, the angle  $\zeta$ , shown in figure 33 is exactly equal to  $\theta$ . The order of rotation used to relate the body and space axes are as follows:

- (1)  $\psi$  rotation about  $Z_F$  (yaw gimbal) to align  $X_F$  with roll axis
- (2)  $\phi$  rotation about  $X'$  (roll gimbal) to align  $Y'$  with pitch gimbal
- (3)  $\theta$  rotation about  $Y''$  (pitch gimbal) to align  $X''$  with aircraft axis

The resultant aircraft angular rates expressed in terms of the space axis rates are:

$$\begin{aligned} p &= \dot{\phi} \cos \theta - \dot{\psi} \cos \phi \sin \theta \\ r &= \dot{\psi} \cos \phi \cos \theta + \dot{\phi} \sin \theta \\ q &= \dot{\theta} + \dot{\psi} \sin \phi \end{aligned} \tag{7}$$

When  $\phi$  is assumed small, the above relationships reduce the equations (2) of reference 22

$$\begin{aligned} p &= \dot{\phi} \cos \theta - \dot{\psi} \sin \theta \\ r &= \dot{\psi} \cos \theta + \dot{\phi} \sin \theta \\ q &= \dot{\theta} \end{aligned} \quad (8)$$

Differentiating, the angular acceleration expressions are:

$$\begin{aligned} \dot{p} &= \ddot{\phi} \cos \theta - \ddot{\psi} \sin \theta \\ \dot{r} &= \ddot{\psi} \cos \theta + \ddot{\phi} \sin \theta \\ \dot{q} &= \ddot{\theta} \end{aligned} \quad (9)$$

Using the vector equivalence for rates and moments, that is,

$$\begin{aligned} p &\approx L_B & \dot{\phi} &\approx I_G \\ r &\approx N_B & \dot{\psi} &\approx N_G \\ q &\approx M_B & \dot{\theta} &\approx M_G \end{aligned} \quad (10)$$

the rate expressions become:

$$\begin{aligned} L_B &= I_G \cos \theta - N_G \sin \theta \\ N_B &= N_G \cos \theta + I_G \sin \theta \\ M_B &= M_G \end{aligned} \quad (11)$$

Since the current study deals only with the lateral-directional stability derivatives, the analysis will be continued with the applicable rolling and yawing moment expressions. Using the first two moment expressions

of equations (11), to solve for the gimbal moments as a function of the body axis moments, the results are:

$$L_G = L_B \cos \theta + N_B \sin \theta \quad (12)$$

$$N_G = N_B \cos \theta - L_B \sin \theta$$

The general principal axis equations of motion (refs. 24 and 26) are:

$$I_x \dot{p} + qr(I_z - I_y) - (\dot{r} + pq)I_{xz} = L_B \quad (13)$$

$$I_z \dot{r} + pq(I_y - I_x) - (\dot{p} - qr)I_{xz} = N_B$$

Dropping the terms having products of rates and substituting these into equations (12)

$$L_G = I_x \dot{p} \cos \theta - I_{xz} \dot{r} \cos \theta + I_z \dot{r} \sin \theta - I_{xz} \dot{p} \sin \theta \quad (14)$$

$$N_G = I_z \dot{r} \cos \theta - I_{xz} \dot{p} \cos \theta - I_x \dot{p} \sin \theta + I_{xz} \dot{r} \sin \theta$$

Finally, substituting for the body-axis angular accelerations and combining coefficients of the space-axis angular accelerations:

$$\begin{aligned} L_G = & [I_x \cos^2 \theta - 2I_{xz} \sin \theta \cos \theta + I_z \sin^2 \theta] \ddot{\theta} \\ & + [(I_z - I_x) \sin \theta \cos \theta + (\sin^2 \theta - \cos^2 \theta) I_{xz}] \ddot{\psi} \\ N_G = & [I_x \sin^2 \theta + 2I_{xz} \sin \theta \cos \theta + I_z \cos^2 \theta] \ddot{\theta} \\ & + [(I_z - I_x) \sin \theta \cos \theta + (\sin^2 \theta - \cos^2 \theta) I_{xz}] \ddot{\psi} \end{aligned} \quad (15)$$

letting,

$$\begin{aligned}
 I_x \cos^2 \theta - 2I_{xz} \sin \theta \cos \theta + I_z \sin^2 \theta &\equiv I_x' \\
 I_x \sin^2 \theta + 2I_{xz} \sin \theta \cos \theta + I_z \cos^2 \theta &\equiv I_z' \\
 (I_z - I_x) \sin \theta \cos \theta + (\sin^2 \theta - \cos^2 \theta) I_{xz} &\equiv P_{xz}
 \end{aligned} \tag{16}$$

the general equations for the roll and yaw gimbal axes are then

$$\begin{aligned}
 I_x' \ddot{\phi} + P_{xz} \ddot{\psi} &= L_G \\
 I_z' \ddot{\psi} + P_{xz} \ddot{\phi} &= N_G
 \end{aligned} \tag{17}$$

The appropriate gimbal axis moments and cross product of inertia were computed for each descent case as a function of the pitch angle  $\theta$ , and are shown below. (Body inertias are given in table II).

	$\gamma$	$\theta = \alpha$	$\theta_a = \alpha + \gamma$	$I_x'$	$I_z'$	$P_{xz}$
Case 1	$0^\circ$	$0^\circ$	$0^\circ$	+3.0	+4.1	-0.2
Case 2	$-5^\circ$	$10^\circ$	$5^\circ$	+2.9	+4.1	0
Case 3 - 5	$-11^\circ$	$20^\circ$	$9^\circ$	+2.9	+4.1	+0.2

The body axis velocities are related to the carriage velocities through the same coordinate transformation outlined above. All of the velocity components realized at each step of the transformation, along with the expressions for the body axis velocities in terms of the space axis velocity, in complete and small angle linearized form, are presented

in figure 34. Again note, for the present study,  $\theta$  is used in place of  $\zeta$ . Using small angle perturbations, the most significant velocity expression is

$$v = v_f - U_{O_f} \psi \quad (18)$$

which will be used to convert the three-degree-of-freedom equations to the gimbal frame of reference.

The linearized, small perturbation lateral-directional equations of motion are:

$$\begin{aligned} Y_v v + g\phi - m(\dot{v} + U_{O_f} \dot{\psi}) &= 0 \\ L_v v + L_{\dot{\phi}} \dot{\phi} - \dot{\phi} + L_{\dot{\psi}} \dot{\psi} &= 0 \\ N_v v + N_{\dot{\phi}} \dot{\phi} + N_{\dot{\psi}} \dot{\psi} - \ddot{\psi} &= 0 \end{aligned} \quad (19)$$

For the present study, though, these equations were modified to the gimbal axis notation by: first, accounting for the inertia differences in the rolling and yawing moment equations; second, substituting the expression for the body sideward velocity term. These substitutions yield:

$$\begin{aligned} Y_{v_f} v_f - U_{O_f} Y_{v_f} \psi - m \dot{v}_f + g\phi &= 0 \\ L_{v_f} v_f - U_{O_f} L_{v_f} \psi + L_{\dot{\psi}} \dot{\psi} + L_{\dot{\phi}} \dot{\phi} - \dot{\phi} - \frac{P_{xz}}{I_x} \ddot{\psi} &= 0 \\ N_{v_f} v_f - U_{O_f} N_{v_f} \psi + N_{\dot{\psi}} \dot{\psi} + N_{\dot{\phi}} \dot{\phi} - \ddot{\psi} - \frac{P_{xz}}{I_z} \dot{\phi} &= 0 \end{aligned} \quad (20)$$



Note: The  $\psi$  coefficients can be expressed as  $Y_\psi$ ,  $L_\psi$ , and  $N_\psi$ , respectively, in the above equations.

One additional correction must be made to account for the "non-lifted" mass of the model support and gimbal system. Defining  $m_t$  as the total traveling mass, equal to the sum of model and linkage equipment, and  $m'$  as the total mass lifted (i.e.,  $-\frac{Z}{g}$ ), the term used in the lateral velocity equation may be modified by the ratio  $\frac{m_t}{m'}$ . This term effectively reduces the lateral acceleration produced by the given thrust, since this is less than the total weight of the moving system.

Since no dynamic tests were made with control inputs, these terms are not included. Other assumptions implicit in this form are: the vehicle is in level flight; the time rate of change of the product of inertia and moment of inertia terms is negligible. Although the effect of the product of inertia ( $I_{xz}$ ) could be neglected, it was retained because the method used to simulate the descent angle caused the product of inertia to be more significant at the steeper descents.

The space axis equations of motion in operator form, with the mass correction term are:

$$\begin{aligned} \left( Y_{v_f} - \frac{m_t}{m'} s \right) v_f + g\phi + Y_\psi \psi &= 0 \\ L_{v_f} v_f + (L_\phi s - s^2) \phi + \left( L_\psi + L_\psi s - \frac{P_{xz}}{I_x} s^2 \right) \psi &= 0 \\ N_{v_f} v_f + \left( N_\phi s - \frac{P_{xz}}{I_x} s^2 \right) \phi + (N_\psi + N_\psi s - s^2) \psi &= 0 \end{aligned} \quad (21)$$

The nontrivial solutions for  $v_f$ ,  $\phi$ ,  $\psi$  are realized through the characteristic equation

$$\begin{vmatrix} \left( Y_{v_f} - \frac{m_c}{m} S \right) & g & Y_{\psi} \\ L_{v_f} & (L_{\phi} S - S^2) & \left( L_{\psi} + L_{\dot{\psi}} S - \frac{P_{xz}}{I_x} S^2 \right) \\ N_{v_f} & \left( N_{\phi} S - \frac{P_{xz}}{I_z} S^2 \right) & (N_{\psi} + N_{\dot{\psi}} S - S^2) \end{vmatrix} = 0 \quad (22)$$

The natural modes of the aircraft motion are determined by the roots of the characteristic equation, that is, the values of "S" satisfying the above expression. Use of a space-fixed axis for the lateral-directional equations of motion results in a fifth-order system, or a fifth-degree characteristic equation. Since the constant term in the equation is equal to zero (ref. 19), one root is zero and remains so whenever yaw angle rather than yaw rate is used as a variable.

For the restricted degree-of-freedom tests, the reduced set of equations that apply are:

- (1) Single degree of freedom in  $\psi$ , ( $v_f = \phi = 0$ )

$$N_{\psi} + N_{\dot{\psi}} S - S^2 = 0 \quad (23)$$

(2) Two degrees-of-freedom

(a)  $\phi - \psi, (v_f = 0)$

$$\begin{vmatrix} \left( L\dot{\phi}S - S^2 \right) & \left( L\psi + L\dot{\psi}S - \frac{P_{xz}}{I_x} S^2 \right) \\ \left( N\dot{\phi}S - \frac{P_{xz}}{I_z} S^2 \right) & \left( N\psi + N\dot{\psi}S - S^2 \right) \end{vmatrix} = 0 \quad (24)$$

(b)  $\phi - v_f, (\psi = 0)$

$$\begin{vmatrix} \left( Y_{v_f} - \frac{m_t}{m'} S \right) & g \\ L_{v_f} & \left( L\dot{\phi}S - S^2 \right) \end{vmatrix} = 0 \quad (25)$$

# DATA ANALYSIS FOR CASE 1 (LEVEL FLIGHT)

## Single Degree-Of-Freedom

For each test case, the above equations were used to experimentally determine the lateral-directional stability derivatives of interest. Initially, for the level case, a yaw degree-of-freedom run was made with the model motors off (run 92, fig. 12). From the period of the motion  $\omega_d = 2.75$  1/sec was determined, and knowing the mechanical spring constant to be  $-31.7$  ft-lb/rad, the yaw moment of inertia was computed as  $4.1$  slug-ft<sup>2</sup>. Using the average values for the period and damping ratio, from table III, the single-degree-of-freedom root was determined as  $S = -0.33 \pm j2.86$ . Substituting into the single degree equation, the results are:

$$N_{\dot{\psi}} = -0.67 \text{ 1/sec}$$

$$N_{\psi} \text{ (mechanical plus aerodynamic)} = -8.41 \text{ 1/sec}^2$$

Eliminating the mechanical spring contribution, the  $N_{\psi}$  (aerodynamic) is  $N_{\psi} = -8.41 - (-7.58) = -0.83 \text{ 1/sec}^2$ .

## Two Degrees-Of-Freedom

With the single-degree-of-freedom data analyzed, the roll and yaw coupling was next examined using the concept of rotating time vectors and mode ratios as discussed in reference 27. For the particular set of equations used, it is more convenient to use the mode ratios rather than solving the system characteristic equation.

The idea that the oscillatory motion of a system described by a linear differential equation can be represented by a vector rotating about its tail forms the basis for use of time vectors. The length of the vector is proportional to amplitude of the oscillatory motion of the system and the damped natural frequency is represented by the angular velocity of the vector. If the oscillatory motion is damped, the vector length will decrease with time; if undamped, the vector length will increase with time. For multiple-degree-of-freedom systems, represented by a set of differential equations, the characteristic equation of the system contains an oscillatory pair of roots thus making it possible to represent the oscillatory mode in each variable by its own rotating time vector. The time vectors for the different variables in a particular mode will maintain a fixed-phase relationship with each other and rotate at the same frequency. The amplitude ratio and the phase angle between two variables are constant for a given linear system and do not depend upon the input or disturbance. The complex number relating the amplitudes of the two variables and the phase angle between them is called the mode ratio. Note, such an approach is also valid when only one mode is present in the response; therefore, for the analysis following, it is assumed that other modes of motion have damped out.

The relationships for the mode ratio of roll angle to yaw angle, for the two-degree-of-freedom motion in roll and yaw, as obtained from equations (24) are

$$\frac{\phi}{\psi} = \frac{L_{\psi} + L_{\dot{\psi}}S - \frac{P_{xz}}{I_x} S^2}{S^2 - L_{\dot{\phi}}S} \quad (26)$$

$$\frac{\phi}{\psi} = \frac{S^2 - N_{\dot{\psi}}S - N_{\psi}}{N_{\dot{\phi}}S - \frac{P_{xz}}{I_z} S^2} \quad (27)$$

where "S" is the root of the characteristic equation corresponding to the mode of interest. Since the mode ratio is a complex number, two stability derivatives can be evaluated from each of the above equations. The phase difference between the roll angle response and the yaw angle response was  $-115^\circ$  (i.e.,  $\phi$  lags  $\psi$  by  $115^\circ$ ), as determined from the data. The average amplitude ratio was 1.48, thus resulting the mode ratio  $\frac{\phi}{\psi} = -0.63 - j1.34$ . The period and the damping ratio of the oscillatory mode were 4.69 seconds and 0.129, respectively, ( $S = -0.17 + j1.36$ ). Using the values,  $L_{\dot{\phi}} = -0.4$  1/sec and  $\frac{P_{xz}}{I_x} = -0.067$ , the model space axis values for  $L_{\dot{\psi}}$  and  $L_{\psi}$  were calculated using equation (26), and found to be:

$$L_{\dot{\psi}} = +1.72 \text{ per second}$$

$$L_{\psi} = +2.20 \text{ per second squared}$$

Having the values of  $N_{\dot{\psi}}$  and  $N_{\psi}$  from the single-degree-of-freedom data, and  $\frac{P_{xz}}{I_z} = -0.049$ , either the real or imaginary part of equation (27) should have resulted in the same computed value for  $N_{\dot{\phi}}$ . However, there was a slight difference, probably resulting from an unbalanced pitching moment because of the model mounting used as

discussed in reference 19. Therefore, the stability derivative  $N_{\phi}$  was added to the mode ratio, with the modification yielding:

$$\frac{\phi}{\psi} = \frac{S^2 - N_{\psi}S - N_{\dot{\psi}}}{N_{\phi} + N_{\dot{\phi}}S - \frac{P_{xz}}{I_z} S^2} \quad (27a)$$

$N_{\dot{\phi}}$  and  $N_{\phi}$  were then determined using the values of  $N_{\dot{\psi}}$ ,  $N_{\psi}$ ,  $\frac{P_{xz}}{I_z}$ ,  $S$ , and  $\frac{\phi}{\psi}$  previously given. The results are:

$$N_{\dot{\phi}} = -0.58 \text{ per second}$$

$$N_{\phi} = +0.036 \text{ per second squared}$$

The value of  $N_{\phi}$  is an order of magnitude less than that found in reference 19, thus corresponding to a very low, almost insignificant, untrimmed pitching moment.

The mode ratio relating the roll angle to the side velocity was used in the same fashion as  $\frac{\phi}{\psi}$  described above, to compute the remaining derivatives of interest. From the  $\phi - v_f$  degree-of-freedom

$$\frac{\phi}{v_f} = \frac{\frac{m_t}{m'} S - Y_{v_f}}{g} \quad (28)$$

A value of  $\frac{m_t}{m'} = 2.16$  was determined from the static data ( $Z = 27.3$  lbs,  $m_t = 1.83$  slugs). The phase difference between the roll angle and the side velocity response is  $79^\circ$  (i.e.,  $v_f$  lags  $\phi$  by  $79^\circ$ ) as determined from the data.

The average amplitude ratio was 0.103, resulting in the mode ratio  $\frac{\phi}{v_f} = 0.02 + j0.1$ . The average period of the oscillatory mode was 6.1 seconds with a damping ratio  $\zeta = -0.14$ , the minus sign indicating an unstable oscillation ( $S = +0.21 + j1.08$ ). The side force due to side velocity was then computed from equation (28) with the result,  $Y_{v_f} = -0.2$  per second. Using the derivatives already determined and the fact that the side velocity and heading are related through the forward velocity, the additional stability derivatives of interest were computed as follows:

$$\begin{aligned} Y_{\psi} &= -U_{of} Y_{v_f} = +3.66 \text{ ft per sec}^2 \\ L_{v_f} &= -\frac{L_{\psi}}{U_{of}} = -0.12 \text{ per ft-sec} \\ N_{v_f} &= -\frac{N_{\psi}}{U_{of}} = +0.045 \text{ per ft-sec} \end{aligned} \quad (29)$$

The model space axis results for case 1, along with those for the additional test cases of this study, are shown in table V.

The accuracy of the linear theory used to compute the stability derivatives was examined by further application of the time vector method described in reference 27. This was accomplished by constructing the vector polygons for various degrees-of-freedom to establish whether or not the polygons closed as required. Specifically, the terms of the particular equations used were added vectorally in accordance with the applicable magnitude and phase relationship.

Figure 35 shows this magnitude and phase relationship between the roll and yaw angles and their higher order terms of interest. The



resulting magnitudes for each term, shown in this figure, were then multiplied by the appropriate stability derivative, as dictated by the equations of motion, and summed vectorally. The vector polygons for the yaw moment equation and roll moment equation for case 1 are shown in figures 36 and 37, respectively. As noted, the polygons close quite well indicating that the values computed and the technique used are credible. Similar diagrams were made for other degrees-of-freedom and for all of the cases of this investigation. Since all polygons closed with apparently the same accuracy, only the  $\phi - \psi$  relationship for case 1 has been presented as an illustration.

#### Three Degrees-Of-Freedom

No stability derivatives were computed using the available three-degree-of-freedom data. The purpose of presenting these data was to indicate the unrestrained motion of this configuration for the various test cases and to provide an additional means of verifying the computed results. The period and damping ratio for each case was determined from this data. For example, from figure 16 (case 1), the period of the oscillatory motion is about 4.4 seconds, and the damping ratio is seen to be very low, approximately  $\zeta = 0.04$ . The roots resulting from these terms are  $S \approx -0.06 \pm j1.4$ .

The space axis stability derivatives of the model, as computed from the data (table V), were used to solve the characteristic equation representing the gimbal axes as given in equation (22). Since the constant term was approximately zero, for most cases, the equation was simplified to a quartic. The results for each of the cases

are shown in root form, being

Case	Roots (model space axes)
1	-0.014, -1.488, +0.076+j1.562
2	+0.134, -1.367, -0.040+j1.073
3	+0.458, -1.339, -0.090+j1.648
4	+0.395, -1.300, -0.042+j1.663
5	-0.028, -1.340, +0.154+j1.697

As can be seen, the value of the oscillatory root determined for case 1, from the data, is in good agreement with the tabulated results. The three-degree-of-freedom data for the remaining cases were also examined and found to correlate with the solutions of the characteristic equations. The general characteristic equation (22) was also modified to represent the body axis equations of motion by simply deleting the attitude terms. The roots for the body axis dynamic motions of the model were then computed using the unadjusted body axis stability derivatives (those computed according to appendix II). These roots, given below, were used to compute the period, time to double or one-half amplitude, and the damping ratio associated with each mode and are presented for each case in tables VI to X.

Case	Roots (model body axes)
1	-0.024, -1.280, -0.023+j1.200
2	+0.221, -1.457, -0.027+j1.168
3	+0.668, -1.637, -0.045+j1.239
4	+0.587, -1.522, -0.032+j1.265
5	+0.105, -1.531, +0.183+j1.200

## APPENDIX II

### FULL-SCALE CONVERSION

The full-scale stability derivatives calculated for the various cases of this experiment were determined from the model values in the following manner: First, the expressions relating the space or gimbal axis moments to the model body axes were solved to transfer the model space derivatives to the model body axis values. Second, the model body axis derivatives were then converted to the full-scale values. The details relative to these steps will now be described.

#### CONVERSION TO MODEL BODY AXES

To determine the values of the model body axes derivatives, the rolling and yawing moments can be expressed as functions of the three aerodynamic parameters of interest during this study. That is, the moment dependency on roll rate, yaw rate, and sideward velocity are:

$$\begin{aligned} L_B &= \frac{\partial L}{\partial p} p + \frac{\partial L}{\partial r} r + \frac{\partial L}{\partial v} v \\ N_B &= \frac{\partial N}{\partial p} p + \frac{\partial N}{\partial r} r + \frac{\partial N}{\partial v} v \end{aligned} \quad (30)$$

The equations for  $p$ ,  $r$ , and  $v$ , as shown in appendix I, can be substituted into the above moment expressions, resulting in:

$$\begin{aligned} L_B &= \frac{\partial L}{\partial p} (\dot{\phi} \cos \theta - \dot{\psi} \sin \theta) + \frac{\partial L}{\partial r} (\dot{\psi} \cos \theta + \dot{\phi} \sin \theta) + \frac{\partial L}{\partial v} (v_f - U_{o_f} \psi) \\ N_B &= \frac{\partial N}{\partial p} (\dot{\phi} \cos \theta - \dot{\psi} \sin \theta) + \frac{\partial N}{\partial r} (\dot{\psi} \cos \theta + \dot{\phi} \sin \theta) + \frac{\partial N}{\partial v} (v_f - U_{o_f} \psi) \end{aligned} \quad (31)$$

These body moment expressions can then be used in the equations relating the gimbal and body moments (eqs. (12) and (17) from appendix I). For the roll and yaw equations the relationships then become

$$\begin{aligned}
 I_X \ddot{\phi} + P_{XZ} \ddot{\psi} = & [L_p \cos^2 \theta + L_r \sin \theta \cos \theta + N_p \cos \theta \sin \theta + N_r \sin^2 \theta] \dot{\phi} \\
 & + [-L_p \sin \theta \cos \theta + L_r \cos^2 \theta - N_p \sin^2 \theta + N_r \cos \theta \sin \theta] \dot{\psi} \\
 & + [L_v \cos \theta + N_v \sin \theta] v_f + [-U_{of} L_v \cos \theta - U_{of} N_v \sin \theta] \psi
 \end{aligned} \quad (32)$$

$$\begin{aligned}
 I_Z \ddot{\psi} + P_{XZ} \ddot{\phi} = & [N_p \cos^2 \theta + N_r \sin \theta \cos \theta - L_p \sin \theta \cos \theta - L_r \sin^2 \theta] \dot{\phi} \\
 & + [-N_p \sin \theta \cos \theta + N_r \cos^2 \theta + L_p \sin^2 \theta - L_r \sin \theta \cos \theta] \dot{\psi} \\
 & + [N_v \cos \theta - L_v \sin \theta] v_f + [-U_{of} N_v \cos \theta + U_{of} L_v \sin \theta] \psi
 \end{aligned}$$

Again note:  $L_\psi = -U_{of} L_v$

$N_\psi = -U_{of} N_v$

Since the general equations, as written from equations 21 of appendix I, are

$$\begin{aligned}
 I_X \ddot{\phi} + P_{XZ} \ddot{\psi} = & L_\phi \dot{\phi} + L_\psi \dot{\psi} + L_{v_f} v_f + L_\psi \psi \\
 I_Z \ddot{\psi} + P_{XZ} \ddot{\phi} = & N_\phi \dot{\phi} + N_\psi \dot{\psi} + N_{v_f} v_f + N_\psi \psi
 \end{aligned} \quad (33)$$

the appropriate expressions relating the gimbal and body derivatives are realized by simply setting the corresponding coefficients equal. That is:

$$\dot{L}_\phi = L_p \cos^2 \theta + (L_r + N_p) \sin \theta \cos \theta + N_r \sin^2 \theta \quad (34)$$

$$\dot{L}_\psi = (-L_p + N_r) \cos \theta \sin \theta + L_r \cos^2 \theta - N_p \sin^2 \theta \quad (35)$$

$$\dot{N}_\phi = N_p \cos^2 \theta + (N_r - L_p) \sin \theta \cos \theta - L_r \sin^2 \theta \quad (36)$$

$$\dot{N}_\psi = -(N_p + L_r) \sin \theta \cos \theta + N_r \cos^2 \theta + L_p \sin^2 \theta \quad (37)$$

$$L_{v_f} = L_v \cos \theta + N_v \sin \theta \quad (38)$$

$$N_{v_f} = N_v \cos \theta - L_v \sin \theta \quad (39)$$

$$L_\psi = -U_{O_f} L_v \cos \theta - U_{O_f} N_v \sin \theta \quad (40)$$

$$N_\psi = -U_{O_f} N_v \cos \theta + U_{O_f} L_v \sin \theta \quad (41)$$

The first four expressions have, as unknowns, the four body axis derivatives shown on the right-hand side of these equations. The gimbal axis values, the left-hand side of each equation, have been determined from the data presented. The last two groupings of equations (i.e.,  $L_{v_f}$  and  $N_{v_f}$ , or  $L_\psi$  and  $N_\psi$ ) are identical, thus, either set represents two equations with two unknowns. In addition to these moment expressions, the side force equation can be examined in the same manner; the correspondence was simply one to one, because

the side forces due to any of the angular rates were considered negligible.

Using the first four equations ((34) through (37)), the body axis stability derivatives are solved as functions of the remaining body axis values. The first and fourth equations result in an expression for  $L_p$ , while the second and third yield an expression for  $L_r$ . These expressions, when substituted back into the general equations from which they were determined, result in two equations having only  $N_r$  and  $N_p$  as the unknowns. Solving the two final equations simultaneously yields the body derivatives,  $N_r$  and  $N_p$ , which are subsequently used to determine  $L_p$  and  $L_r$ . For case 1, the body values are equal to the gimbal values because both axes are aligned when the pitch attitude is zero. The equations also lead to this result when  $\theta = 0$ , thus establishing a check on the equations developed for the analysis. As an example, the computations for case 2 will be shown. For this case,

$$\begin{aligned} \theta &= 10^\circ & L_{\dot{\theta}} &= -0.55 \text{ per sec} \\ \sin \theta &= 0.17 & L_{\dot{\psi}} &= +1.25 \text{ per sec} \\ \cos \theta &= 0.985 & N_{\dot{\theta}} &= -0.53 \text{ per sec} \\ \sin^2 \theta &= 0.03 & N_{\dot{\psi}} &= -0.53 \text{ per sec} \\ \cos^2 \theta &= 0.965 \end{aligned}$$

The expressions for  $L_p$  and  $L_r$  from equations (34) to (37) are

$$L_p = L\dot{\phi} + N\dot{\psi} - N_r = -1.08 - N_r \quad (42)$$

$$L_r = L\dot{\psi} - N\dot{\phi} + N_p = +1.78 + N_r$$

Substituting  $L_p$  and  $L_r$  into equations (34) and (35), the pair of equations resulting are

$$0.34 N_p - 0.777 N_r = 0.18$$

$$0.935 N_p + 0.34 N_r = -0.65$$

Solving simultaneously, yields

$$N_r = -0.4 \text{ per sec and } N_p = -0.62 \text{ per sec}$$

which in turn from (42) yields

$$L_p = -0.68 \text{ per sec and } L_r = 1.16 \text{ per sec}$$

Either of the last two sets of equations ((38) and (39), or (40) and (41)) could be used to find  $L_v$  and  $N_v$ . Again, for case 1, the equations indicate that the gimbal and body values are equal. Letting case 2 provide the example once more, the simultaneous set (from eqs. (38) and (39))

$$L_{v_r} = -0.1 = L_v \cos 10^\circ + N_v \sin 10^\circ$$

$$N_{v_r} = +0.084 = N_v \cos 10^\circ - L_v \sin 10^\circ$$

yields

$$L_v = -0.11 \text{ per ft-sec}$$

$$N_v = +0.065 \text{ per ft-sec}$$

This overall approach, that is solving the set of four equations in four unknowns, and the last simultaneous set, was used to calculate the model body axis stability derivatives for the remaining cases. All results are shown in tables VI to X.

#### FULL-SCALE DERIVATIVES

The second step of this procedure leading the actual aircraft's stability derivatives was the scaling up from the model body axis values, now known, to the full-scale value. Two calculations were performed on each derivative to acquire the final full-scale values. The first accounted for the difference between the scaled-down moments of inertia of the full-scale vehicle and the actual model; specifically, the rolling moment derivatives must be increased by a factor  $\frac{3.0}{1.5}$  while the factor  $\frac{4.1}{2.7}$  must be applied to the yawing moment derivatives. These adjusted model results were then converted to the full-scale values by use of the scale factors for dynamic model similarity, as listed in table XI. The body axis stability derivatives for the model, adjusted model, and full-scale vehicle for each case are presented in tables VI to X.

In order to present the dynamics of the full-scale aircraft, the body axis equations of motion were adjusted to account for the fact that the model was flying down the test track, simulating descent, in such a manner that the horizon was thought of as being rotated, rather than having the aircraft actually descending. Only the sideforce



equation is affected by this condition, and was rewritten to include the appropriate components of track velocity and gravity. The modified sideforce equation, as noted in reference 26, becomes:

$$\sum \bar{Y} = m[\dot{v} + U_r - W_p - g(\sin \theta_a)\psi - g(\cos \theta_a)\phi] \quad (43)$$

where:

$$U = U_f \cos \alpha$$

$$W = U_f \sin \alpha$$

$\theta_a$  = aerodynamic pitch angle  
between fictitious horizon  
and principal X-axis

Use of the aircraft's body axis eliminated all terms dependent on attitude (i.e.,  $N_\psi = Y_\psi = L_\psi = N_\phi = 0$ ), the cross products of inertia and permitted setting  $\frac{m_t}{m'} = 1$ . The modified characteristic equation then becomes:

$$\begin{vmatrix} Y_v - S & g \cos \theta_a + (U_f \sin \alpha)S & g \sin \alpha - (U_f \cos \alpha)S \\ L_v & L_p S - S^2 & L_r S \\ N_v & N_p S & N_r S - S^2 \end{vmatrix} = 0 \quad (44)$$

from which the roots for the full scale aircraft were computed.

Although the order of the equation is quintic, the constant terms for each case were approximately zero, and thus eliminated. The roots for the resulting quartic characteristic equation were:

Case	Roots (full-scale body axes)
1	-0.014, -0.760, -0.005+j0.753
2	-0.082, -0.756, -0.013+j0.721
3	+0.285, -0.779, -0.085+j0.748
4	+0.262, -0.715, -0.076+j0.783
5	+0.072, -0.744, +0.014+j0.770

These roots are graphically presented on figure 38 and were used to compute the period, damping ratio and time to double or one-half amplitude of the various modes, for each case, as noted on tables VI to X. It should be noted that the adjusted model axis roots were also determined using equation (44) and used to compute the periods damping ratios, etc., for the model: these results compared well with those values scaled down from the full-scale results.

## REFERENCES

1. White, R. M.: A Low Speed Wind Tunnel Test of a 0.11 Scale XC-142A Powered Model Conducted to Optimize the Production Slats. LTV Aerospace Corporation, Report No. 2-59730/3R/900, Dallas, Texas, Feb. 1964.
2. Newsom, W. A., Jr.; and Kirby, R. H.: Flight Investigation of Stability and Control Characteristics of a 1/9-Scale Model of a Four-Propeller Tilt-wing V/STOL Transport. NASA TN D-2443, Washington, D. C., Sept. 1964.
3. Newsom, W. A., Jr.; and Tosti, L. P.: Force-Test Investigation of the Stability and Control Characteristics of a 1/4-Scale Model of a Tilt-Wing Vertical-Take-Off-And-Landing-Aircraft. NASA Memo. 11-3-58L, Washington, D. C., Jan. 1959.
4. Foster, R. D.; and Kidd, D. L.: Summary Report of the Full Scale Wind Tunnel Tests of the XV-3 Convertiplane. Bell Aircraft Corp. Report 200-099-925, Fort Worth, Texas, Jan. 7, 1958.
5. Putman, W. F.; Traybar, J. J.; Curtiss, H. C., Jr.; and Kuk, J. P.: An Investigation of the Dynamic Stability Characteristics of a Quad Configuration, Ducted-Propeller V/STOL Model. Vol. 1, Phase 1 - Hovering Data Report, Princeton University, U. S. Army Aviation Materiel Laboratories, USAAVLABS TR 68-49A, Fort Eustis, Virginia, Sept. 1968.
6. Putman, W. F.; Traybar, J. J.; Curtiss, H. C., Jr.; and Kukon, J. P.: An Investigation of the Dynamic Stability Characteristics of a Quad Configuration, Ducted-Propeller V/STOL Model. Vol. 2, Phase 2 - Longitudinal Dynamics at High Duct Incidence. U. S. Army Aviation Materiel Laboratories, USAAVLABS TR 68-49B, Fort Eustis, Virginia, Aug. 1968.
7. Putman, W. F.; Traybar, J. J.; Curtiss, H. C., Jr.; and Kukon, J. P.: An Investigation of the Dynamic Stability Characteristics of a Quad Configuration, Ducted-Propeller V/STOL Model. Vol. 3, Phase 3 - Lateral/Directional Dynamics at High Duct Incidences. Data Report Princeton University, U. S. Army Aviation Materiel Laboratories, USAAVLABS TR-68-49C, Fort Eustis, Virginia, Nov. 1968.
8. Koenig, D. G.; Grief, R. K.; and Kelly, M. W.: Full-Scale Wind-Tunnel Investigation of the Longitudinal Characteristics of a Tilting-rotor Convertiplane. NASA TN D-35, Washington, D. C., Dec. 1959.

9. Spreeman, Kenneth P.: Wind-Tunnel Investigation of Lateral Aerodynamic Characteristics of a Powered Four-Duct-Propeller V/STOL Model in Transition. NASA D-4343, Washington, D. C., Feb. 1968.
10. Deal, P. L.; and Jenkins, J. L., Jr.: Flight Investigation of the Wing-Rotor Lift-Sharing Characteristics of a Hingeless Rotor Compound Helicopter. Presented at the 24th Annual National Forum of the American Helicopter Society. Washington, D. C., May 1968.
11. Van Wyckhouse, J. F.: High Performance UH-1 Compound Helicopter Maneuver Flight Test Program. U. S. Army Aviation Materiel Laboratories, USAAVLABS TR-66-17, Fort Eustis, Virginia, Feb. 1966.
12. Lentine, F. P.; Groth, W. P.; and Oglesby, T. H.: Research in Maneuverability of the XH-51A Compound Helicopter. U. S. Army Aviation Laboratory, USAAVLABS TR-68-23, Fort Eustis, Virginia, June 1968.
13. Pegg, Robert J.: Summary of Flight-Test Results of the VZ-2 Tilt-Wing Aircraft. NASA TN D-989, Washington, D. C., Feb. 1962.
14. Down, H. W., Jr.; Jones, G. E.; and Satterwhite, J. J.: XC-142A Limited Category II Stability and Control Tests. Air Force Flight Test Center TR No. 68-9, Edwards Air Force Base, Calif., Sept. 1968.
15. Ransone, R. K.; and Jones, G. E.: XC-142A V/STOL Transport Tri-Service Limited Category I Evaluation. Air Force Flight Test Center, TR No. 65-27, Edwards Air Force Base, Calif., Jan. 1966.
16. Reeder, J. P.: Handling Qualities Experience With Several VTOL Research Aircraft. NASA TN D-735, Washington, D. C., March 1961.
17. McKinzie, G. A.; Bradfield, E. N., Jr.; Ludwig, J. H.; and Casey, W. R.: P-1127 (XV-6A) VSTOL Handling Qualities Evaluation. Air Force Flight Test Center TR No. 68-10, Edwards Air Force Base, Calif., Aug. 1968.
18. Leppert, D. S.: Model XC-142A Aircraft Flight Test, Biweekly Summary Report No. 11. LTV Vought Aeronautics Division, Dallas, Texas, March 29, 1965.
19. Boyden, R. P.; and Curtiss, H. C., Jr.: Investigation of the Lateral/Directional Stability Characteristics of a Four-Propeller Tilt-wing VTOL Model. U. S. Army Aviation Materiel Laboratories, USAAVLABS TR 68-19, Fort Eustis, Virginia, April 1968.

20. Curtiss, H. C., Jr.; Putnam, W. F.; and Lebacqz, J. V.: An Experimental Investigation of the Longitudinal Dynamic Stability Characteristics of a Four-Propeller Tilt-Wing VTOL Model. U. S. Army Aviation Materiel Laboratories, USAAVLABS TR 66-80, Fort Eustis, Virginia, 1966.
21. Curtiss, H. C., Jr.; Putnam, W. F.; and Martinez, E.: The Evaluation of Stability and Control Characteristics of Aircraft at Low Speeds Using Dynamically Similar Models in Semi-Free Flight. Proceedings of the American Helicopter Society Eighteenth Annual National Forum, Washington, D. C., May 1962.
22. Putman, William F.: An Investigation of the Lateral/Directional Dynamic Stability Characteristics of a Tilt-Wing V/STOL Transport Model in Low Speed Descending Flight. U. S. Army Aviation Materiel Laboratories, USAAVLABS TR 69-46, Fort Eustis, Virginia, July 1969.
23. Curtiss, H. C., Jr.; Traybar, J. J.; and Putman, W. F.: General Description of the Princeton Dynamic Model Track. U. S. Army Aviation Materiel Laboratories, USAAVLABS TR 66-73, Fort Eustis, Virginia, Nov. 1966.
24. Seckel, Edward: Stability and Control of Airplanes and Helicopters. Academic Press, New York, 1964. (ff )
25. Chambers, Joseph R.; and Grafton, Sue B.: Investigation of Lateral-Directional Dynamic Stability of a Tilt-Wing V/STOL Transport. NASA TN D-5637, Washington, D. C., Feb. 1970.
26. Dynamics of the Airframe. Bureau of Aeronautics Report AE-61-4-II, Norair Division of Northrop Corporation, Hawthorne, Calif., Sept. 1952.
27. Breuhaus, W. O.: Resume of the Time Vector Method as a Means for Analyzing Aircraft Stability Problems. Wright Air Development Center, WADC TR 52-299, Wright-Patterson Air Force Base, Ohio, Nov. 1952.

TABLE I.- SUMMARY OF TEST CONDITIONS

All tests conducted at $i_w = 40^\circ$ , $\delta_f = 60^\circ$ and model rpm = 4000 except where rpm = 0 as noted.							
Fuselage pitch attitude $\theta = \alpha$ (deg)	Collective pitch $\beta.75R$ (deg)	Descent angle $\gamma$ (deg)	Aerodynamic pitch attitude $\theta_a = \alpha + \gamma$ (deg)	Trim velocity $U_f$ (ft/sec)	Run Nos.	Figure Nos.	Degrees of freedom
0 (case 1)	13.5	0	0	17.8	91	12	$\psi^*$
				0	92**		
				19.4	102 106	13	
				17.6	164 166	14	$\phi-\psi$
				18.4	179 182	15	$\phi-v_f$
				17.9	203 204	16	$\phi-\psi-v_f$
10 (case 2)	13.5	-5	5	17.8	213 214	17	$\psi$
				17.7	210 212	18	$\phi-\psi$
				17.6	220 224	19	$\phi-v_f$
				18.4	228 229	20	$\phi-\psi-v_f$

\* Mechanical spring in place,  $K_{\psi_m} = -31.7 \text{ ft-lb/rad}$ 

\*\* rpm = 0

TABLE I.- Concluded

All tests conducted at $i_w = 40^\circ$ , $\delta_f = 60^\circ$ and model rpm = 4000 except where rpm = 0 as noted.							
Fuselage pitch attitude $\theta = \alpha$ (deg)	Collective pitch $\beta_{.75R}$ (deg)	Descent angle $\gamma$ (deg)	Aerodynamic pitch attitude $\theta_a = \alpha + \gamma$ (deg)	Trim velocity $U_f$ (ft/sec)	Run Nos.	Figure Nos.	Degrees of freedom
20 (case 3)	13.5	-11	9	18.6	234	21	$\psi$
					235		
					231	22	$\phi-\psi$
					232		
				18.4	238	23	$\phi-v_f$
					239		
					247	24	$\phi-\psi-v_f$
					248		
20 (case 4)	11.5	-11	9	18.1	261	25	$\psi$
					263		
				18.8	251	26	$\phi-\psi$
					254		
				18.4	269	27	$\phi-v_f$
					270		
20 (case 5)	11.5	-11	9	23.5	323	28	$\psi$
					326		
				24.0	331	29	$\phi-\psi$
					336		
				23.6	327	30	$\phi-v_f$
					329		
					339	31	$\phi-\psi-v_f$
					341		

TABLE II.- MODEL GEOMETRIC AND INERTIAL CHARACTERISTICS

Model weight,  $W_p = 45.9$  pounds

Rolling moment of inertia,  $I_x = 3.0$  slug-feet squared

Yawing moment of inertia,  $I_z = 4.1$  slug-feet squared

Wing area = 5.34 feet squared

cg position:

$x_{cg} = 9$  percent mean aerodynamic chord  
 $i_w = 0$

$z_{cg} = 26.5$  percent mean aerodynamic chord  
below wing reference plane location  
at  $i_w = 0$



REPRODUCIBILITY OF THE  
ORIGINAL PAGE IS POOR

52

TABLE III.- SUMMARY OF TRANSIENT RESPONSE DATA (MEASURED)  
FOR SINGLE DEGREE OF FREEDOM  
( $\psi$  only)

	Run	$\psi$ -period (sec)	$\zeta$		Run	$\psi$ -period (sec)	$\zeta$
Case 1 (with mech. springs)	86	2.17	0.110	Case 3	234	5.80	0.175
	87	2.17	.115		235	4.50	.162
	88	2.15	.116		236	4.80	.158
	89	2.20	.116		Averages	5.03	0.165
	96	2.20	.112	Case 4			
	97	2.20	.118				
	98	2.18	.122		260	5.20	0.20
	99	2.30	.131		261	5.50	.19
	102	2.20	.100		262	5.80	.21
	103	2.15	.118		263	5.50	.20
	104	2.20	.105		Averages	5.50	0.20
	105	2.20	.108	Case 5			
	106	2.20	.124		323	4.50	0.18
	Averages	2.2	0.115		324	5.10	.17
Case 2	213	5.30	0.220		325	5.10	.19
	213R	5.40	.220		326	5.00	.18
	Averages	5.35	0.220		Averages	4.93	0.18

TABLE IV. - SUMMARY OF TRANSIENT RESPONSE DATA (MEASURED)

FOR MULTIPLE DEGREES OF FREEDOM  
(Note: both variables presented)

Two degrees of freedom ( $\phi - \psi$ )					
	Run	$\phi$ -period (sec)	$\zeta$	$\psi$ -period (sec)	$\zeta$
Case 1	152	4.8	0.076	4.8	0.073
	163	5.0	.125	4.5	.170
	164	4.5	.220	4.3	.230
	166	4.8	.078	4.5	.084
	167	5.0	.090	4.7	.095
	Averages	4.7	0.129		
Case 2	209	4.5	0.140	6.0	0.135
	210	4.7	.150	5.0	.148
	212	4.6	.130	4.8	.125
	Averages	4.9	0.138		
Case 3	230	4.5	0.130	4.6	0.130
	231	4.8	.120	4.8	.155
	232	5.0	.130	4.6	.145
	Averages	4.7	0.135		
Case 4	251	4.0	0.130	4.4	0.140
	253	4.6	.100	4.4	.095
	254	4.8	.095	4.6	.095
	Averages	4.5	0.110		
Case 5	331	4.3	-0.09	4.3	-0.10
	332	4.5	-0.09	4.5	-0.09
	336	4.3	-0.11	4.5	-0.18
	Averages	4.4	-0.11		

TABLE IV.- Concluded

Two degree of freedom ( $\phi - v_f$ )					
	Run	$\phi$ -period (sec)	$\zeta$	$v_f$ -period (sec)	$\zeta$
Case 1	179	5.6	-0.190	5.6	-0.185
	181	6.1	-0.185	6.7	-0.185
	182	5.7	-0.195	5.8	-0.197
	Averages	5.9	-0.190		
Case 2	219	5.9	-0.120	6.0	-0.110
	220	5.8	-0.115	5.8	-0.127
	224	6.6	-0.138	6.7	-0.141
	225	5.9	-0.155	6.0	-0.157
	Averages	6.1	-0.140		
Case 3	237	5.9	-0.120	6.0	-0.125
	238	6.5	-0.140	6.5	-0.140
	239	6.5	-0.115	6.5	-0.150
	Averages	6.4	-0.130		
Case 4	267	5.8	-0.175	5.4	-0.135
	269	6.5	-0.190	6.6	-0.170
	270	6.2	-0.180	6.0	-0.135
	Averages	6.1	-0.170		
Case 5	294	5.6	-0.190	5.0	-0.180
	295	5.4	-0.200	5.2	-0.190
	316	5.6	-0.200	5.4	-0.170
	317	5.6	-0.220	5.6	-0.210
	327	5.4	-0.205	5.2	-0.190
	328	5.6	-0.195	5.2	-0.195
	329	5.6	-0.195	5.3	-0.195
	Averages	5.4	-0.210		

TABLE V. - MODEL SPACE AXIS STABILITY DERIVATIVES

Parameter	Case 1	Case 2	Case 3	Case 4	Case 5
$N_{\dot{\psi}}, 1/\text{sec}$	-0.67	-0.53	-0.41	-0.46	-0.41
$N_{\dot{\psi}}^*, 1/\text{sec}^2$ (= $-U_{OF}N_V$ )	-0.83	-1.51	-1.66	-1.49	-1.57
$N_{\dot{\phi}}, 1/\text{sec}$	-0.58	-0.53	-0.13	-0.29	-0.33
$N_{\dot{\phi}}, 1/\text{sec}^2$	+0.036	-0.15	-0.077	-0.023	-0.36
$N_V, 1/\text{ft-sec}$	+0.045	+0.084	+0.09	+0.08	+0.066
$L_{\dot{\psi}}, 1/\text{sec}$	+1.72	+1.25	+1.80	+1.76	+1.28
$L_{\dot{\psi}}^*, 1/\text{sec}^2$ (= $-U_{OF}L_V$ )	+2.20	+0.82	+1.67	+1.48	+3.49
$L_{\dot{\phi}}^{**}, 1/\text{sec}$	-0.63	-0.55	-0.40	-0.40	-0.40
$L_V, 1/\text{ft-sec}$	-0.12	-0.10	-0.06	-0.06	-0.11
$Y_{\dot{\psi}}^*, \text{ft/sec}^2$ (= $-U_{OF}Y_V$ )	+3.66	+4.71	+7.75	+3.13	+10.9
$Y_V, 1/\text{sec}$	-0.20	-0.25	-0.42	-0.17	-0.46
$U_{OF}, \text{ft/sec}$	18.3	18.3	18.5	18.4	23.7
$X_F, \text{lb}$	+0.7	-2.3	-5.5	-5.95	-6.1
$Z_F, \text{lb}$	27.3	25.9	27.6	29.2	29.0
$m_t/m'$	2.16	2.27	2.22	2.05	2.02

\* Derivatives exist due to use of space axis system.

\*\*Value approximated for each case.

TABLE VI.- BODY AXIS STABILITY DERIVATIVES AND PARAMETERS (CASE 1)

Parameter	Model	Adjusted model	Full-scale aircraft
$N_r$ , 1/sec	-0.67	-1.02	-0.32
$N_p$ , 1/sec	-0.58	-0.88	-0.28
$N_v$ , 1/ft-sec	+0.045	+0.068	+0.002
$L_r$ , 1/sec	+1.72	+3.44	+1.09
$L_p$ , 1/sec	-0.63	-1.26	-0.40
$L_v$ , 1/ft-sec	-0.12	-0.24	-0.008
$Y_v$ , 1/sec	-0.20	-0.20	-0.063
$I_x$ , slug-ft <sup>2</sup>	3.0	1.5	150,000
$I_z$ , slug-ft <sup>2</sup>	4.1	2.7	270,000
<u>Oscillatory mode (Dutch roll)</u>			
Period, sec	5.2	2.6	8.4
Time to one-half amplitude ( $T_{1/2}$ ), sec	30.0	27.6	138.0
Damping ratio ( $\xi$ )	0.02	0.01	0.01
<u>First real mode (spiral)</u>			
Time to one-half amplitude ( $T_{1/2}$ ), sec	26.9	14.6	49.3
<u>Second real mode (rolling mode)</u>			
Time to one-half amplitude ( $T_{1/2}$ ), sec	0.54	0.29	0

TABLE VII.- BODY AXIS STABILITY DERIVATIVES AND PARAMETERS (CASE 2)

Parameter	Model	Adjusted model	Full-scale aircraft
$N_r$ , 1/sec	-0.40	-0.61	-0.19
$N_p$ , 1/sec	-0.62	-0.94	-0.30
$N_y$ , 1/ft-sec	+0.065	+0.099	+0.003
$L_r$ , 1/sec	+1.16	+2.32	+0.73
$L_p$ , 1/sec	-0.68	-1.36	-0.43
$L_y$ , 1/ft-sec	-0.11	-0.22	-0.007
$Y_v$ , -/sec	-0.25	-0.25	-0.08
$I_x$ , slug-ft <sup>2</sup>	3.0	1.5	150,000
$I_z$ , slug-ft <sup>2</sup>	4.1	2.7	270,000
<u>Oscillatory mode (Dutch roll)</u>			
Period, sec	5.4	2.5	7.9
Time to one-half amplitude ( $T_{1/2}$ ), sec	25.6	14.7	53.0
Damping ratio ( $\zeta$ )	0.02	0.02	0.02
<u>First real mode (spiral)</u>			
Time to double amplitude ( $T_2$ ), sec	3.1	2.5	8.4
<u>Second real mode (rolling mode)</u>			
Time to one-half amplitude ( $T_{1/2}$ ), sec	0.48	0.29	0.92

TABLE VIII.- BODY AXIS STABILITY DERIVATIVES AND PARAMETERS (CASE 3)

Parameter	Model	Adjusted model	Full-scale aircraft
$N_r$ , 1/sec	+0.14	+0.21	+0.066
$N_p$ , 1/sec	-0.30	-0.46	-0.15
$N_v$ , 1/ft-sec	-0.06	+0.10	+0.003
$L_r$ , 1/sec	+1.63	+3.26	+1.03
$L_p$ , 1/sec	-0.95	-1.90	-0.60
$L_v$ , 1/ft-sec	-0.087	-0.174	-0.006
$Y_v$ , 1/sec	-0.42	-0.42	-0.13
$I_x$ , slug-ft <sup>2</sup>	3.0	1.5	150,000
$I_z$ , slug-ft <sup>2</sup>	4.1	2.7	270,000
<u>Oscillatory mode (Dutch roll)</u>			
Period, sec	5.1	2.6	8.4
Time to one-half amplitude ( $T_{1/2}$ ), sec	15.4	2.4	8.1
Damping ratio ( $\xi$ )	0.04	0.12	0.12
<u>First real mode (spiral)</u>			
Time to double amplitude ( $T_2$ ), sec	1.03	0.76	2.42
<u>Second real mode (rolling mode)</u>			
Time to one-half amplitude ( $T_{1/2}$ ), sec	0.42	0.28	0.89

TABLE IX.- BODY AXIS STABILITY DERIVATIVES AND PARAMETERS (CASE 4)

Parameter	Model	Adjusted model	Full-scale aircraft
$N_r$ , 1/sec	+0.02	+0.03	+0.01
$N_p$ , 1/sec	-0.44	-0.67	-0.21
$N_v$ , 1/ft-sec	+0.055	+0.083	+0.003
$L_r$ , 1/sec	+1.61	+3.22	+1.02
$L_p$ , 1/sec	-0.88	-1.76	-0.56
$L_v$ , 1/ft-sec	-0.084	-0.168	-0.005
$Y_v$ , 1/sec	-0.17	-0.17	-0.054
$I_x$ , slug-ft <sup>2</sup>	3.0	1.5	150,000
$I_y$ , slug-ft <sup>2</sup>	4.1	2.7	270,000
<u>Oscillatory mode (Dutch roll)</u>			
Period, sec	4.9	2.6	8.1
Time to one-half amplitude ( $T_{1/2}$ ), sec	21.6	3.3	9.1
Damping ratio ( $\xi$ )	0.03	0.10	0.10
<u>First real mode (spiral)</u>			
Time to double amplitude ( $T_2$ ), sec	1.2	0.92	2.63
<u>Second real mode (rolling mode)</u>			
Time to one-half amplitude ( $T_{1/2}$ ), sec	0.45	0.31	0.96



TABLE X.- BODY AXIS STABILITY DERIVATIVES AND PARAMETERS (CASE 5)

Parameter	Model	Adjusted model	Full-scale aircraft
$N_r$ , 1/sec	-0.11	-0.167	-0.053
$N_p$ , 1/sec	-0.45	-0.68	-0.21
$N_v$ , 1/ft-sec	+0.024	+0.036	+0.001
$L_r$ , 1/sec	+1.16	+2.32	+0.73
$L_p$ , 1/sec	-0.69	-1.38	-0.44
$L_v$ , 1/ft-sec	-0.125	-0.25	-0.008
$Y_v$ , 1/sec	-0.46	-0.46	-0.15
$I_x$ , slug-ft <sup>2</sup>	3.0	1.5	150,000
$I_y$ , slug-ft <sup>2</sup>	4.1	2.7	270,000
<u>Oscillatory mode (Dutch roll)</u>			
Period, sec	5.2	2.5	8.2
Time to double amplitude ( $T_2$ ), sec	3.8	10.2	49.0
Damping ratio ( $\zeta$ )	-0.15	-0.02	-0.02
<u>First real mode (spiral)</u>			
Time to double amplitude ( $T_2$ ), sec	6.6	3.6	9.6
<u>Second real mode (rolling mode)</u>			
Time to one-half amplitude ( $T_{1/2}$ ), sec	0.45	0.30	0.89

TABLE XI.- SCALE FACTORS FOR DYNAMIC MODEL SIMILARITY

Multiply full-scale property by scale factor to obtain model property.

		For $\lambda = 10$
Linear dimension	$\lambda^{-1}$	0.1
Area	$\lambda^{-2}$	0.01
Volume, mass, force	$\lambda^{-3}$	0.001
Moment	$\lambda^{-4}$	0.0001
Moment of inertia	$\lambda^{-5}$	0.00001
Linear velocity	$\lambda^{-0.5}$	0.316
Linear acceleration	$\lambda^0$	1.
Angular velocity	$\lambda^{0.5}$	3.16
Angular acceleration	$\lambda$	10.
Time	$\lambda^{-0.5}$	0.316
Frequency	$\lambda^{0.5}$	3.16
Reynolds number	$\lambda^{-1.5}$	0.0316
Mach number	$\lambda^{-0.5}$	0.316

where  $\lambda = \frac{\text{model linear dimension}}{\text{full-scale linear dimension}}$

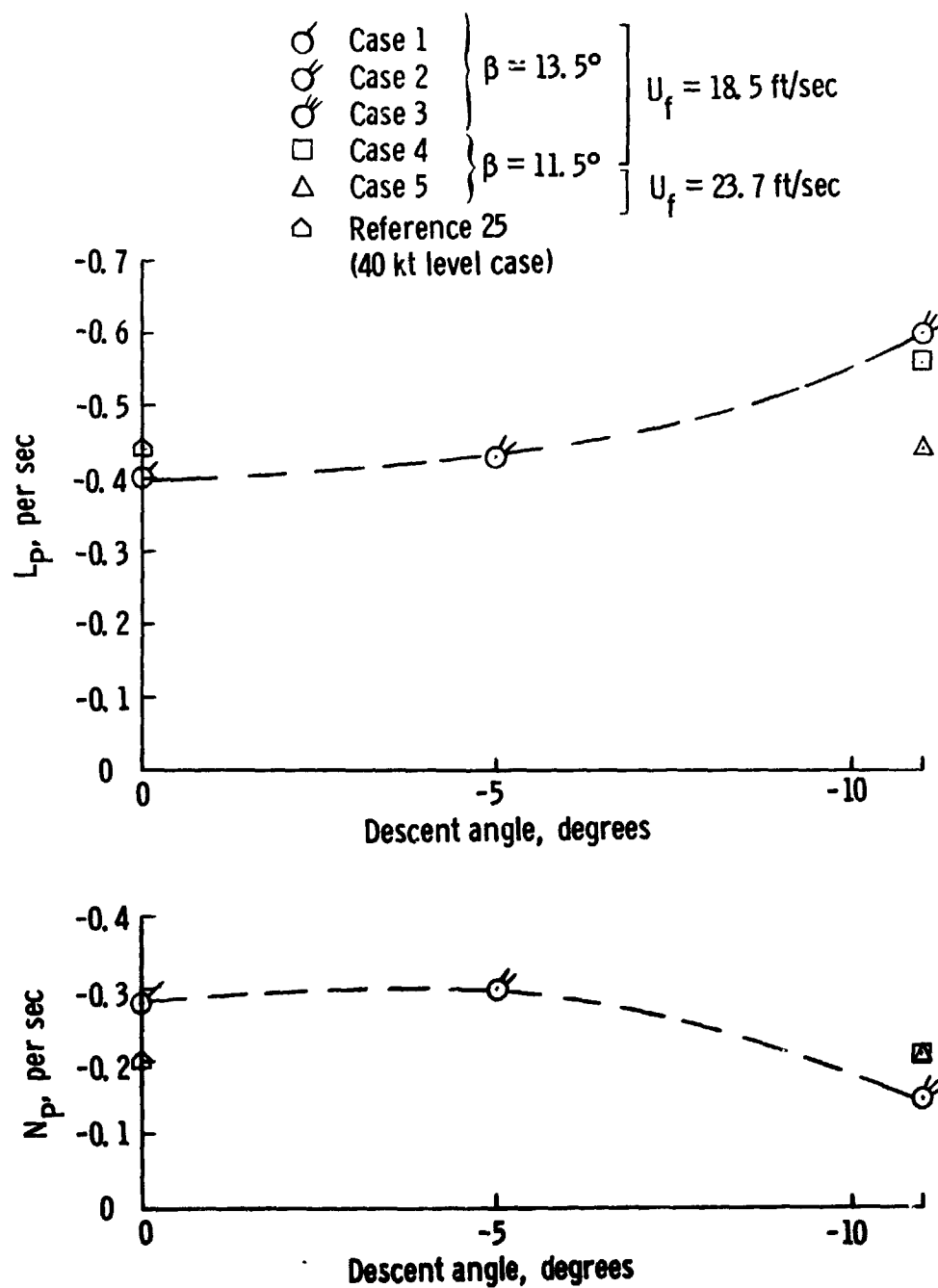


Figure 1.- Full scale stability derivatives.

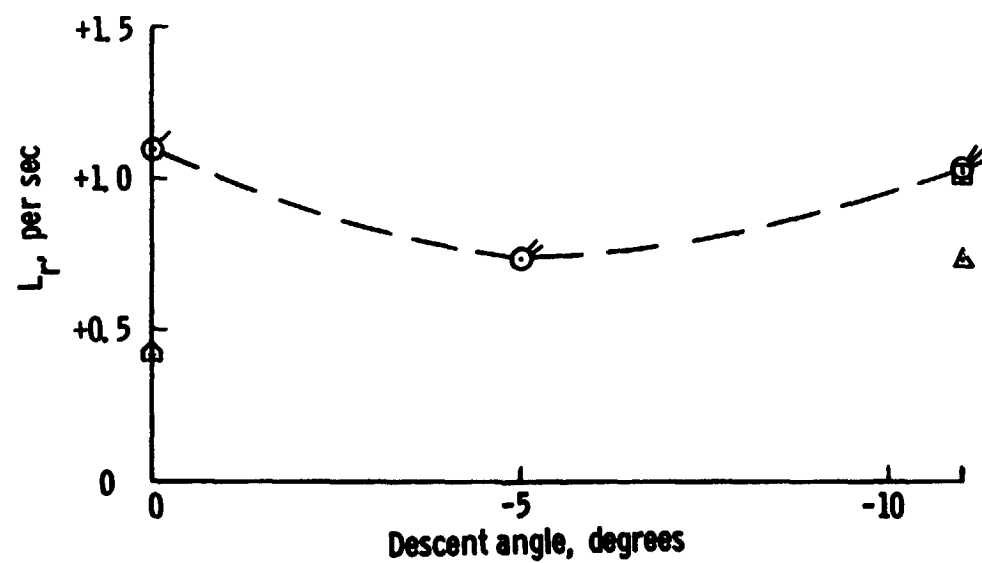
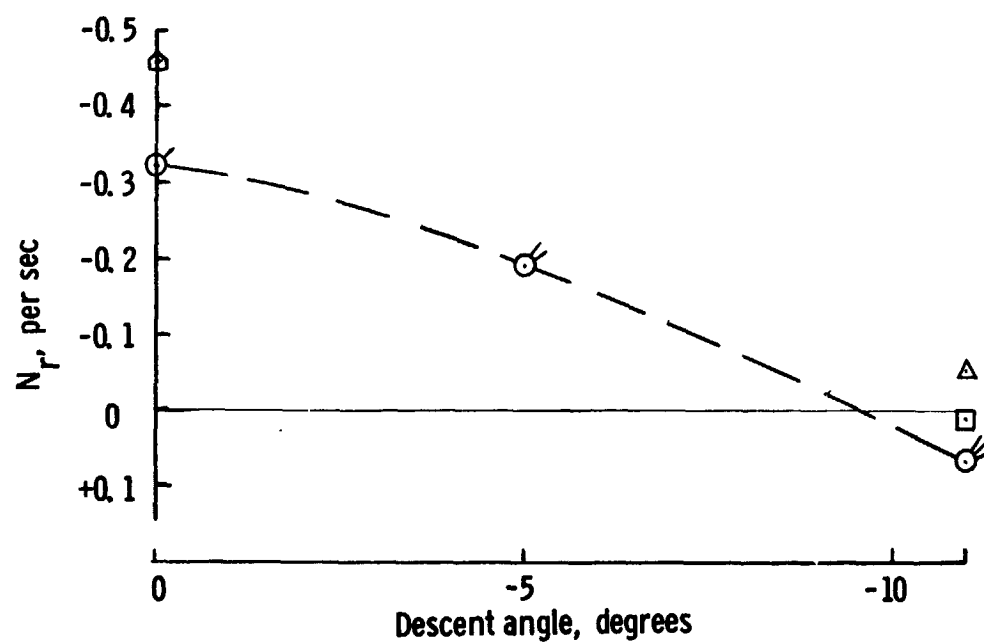


Figure 1.- Continued.

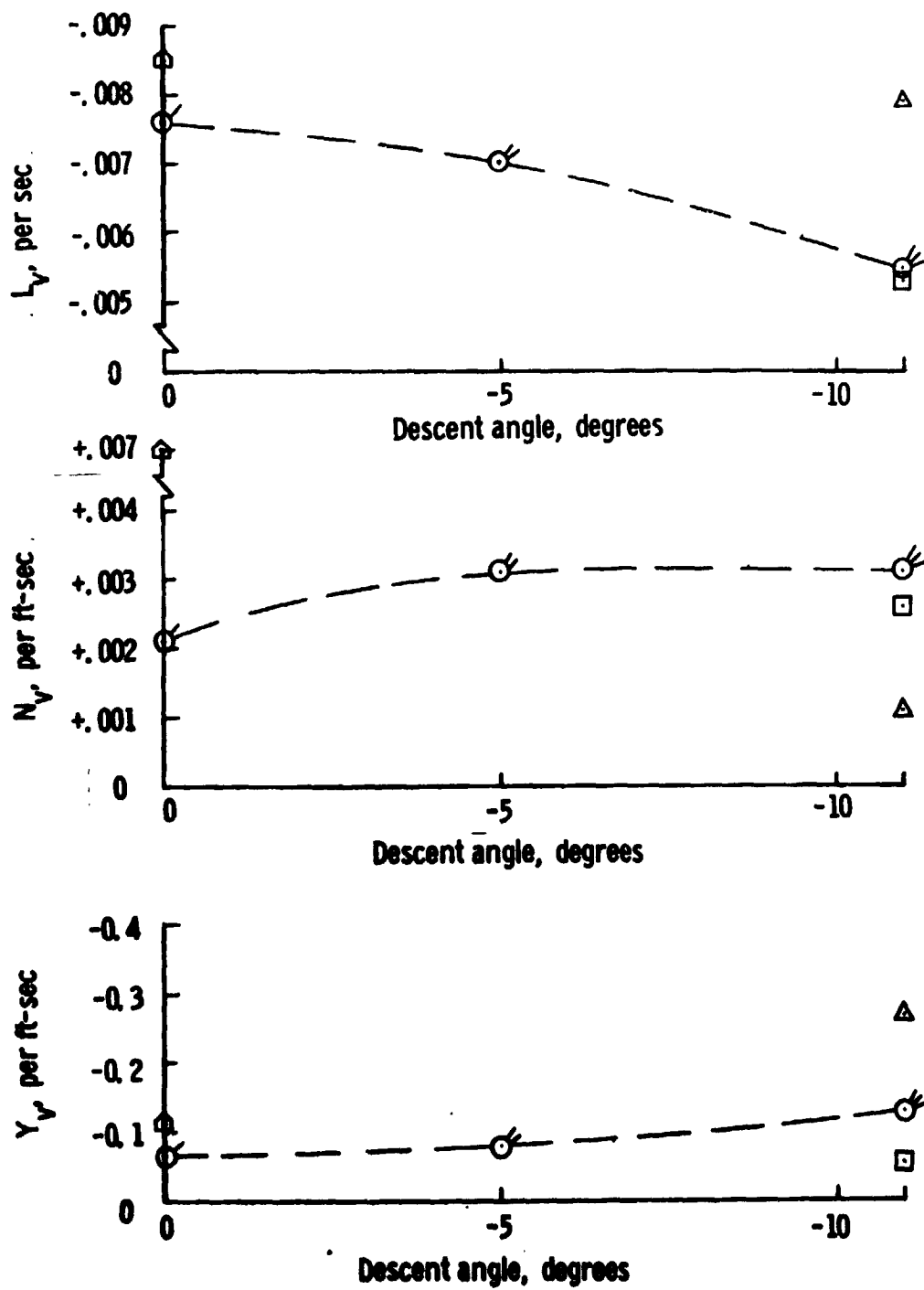


Figure 1.- Concluded.

REPRODUCIBILITY OF THE ORIGINAL PAGE IS POOR.

Figure 2.- Princeton Dynamic Model Track longitudinal mount  
with one-tenth scale dynamically similar model.

REPRODUCIBILITY OF THE ORIGINAL PAGE IS POOR.

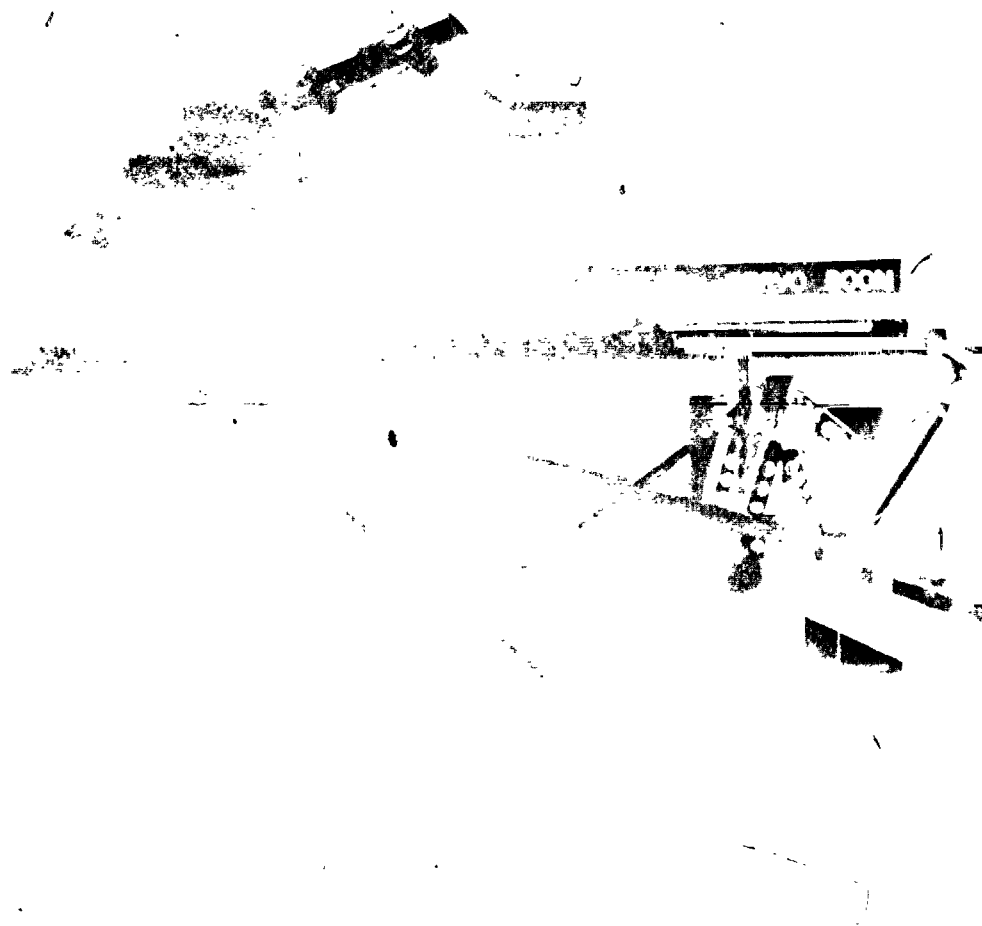


Figure 3.- Princeton Dynamic Model Track lateral/directional mount with one-tenth scale dynamically similar model.

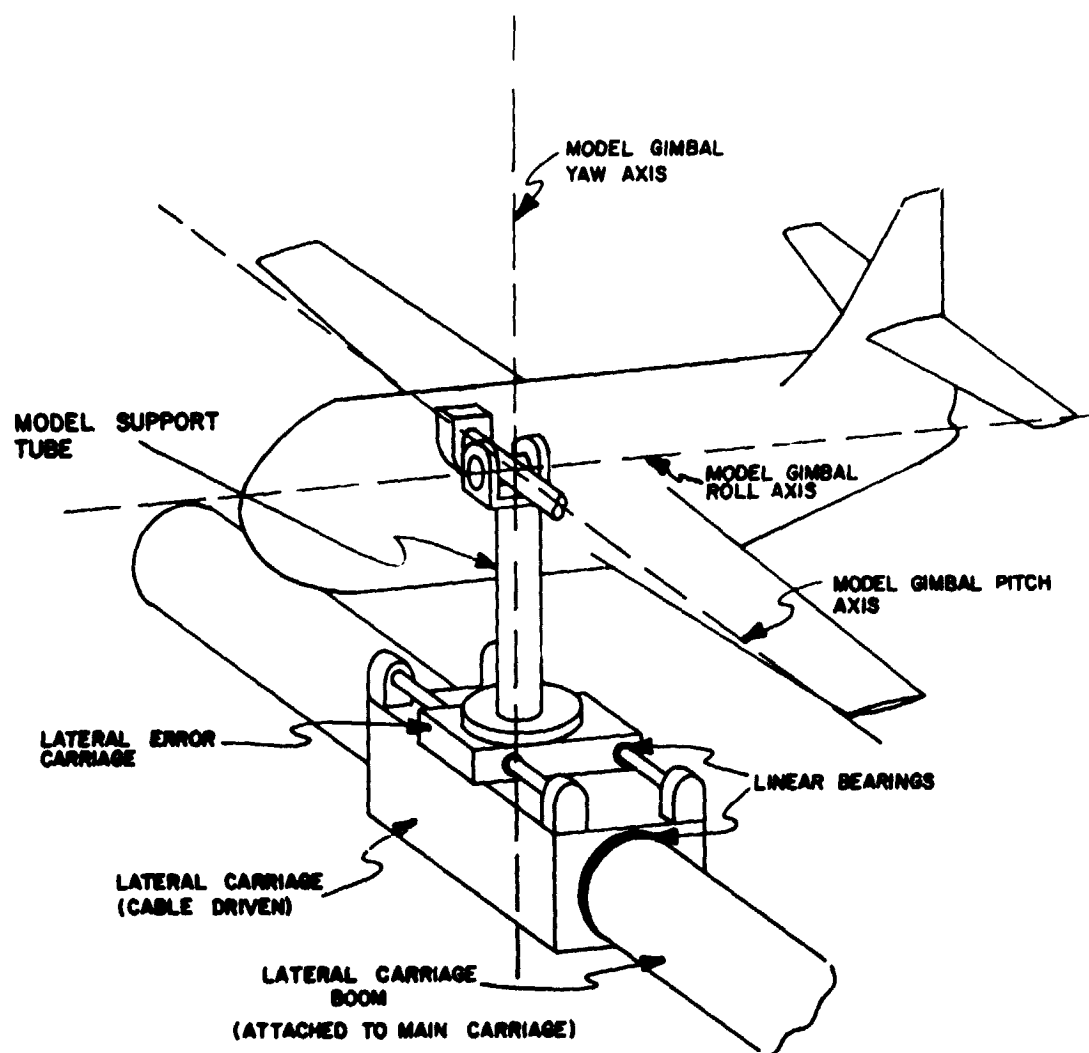


Figure 4.- Schematic representation of lateral carriage system, model support, and gimbal arrangement.






Figure 5.- 0.10 scale dynamic model of XC-142A tilt-wing V/STOL aircraft



Note. Wing Airfoil Section NACA 63-318  
 Angular Travel of Vane =  $1.075 \times$  Angular Travel of Flap  
 All Dimensions Given in Percent Chord at Any Wing Station

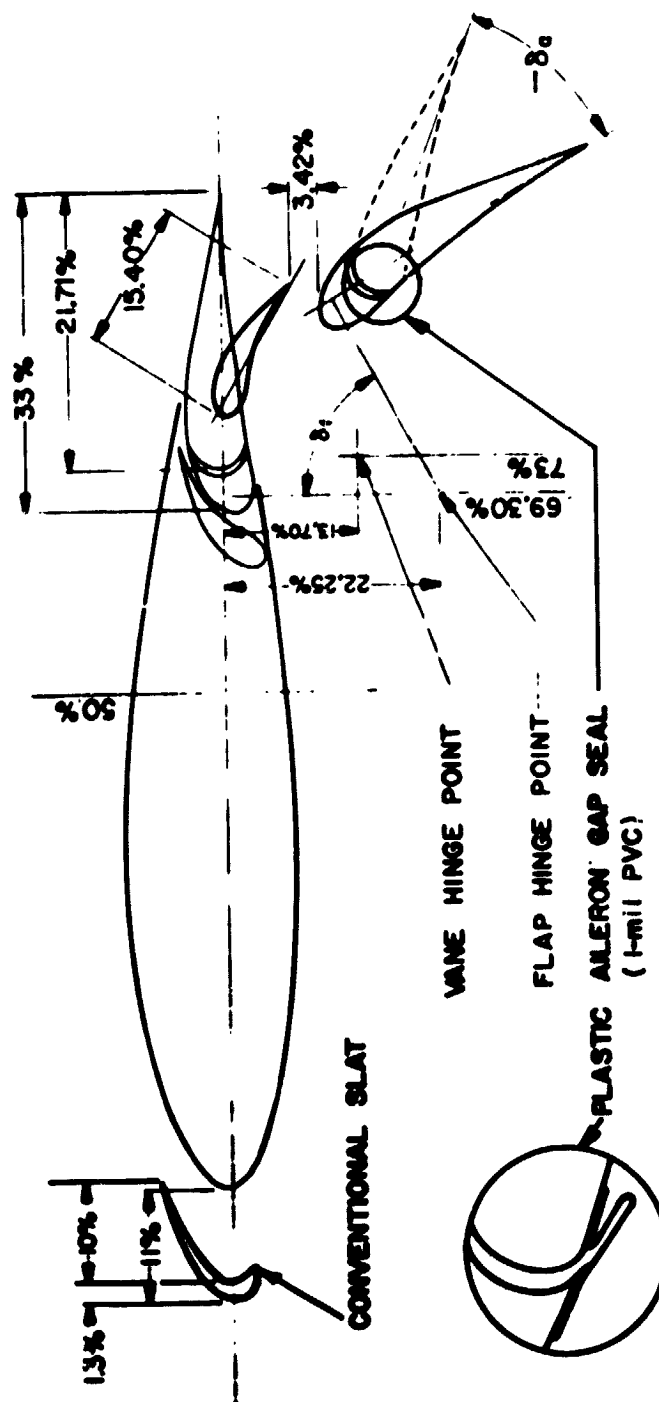


Figure 7.- Model wing airfoil section, showing slat, flap, and aileron arrangement.

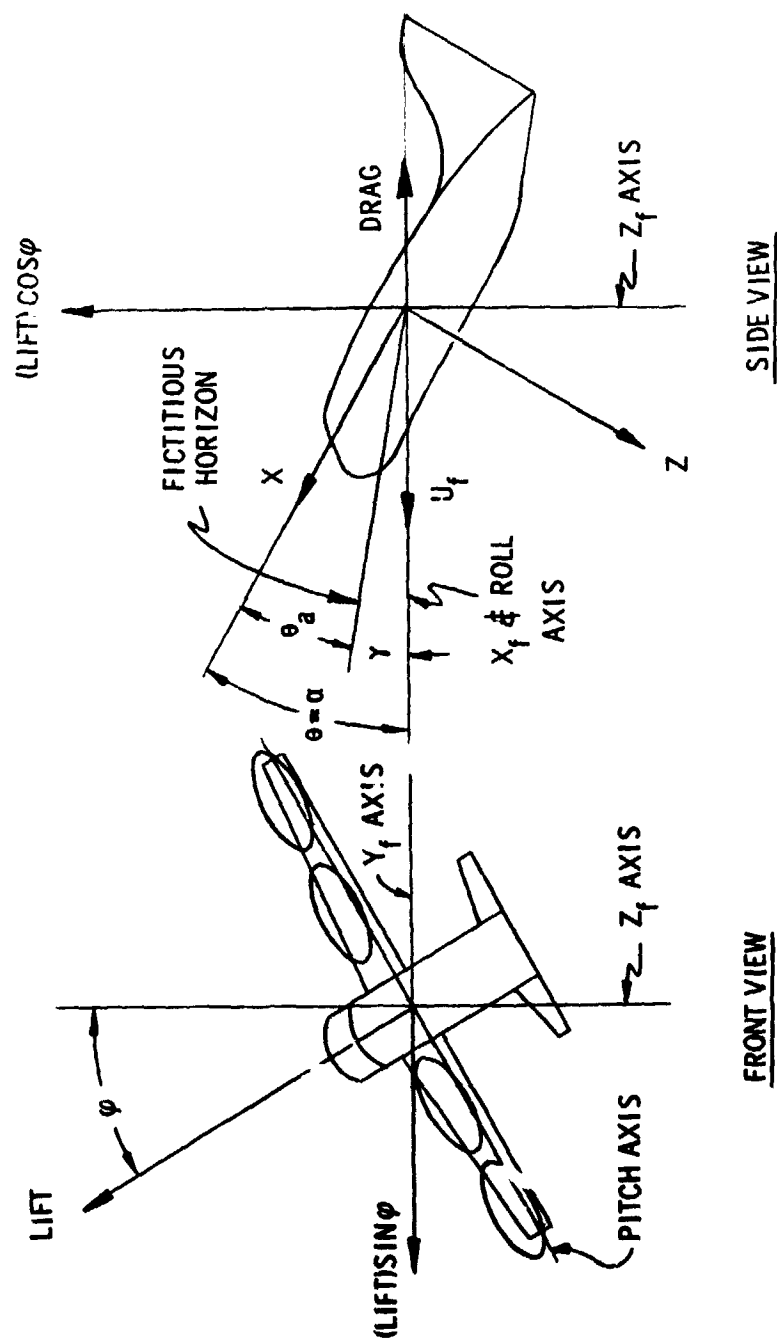


Figure 8.- Diagram for resolution of model forces from static test data.

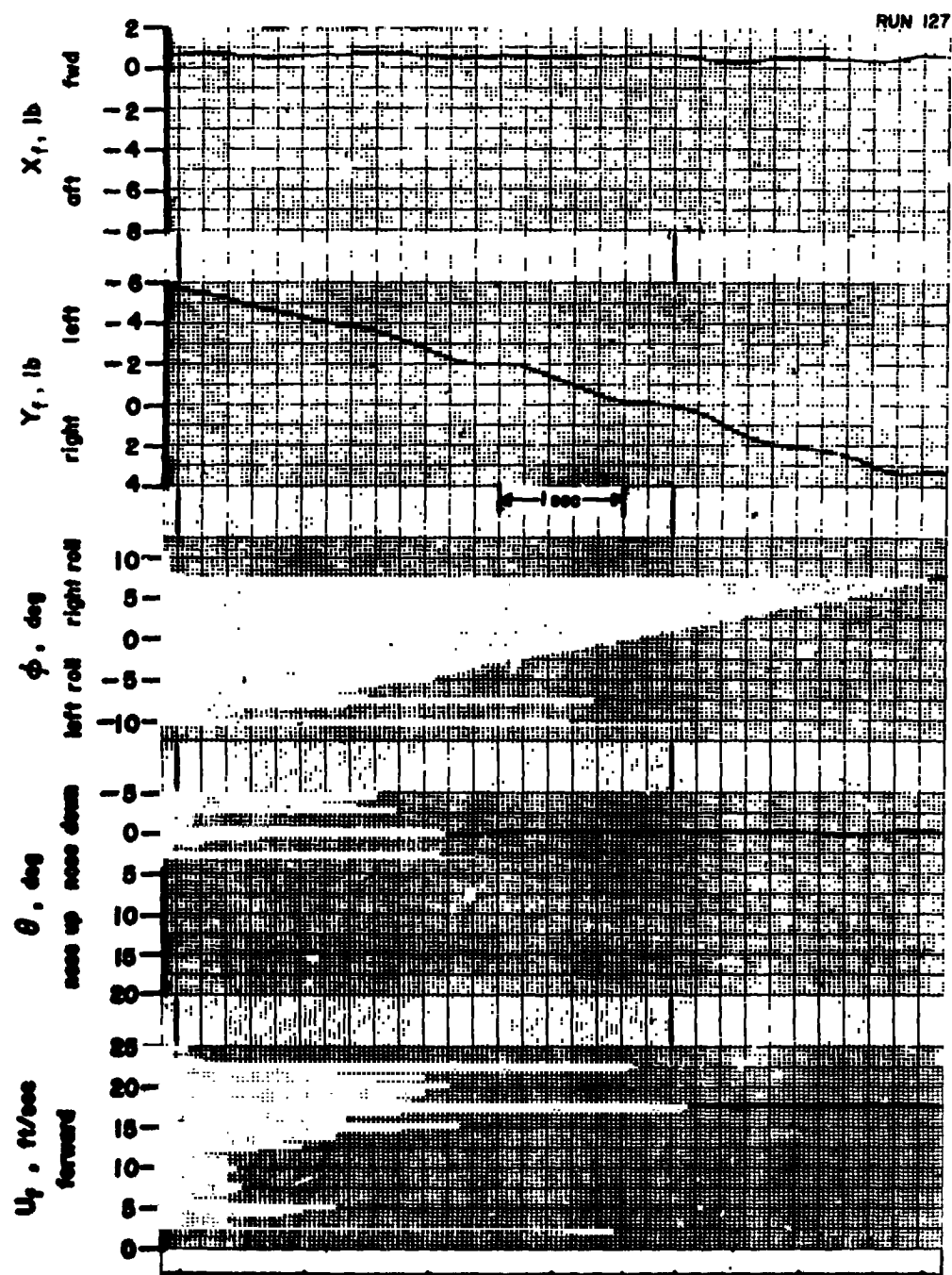


Figure 9.- Static test data; descent condition determination.  
 Ramp input to roll attitude-hold loop.  $\beta_{.75R} = 13.5^\circ$ ,  
 $\delta_a = 0$ , and  $\Delta\beta = 0$ .

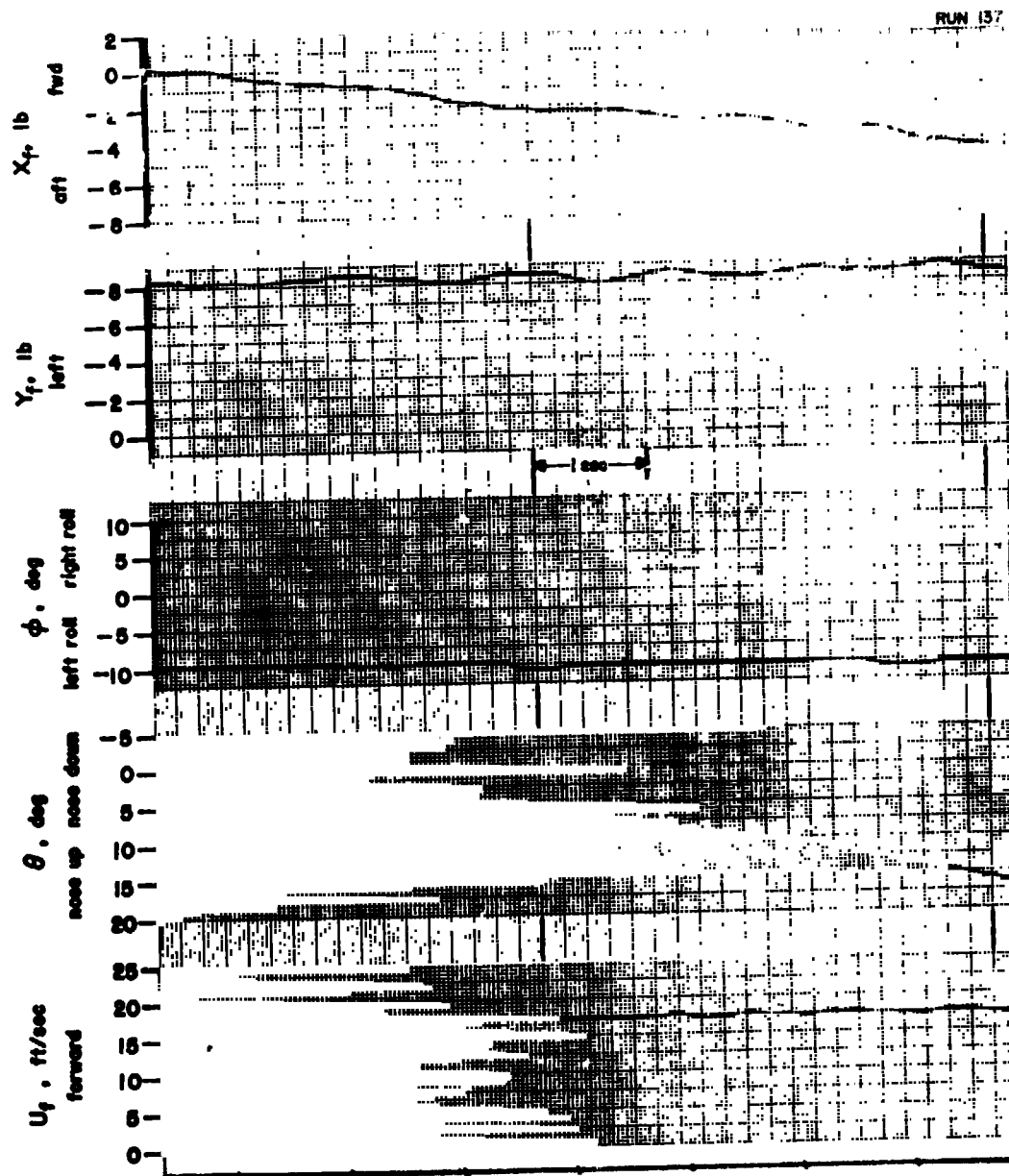


Figure 10.- Static test data; descent condition determination.  
Ramp input to pitch attitude-hold loop.  $\beta_{.75R} = 13.5^\circ$ ,  
 $\delta_a = 0$ , and  $\Delta\beta = 0$ .

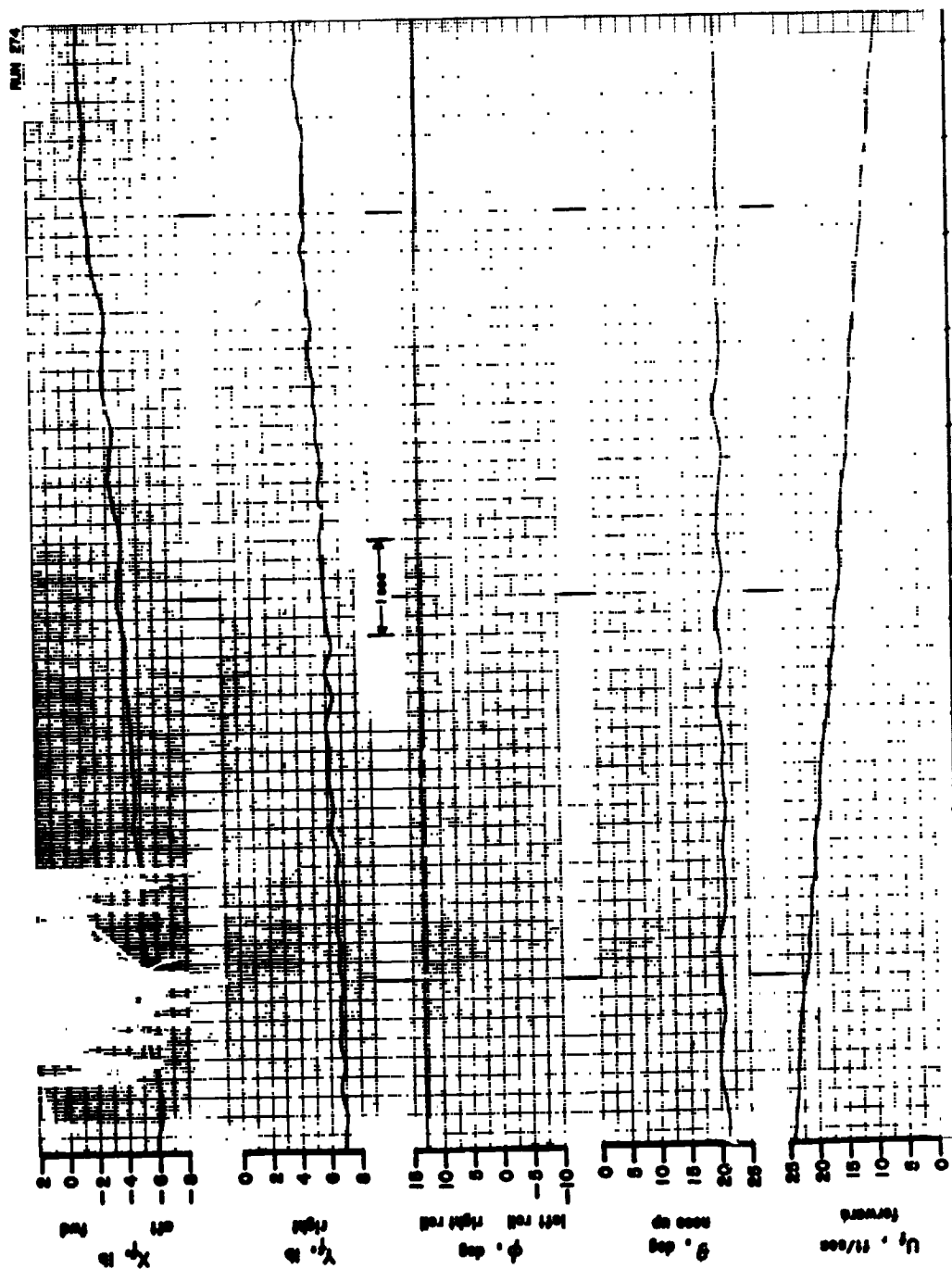


Figure 11.- Static test data; descent condition determination.  
Ramp velocity input.  $\beta = 11.5^\circ$ ,  $\delta_a = 0$ , and  $\Delta\beta = 0$ .

REPRODUCIBILITY OF THE  
ORIGINAL PAGE IS POOR

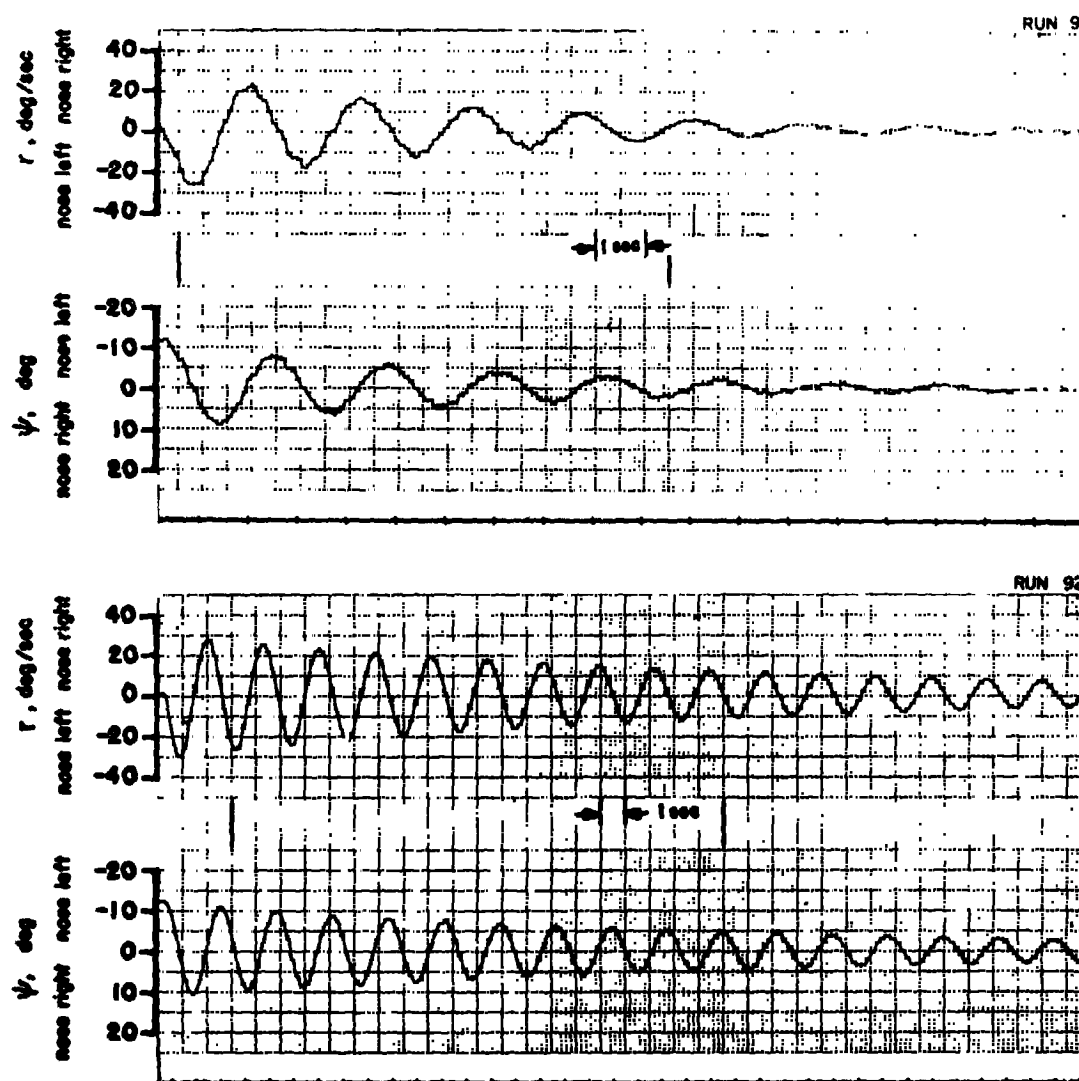


Figure 12.- Dynamic test data; directional transient response.  
One degree-of freedom,  $\psi$ .  $\theta = 0$ ,  $\beta_{75R} = 13.5^\circ$ , and  
 $\gamma = 0$  ( $U_f = 17.8$  and  $0$  ft/sec for runs 91 and 92,  
respectively).



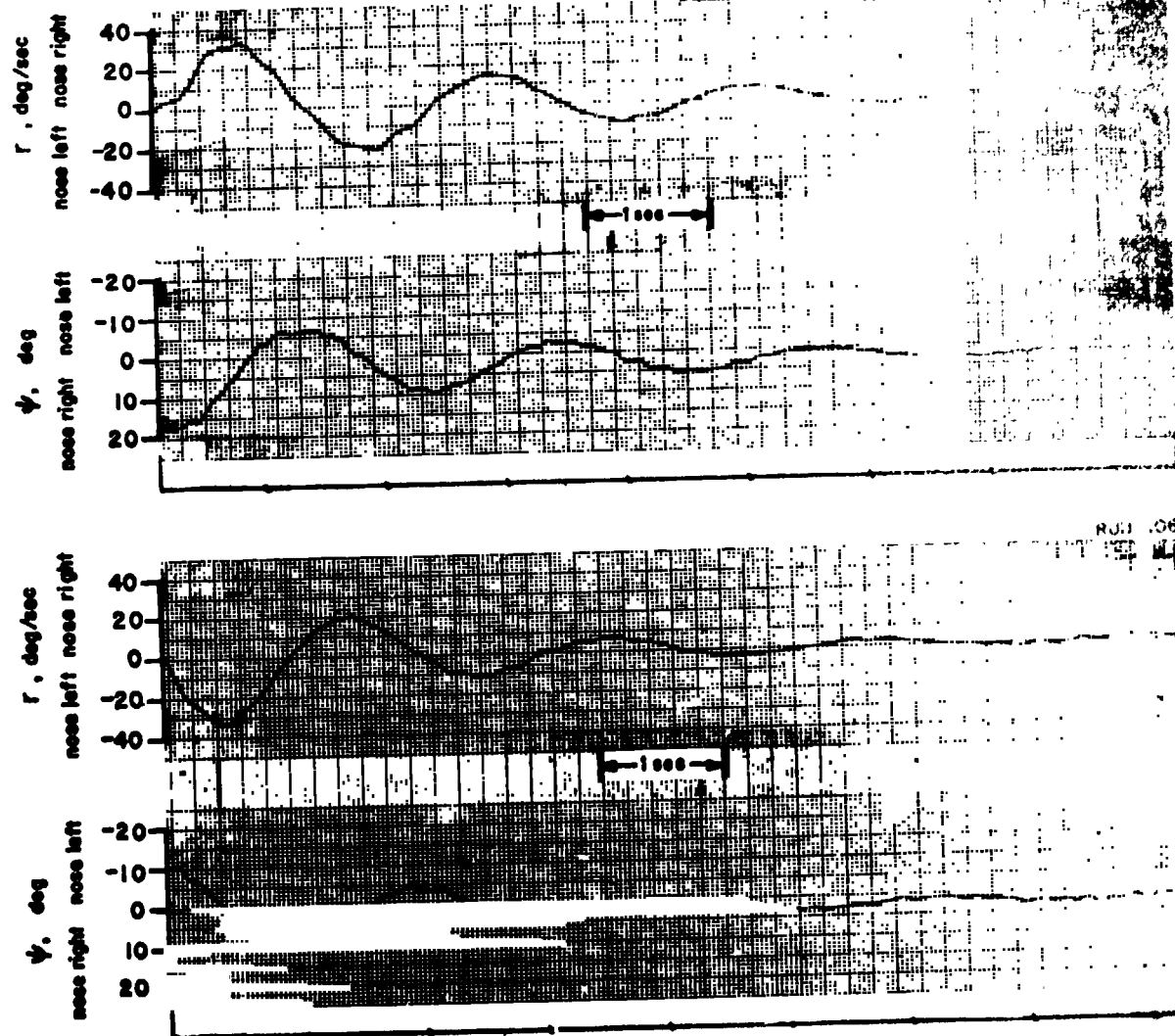


Figure 13.- Dynamic test data; directional transient response.  
 One degree-of-freedom,  $\psi$ .  $\theta = 0$ ,  $\beta.75R = 13.5^\circ$ ,  $\gamma = 0$ ,  
 and  $U_f = 19.4$  ft/sec.

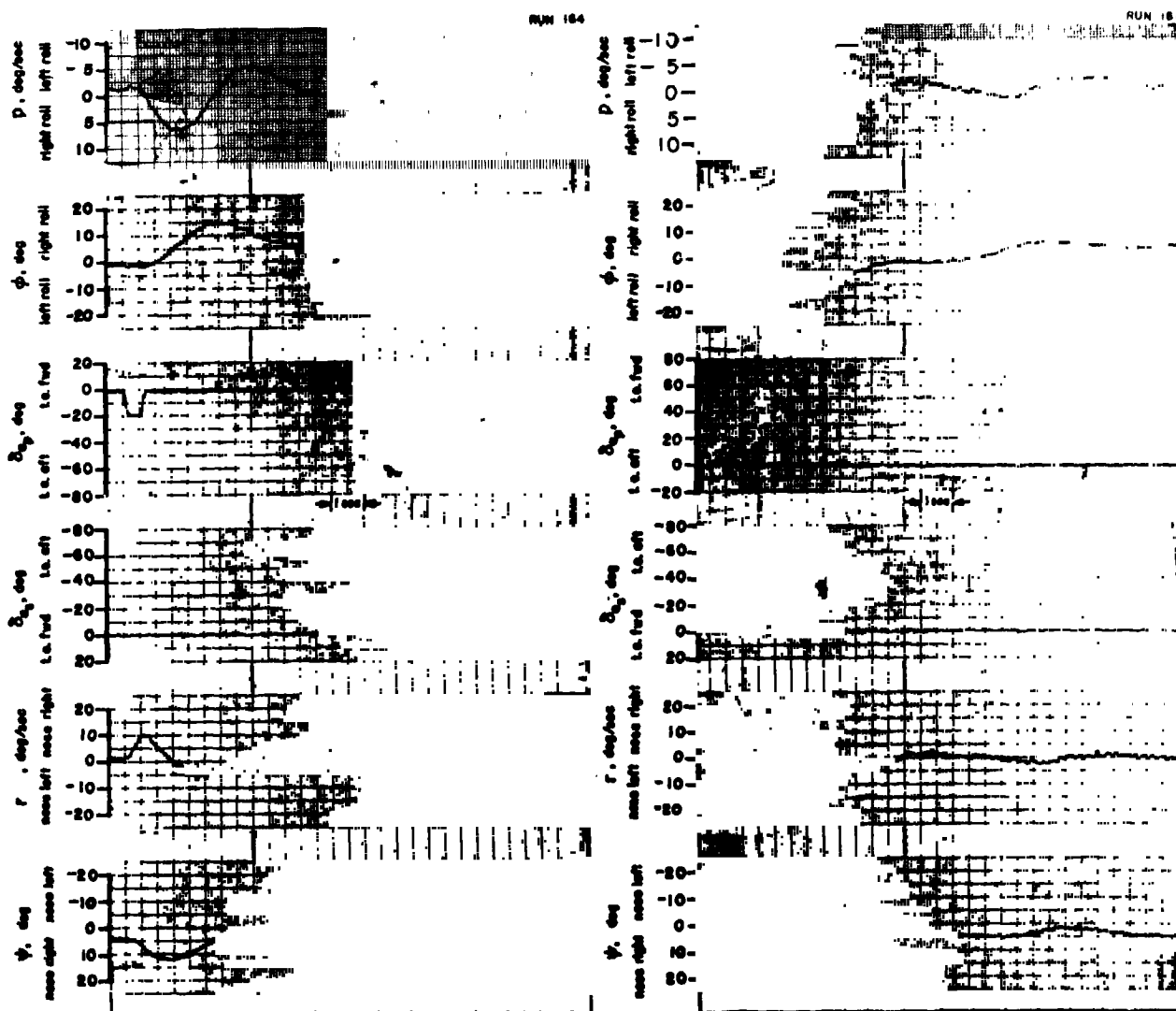


Figure 14.- Dynamic test data; lateral/directional transient response. Two degrees-of-freedom,  $\phi$ - $\psi$ .  $\theta = 0$ ,  $\beta_{.75R} = 13.5^\circ$ ,  $\gamma = 0$ , and  $U_T = 17.6$  ft/sec.

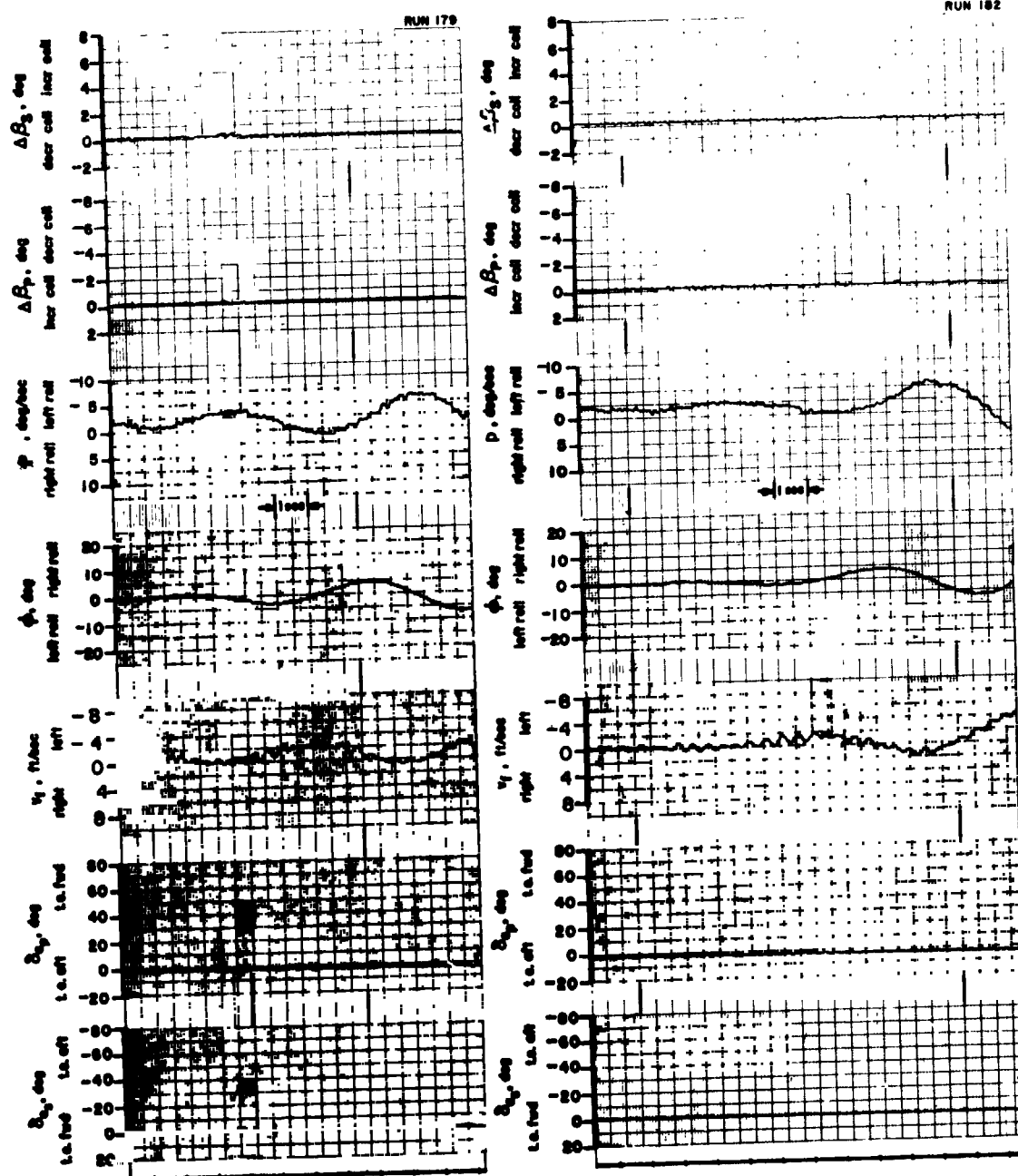


Figure 15.- Dynamic test data; lateral/directional transient response. Two degrees-of-freedom,  $\phi$ - $\psi$ .  $\theta = 0$ ,  $\beta_{.75R} = 13.5^\circ$ ,  $\gamma = 0$ , and  $U_F = 18.4$  ft/sec.

REPRODUCIBILITY OF THE  
ORIGINAL PAGE(S) IN THE

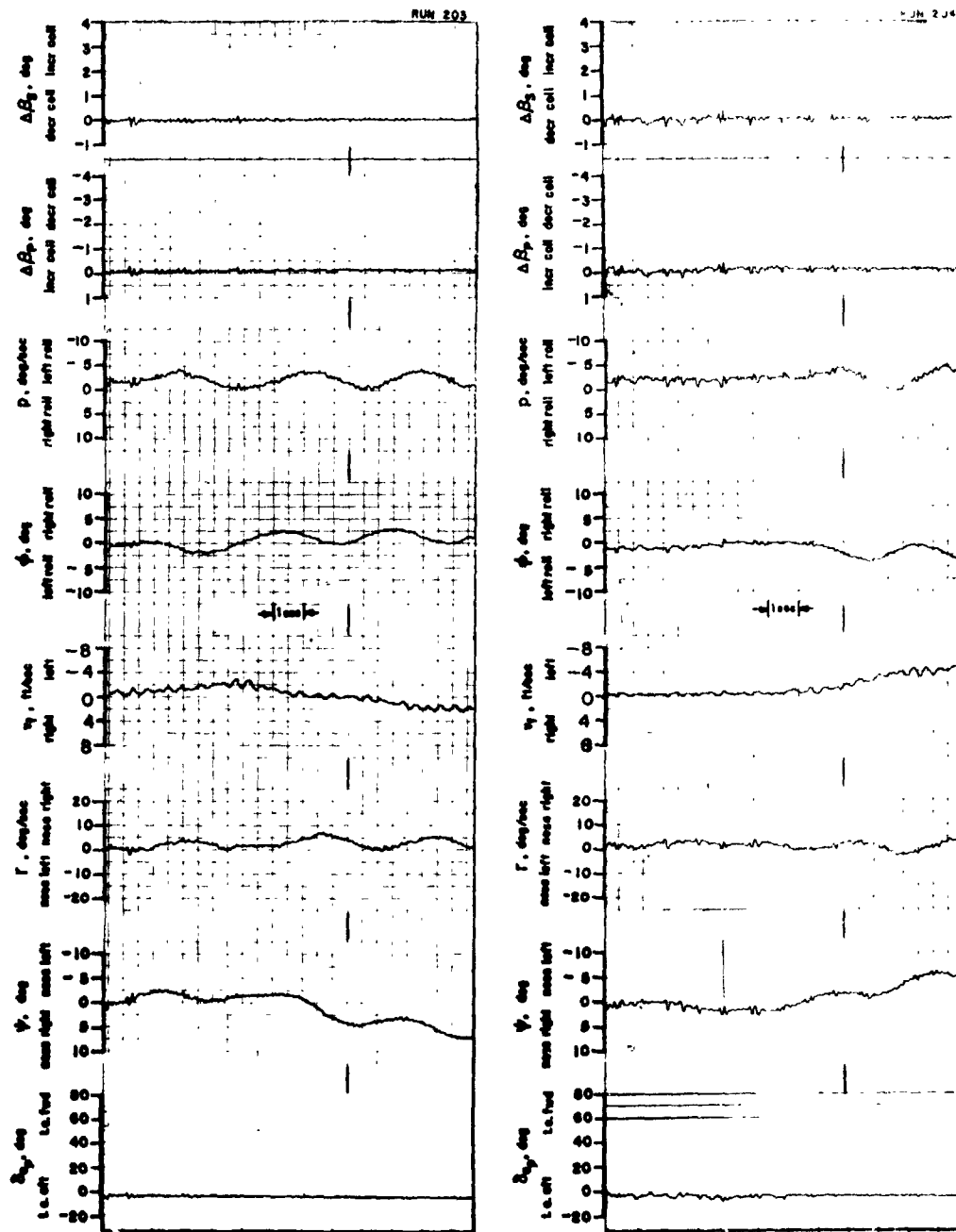


Figure 16.- Dynamic test data; lateral/directional transient response. Three degrees-of-freedom,  $\phi$ - $\psi$ - $v_F$ .  $\theta = 0$ ,  $\beta_{/5R} = 13.5^\circ$ ,  $\gamma = 0$ , and  $U_F = 17.9$  ft/sec.

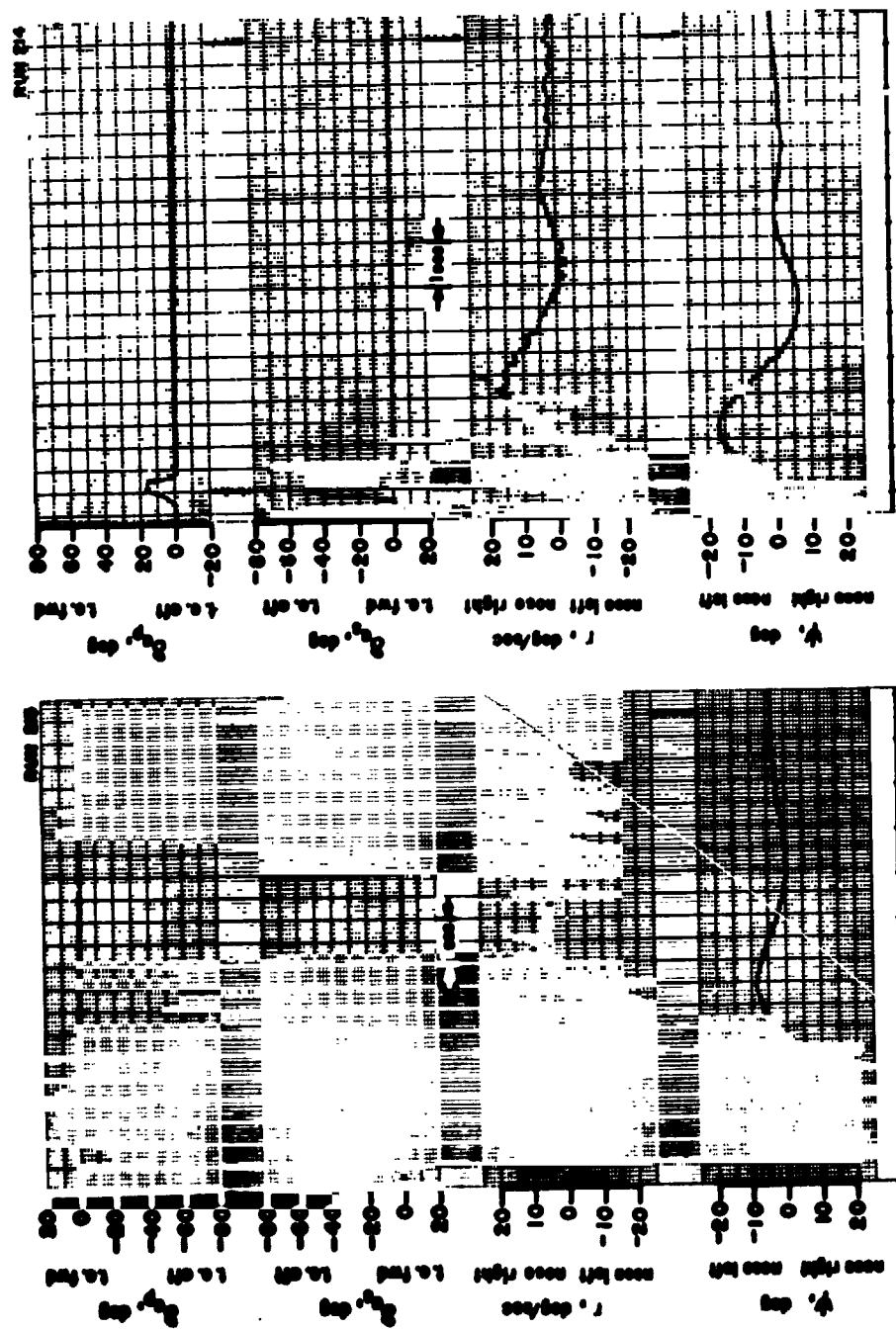


Figure 17.- Dynamic test data; lateral/directional transient response. One degree-of-freedom,  $\psi, \theta = 10^\circ$ ,  $\beta.75R = 13.5^\circ$ ,  $\gamma = -5^\circ$ , and  $U_f = 17.8 \text{ ft/sec}$ .

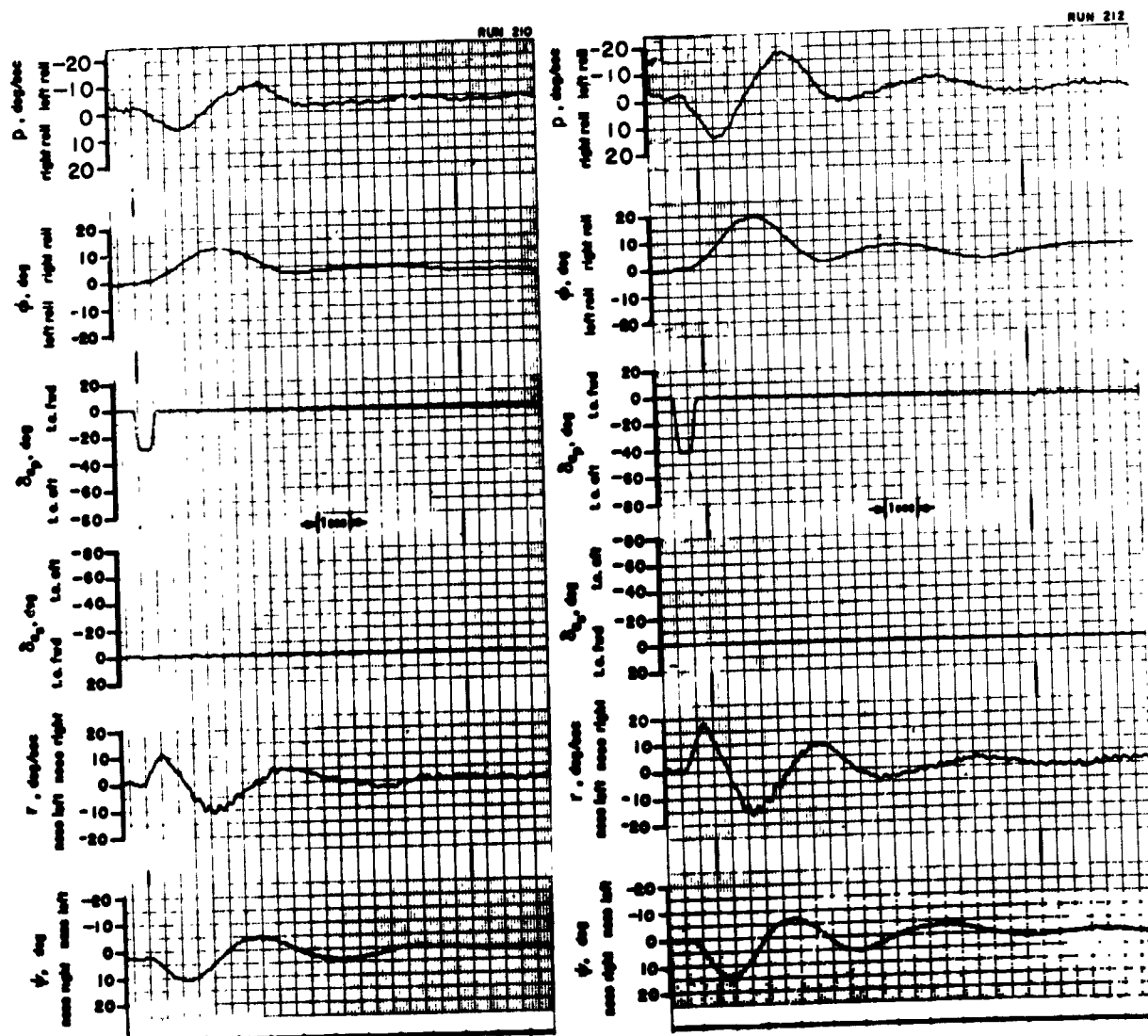


Figure 18.- Dynamic test data; lateral/directional transient response. Two degrees-of-freedom,  $\phi$ - $\psi$ .  $\theta = 10^\circ$ ,  $\beta.75R = 13.5^\circ$ ,  $\gamma = -5^\circ$ , and  $U_F = 17.7$  ft/sec.

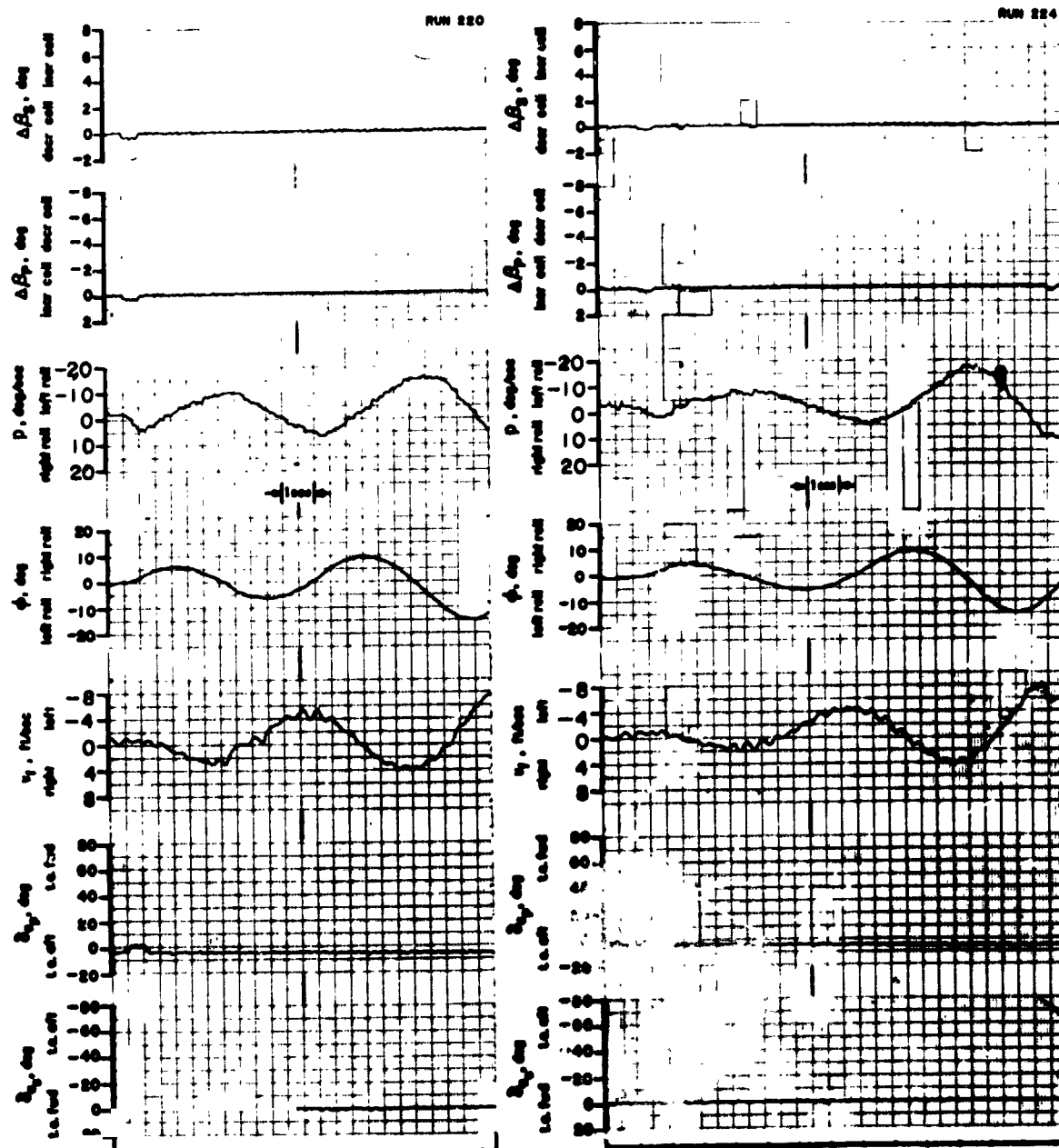


Figure 19.- Dynamic test data; lateral/directional transient response. Two degrees-of-freedom,  $\beta$ -vr.  $\theta = 10^\circ$ ,  $\beta.75R = 13.5^\circ$ ,  $\gamma = -5^\circ$ , and  $U_T = 17.6$  ft/sec.

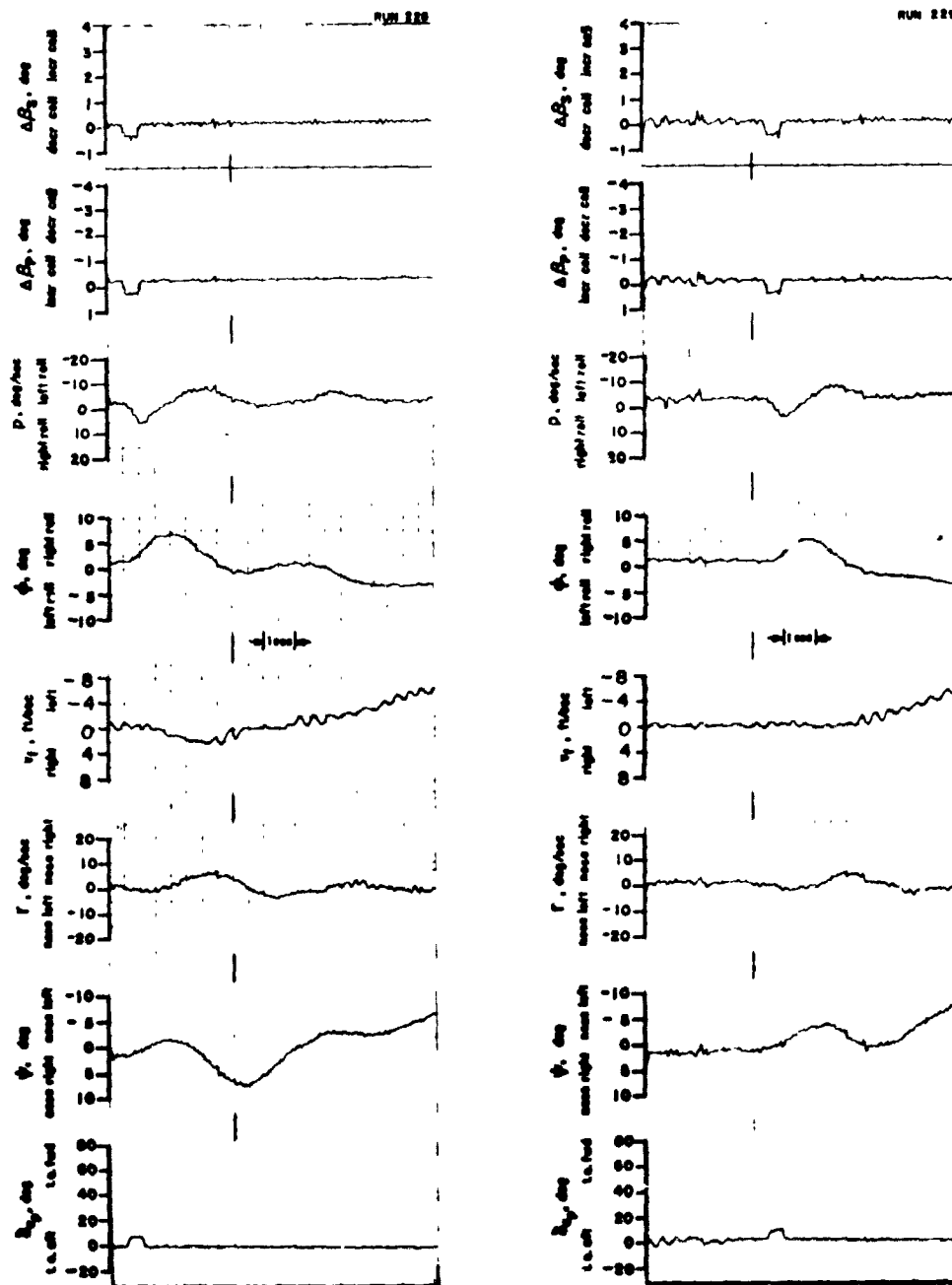


Figure 20.- Dynamic test data; lateral/directional transient response. Three degrees-of-freedom,  $\phi-\psi-v$ .  $\theta = 10^\circ$ ,  $\beta.75R = 13.5^\circ$ ,  $\gamma = -5^\circ$ , and  $U_T = 18.4$  ft/sec.



REPRODUCIBILITY OF THE  
ORIGINAL PAGE IS POOR

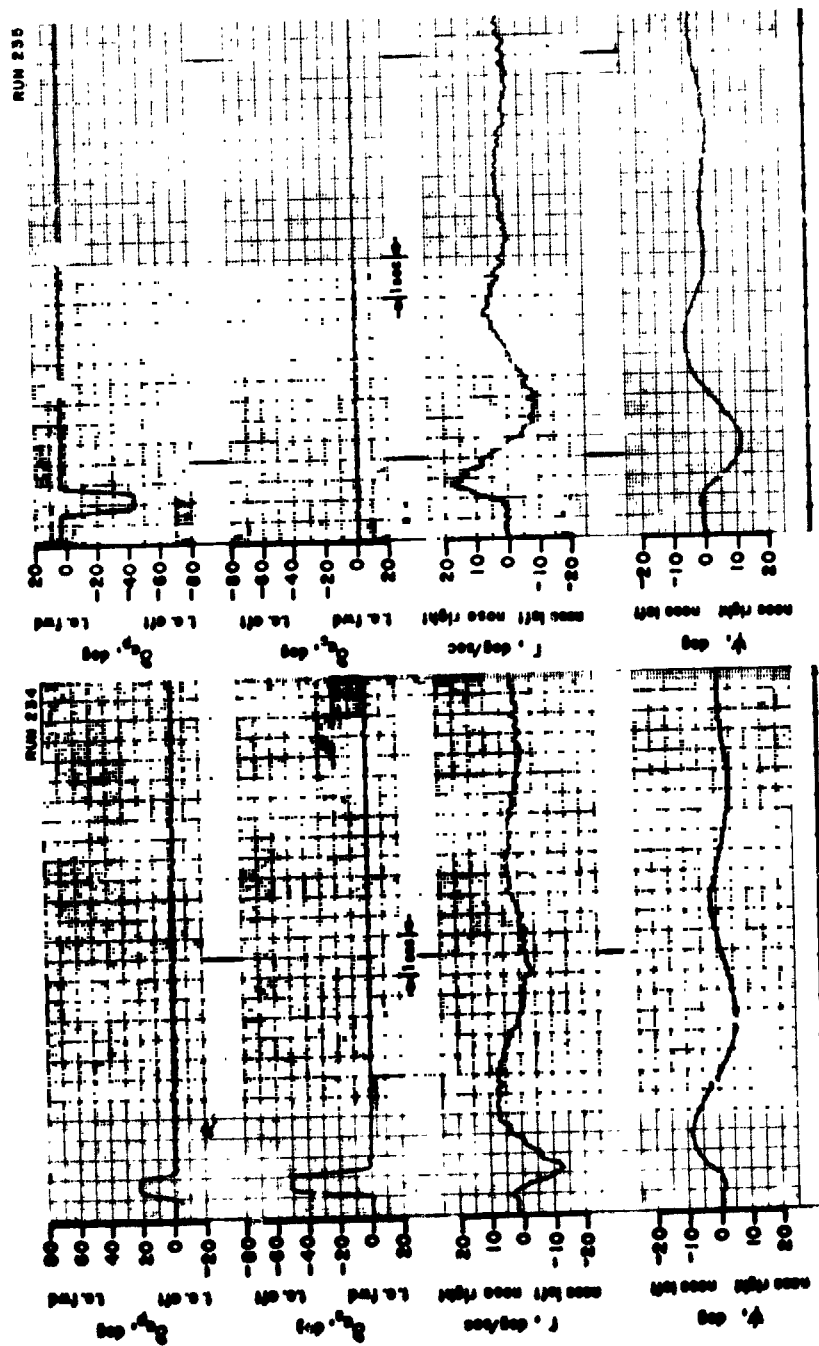


Figure 21.- Dynamic test data; lateral/directional transient response. One degree-of-freedom,  $\psi$ ,  $\theta = 20^\circ$ ,  $\beta.75R = 13.5^\circ$ ,  $\gamma = -11^\circ$ , and  $U_f = 18.6$  ft/sec.

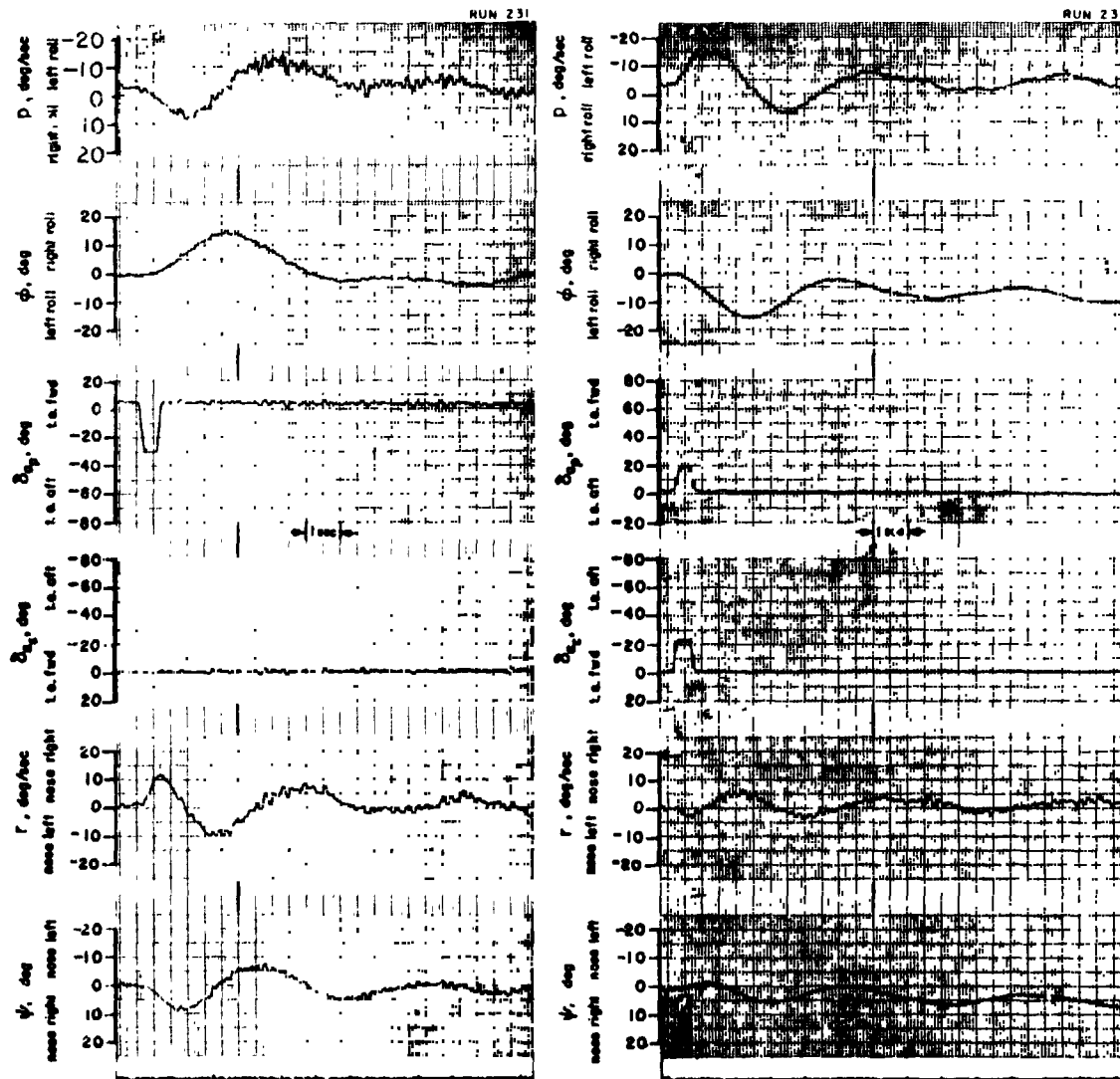


Figure 22.- Dynamic test data; lateral/directional transient response. Twodegrees-of-freedom,  $\phi$ - $\psi$ .  $\theta = 20^\circ$ ,  $\beta_{.75R} = 15.5^\circ$ ,  $\gamma = -11^\circ$ , and  $U_F = 18.6$  ft/sec.

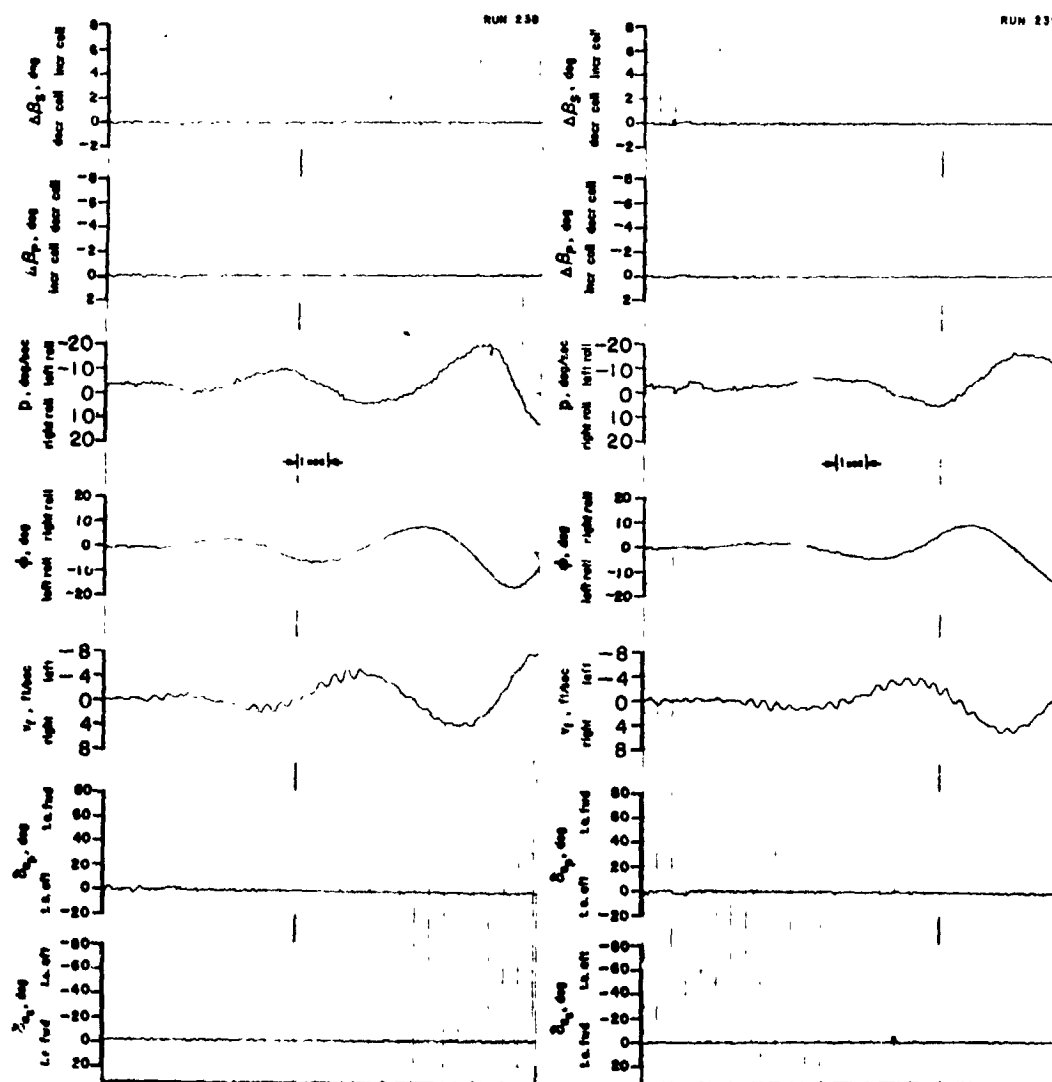


Figure 23.- Dynamic test data; lateral/directional transient response. Two degrees-of-freedom,  $\phi$ - $v$ .  $\theta = 20^\circ$ ,  $\beta_{.75R} = 13.5^\circ$ ,  $\gamma = -11^\circ$ , and  $U_F = 18.4$  ft/sec.

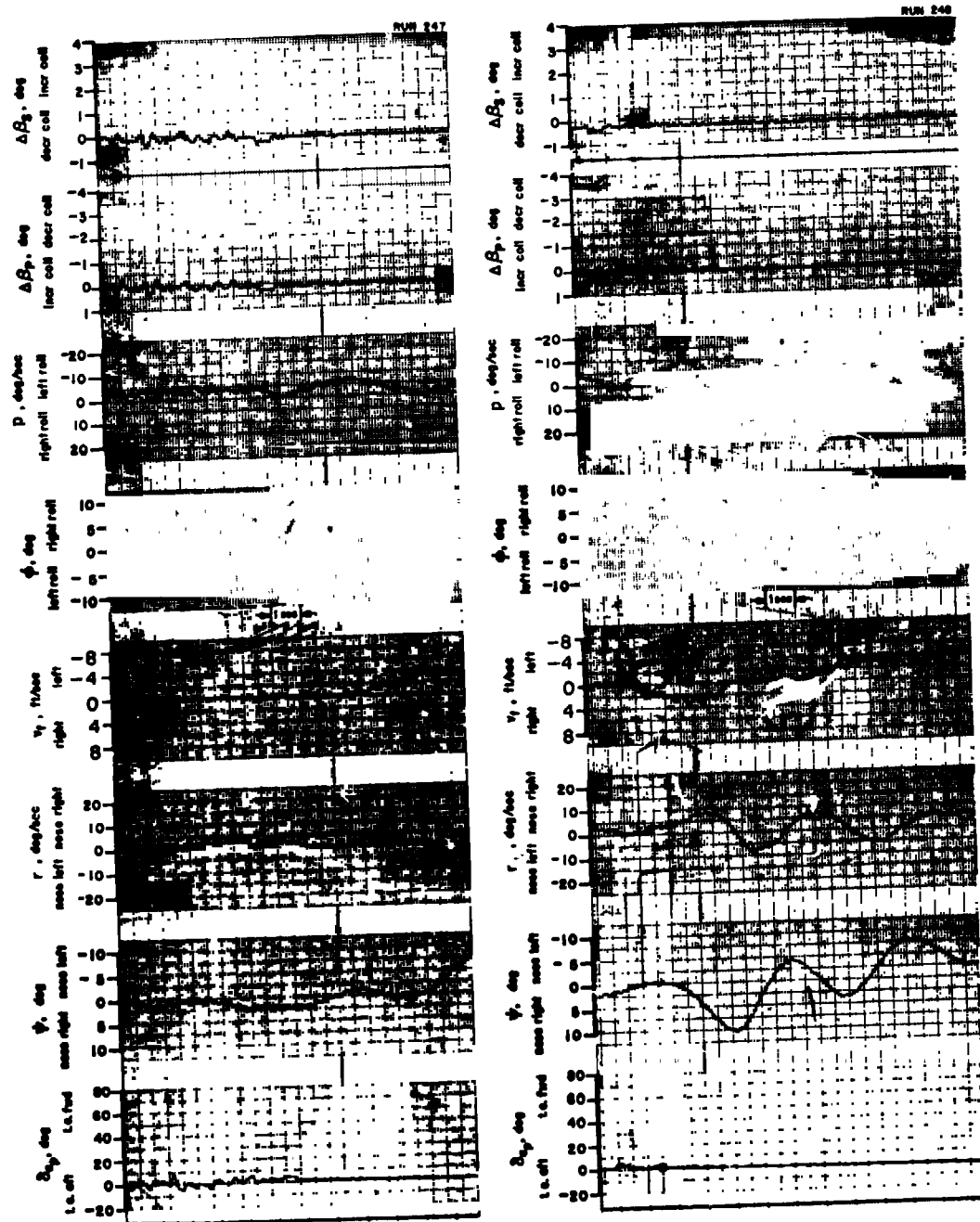


Figure 24.- Dynamic test data; lateral/directional transient response. Three degrees-of-freedom,  $\phi-\psi-v_r$ .  $\theta = 20^\circ$ ,  $\beta_{75R} = 13.5^\circ$ ,  $\gamma = -11^\circ$ , and  $U_F = 18.4$  ft/sec.

REPRODUCIBILITY OF THE  
ORIGINAL PAGE IS POOR

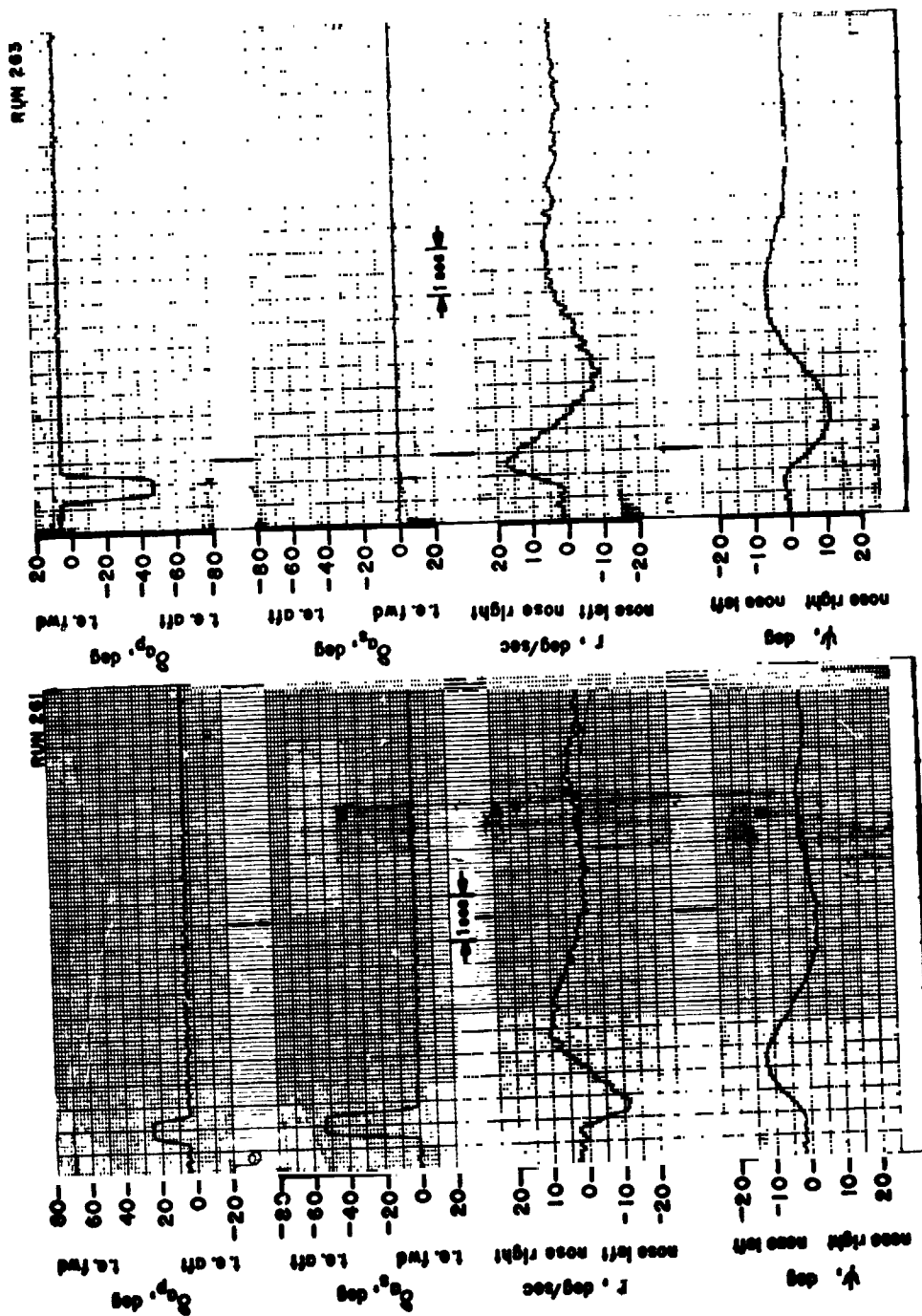


Figure 25.- Dynamic test data; lateral/directional transient response. One degree-of-freedom,  $\psi$ .  
 $\theta = 20^\circ$ ,  $\beta_{.75R} = 11.5^\circ$ ,  $\gamma = -11^\circ$ , and  
 $U_f = 18.1$  ft/sec.

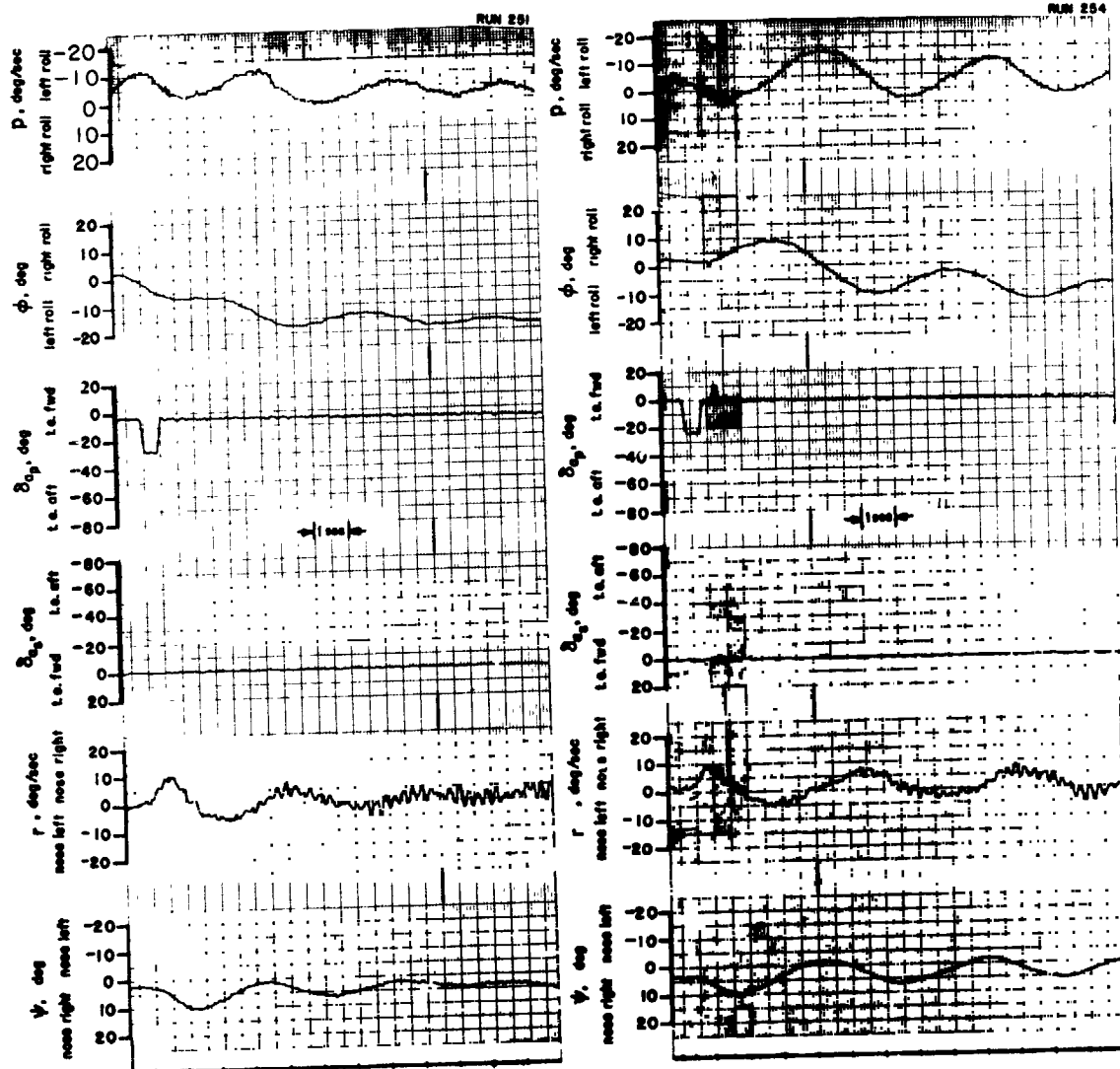


Figure 26.- Dynamic test data; lateral/directional transient response.  
Two degrees-of-freedom,  $\phi$ - $\psi$ .  $\theta = 20^\circ$ ,  $\beta.75R = 11.5^\circ$ ,  $\gamma = -11^\circ$ ,  
and  $U_F = 18.8$  ft/sec.

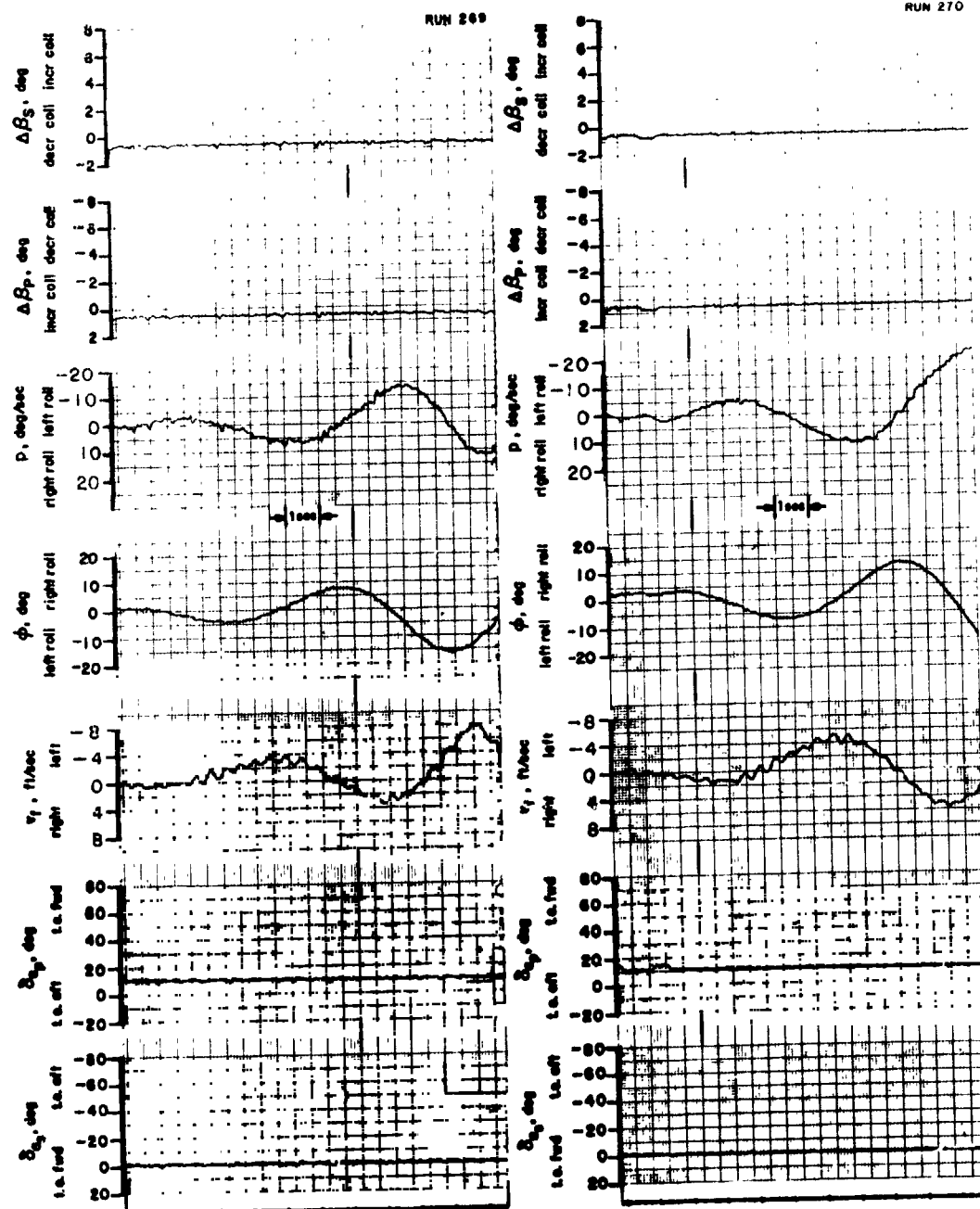


Figure 27.- Dynamic test data; lateral/directional transient response.  
Two degrees-of-freedom,  $\phi-v_F$ .  $\theta = 20^\circ$ ,  $\beta_{.75R} = 11.5^\circ$ ,  $\gamma = -11^\circ$ ,  
and  $v_F = 18.4$  ft/sec.

REPRODUCIBILITY OF THE  
ORIGINAL PAGE IS POOR

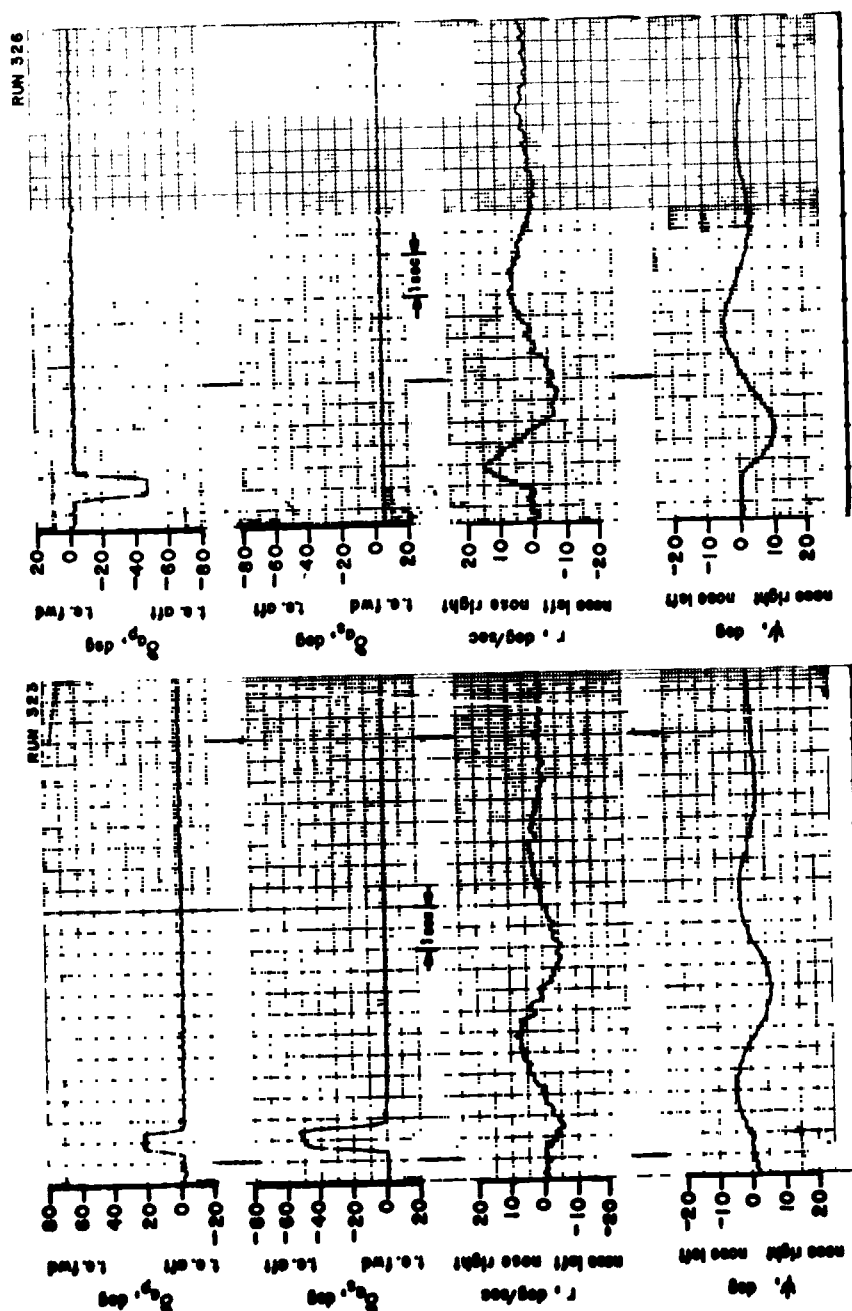


Figure 28.- Dynamic test data; lateral/directional transient response.  
One degree-of-freedom,  $\psi$ ,  $\theta = 20^\circ$ ,  $\beta = 11.5^\circ$ ,  $\gamma = -11^\circ$ , and  
 $U_f = 23.5$  ft/sec.



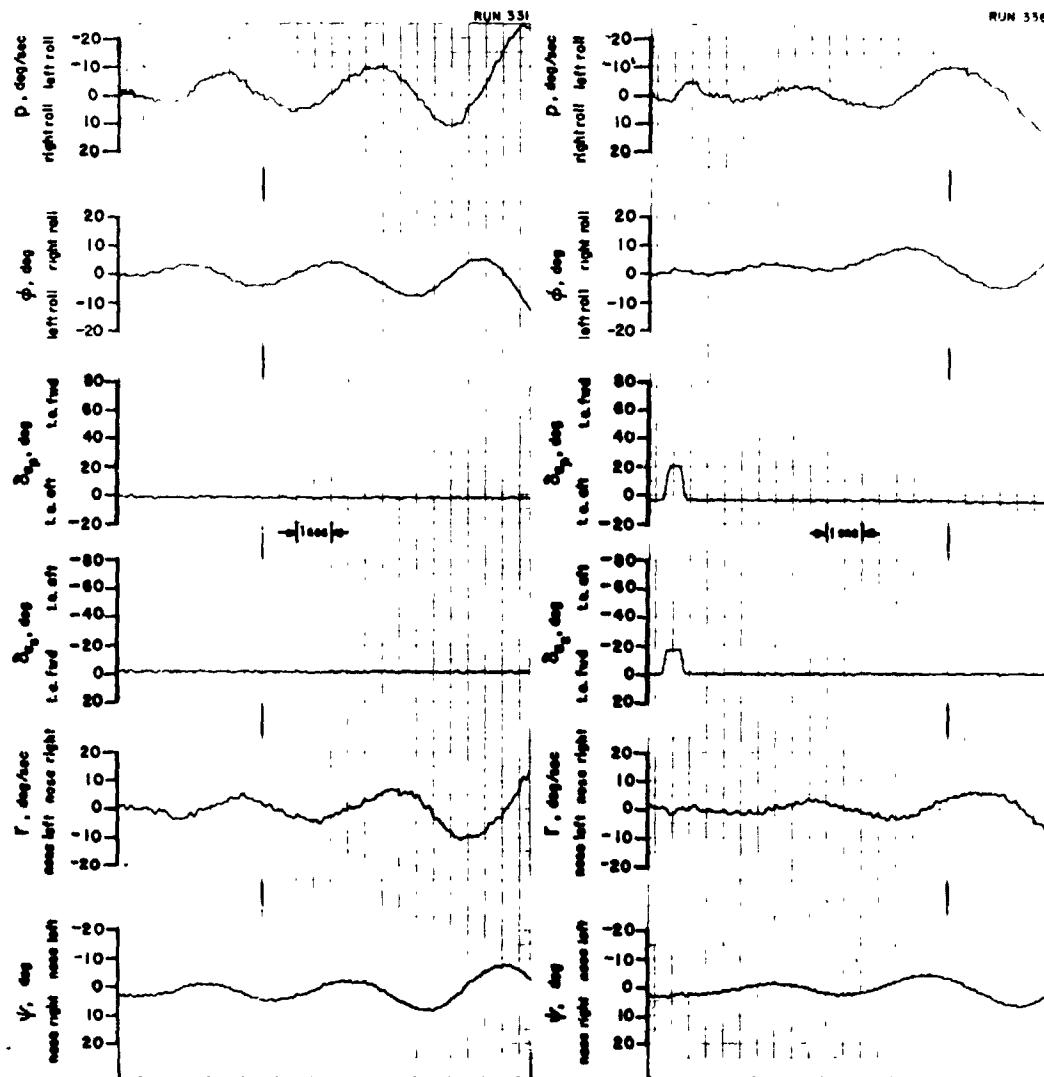


Figure 29.- Dynamic test data; lateral/directional transient response.  
 Two degrees-of-freedom,  $\phi$ - $\psi$ .  $\theta = 20^\circ$ ,  $B_{.75R} = 11.5^\circ$ ,  $\gamma = -11^\circ$ ,  
 and  $U_F = 24$  ft/sec.

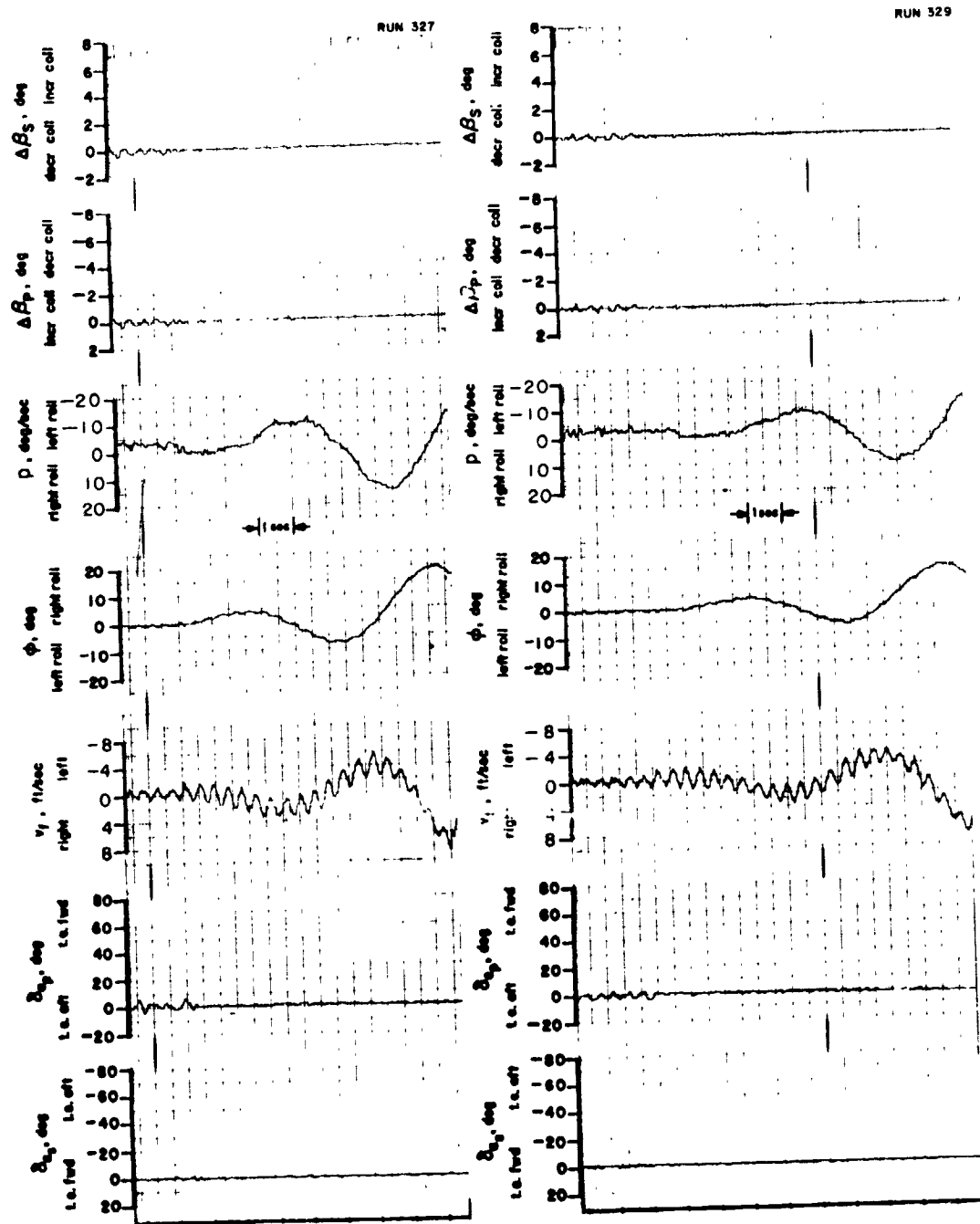


Figure 30.- Dynamic test data; lateral/directional transient response. Two degrees-of-freedom,  $\phi$ - $v_f$ .  $\theta = 20^\circ$ ,  $\beta_{.75R} = 11.5^\circ$ ,  $\gamma = -11^\circ$ , and  $U_f = 23.6$  ft/sec.

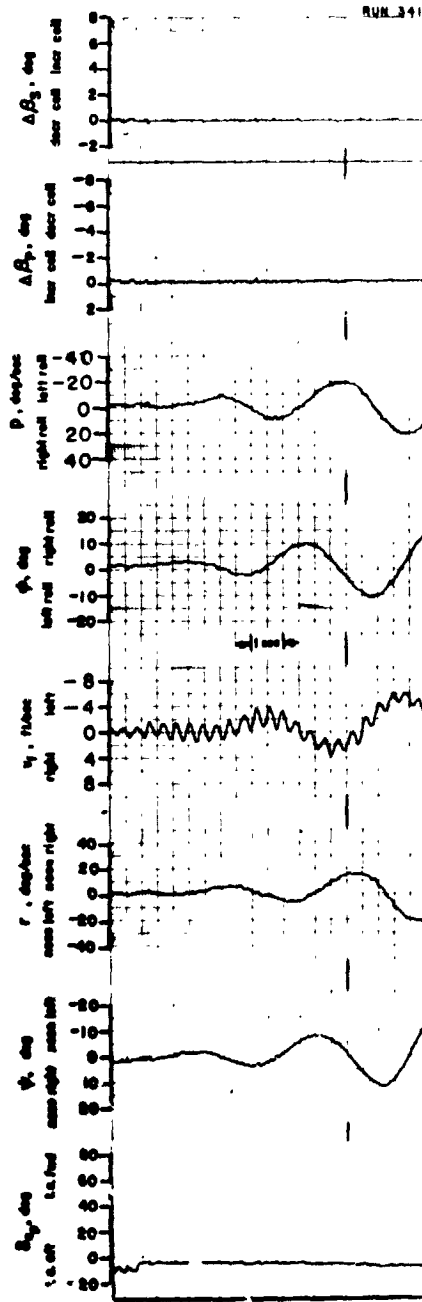
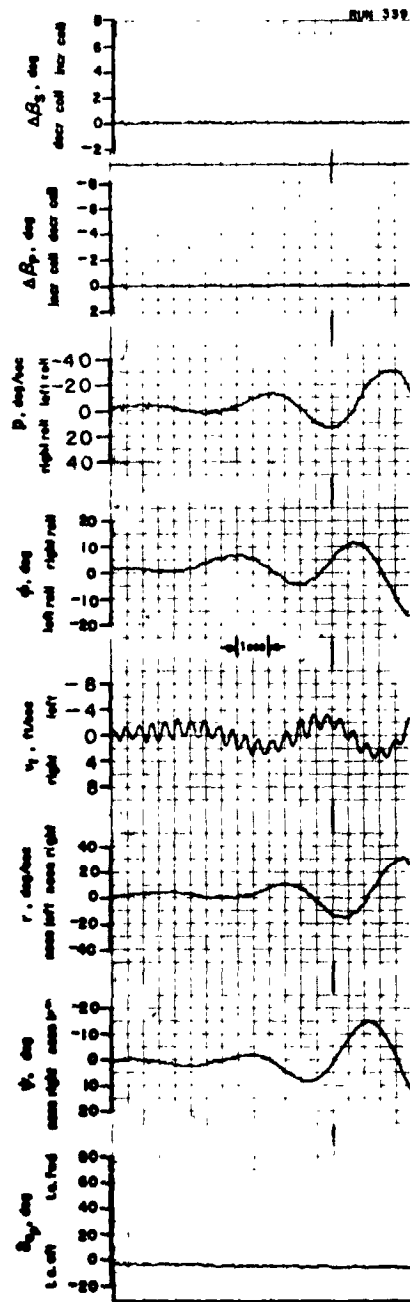


Figure 31.- Dynamic test data; lateral/directional transient response.  
 Three degrees-of-freedom,  $\phi$ - $\psi$ - $v_r$ .  $\theta = 20^\circ$ ,  $\beta_{.75R} = 11.5^\circ$ ,  
 $\gamma = -11^\circ$ , and  $U_r = 23.6$  ft/sec.

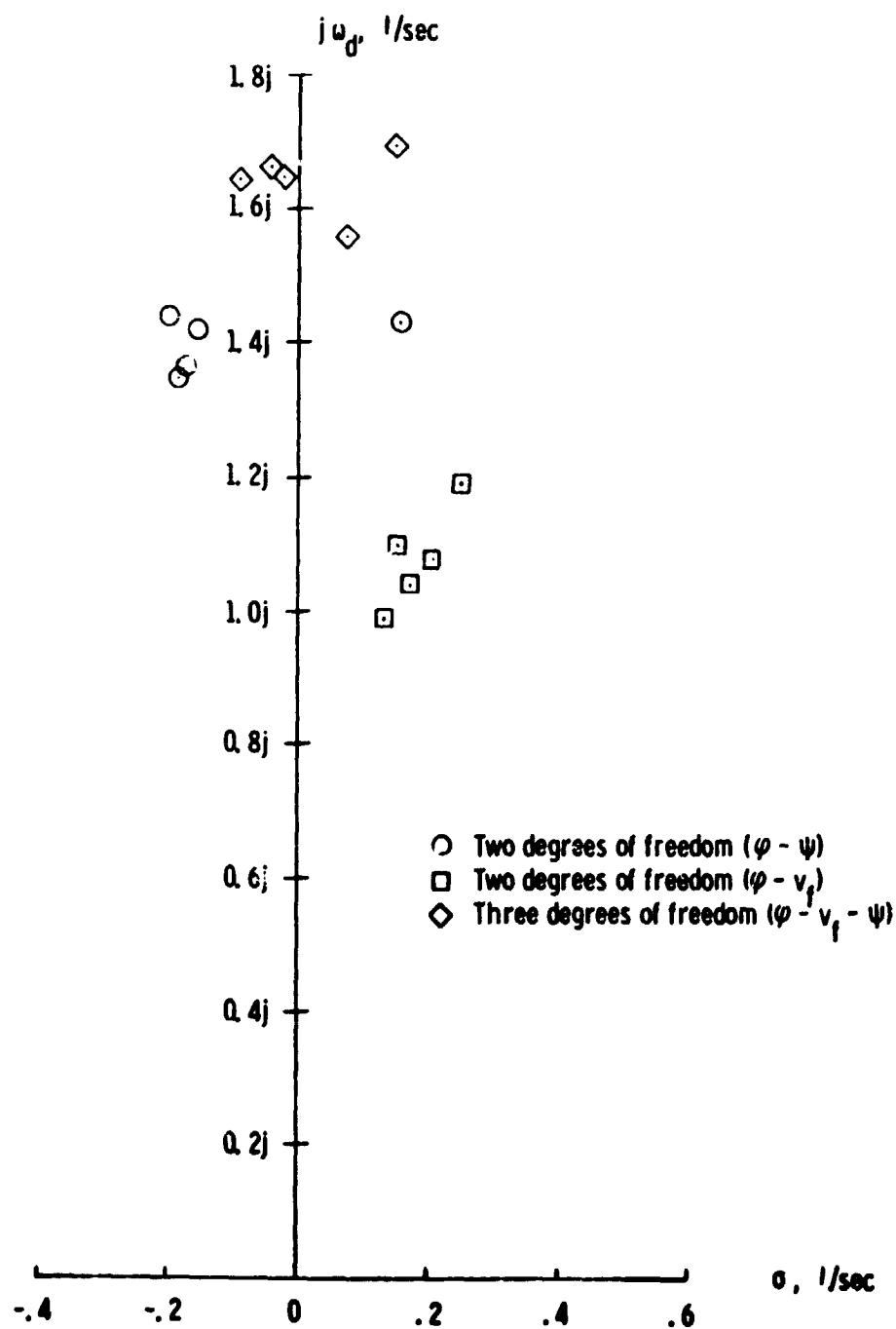


Figure 32.- Summary of model transient response data.  
( $\sigma + j\omega_d$  only root shown.)

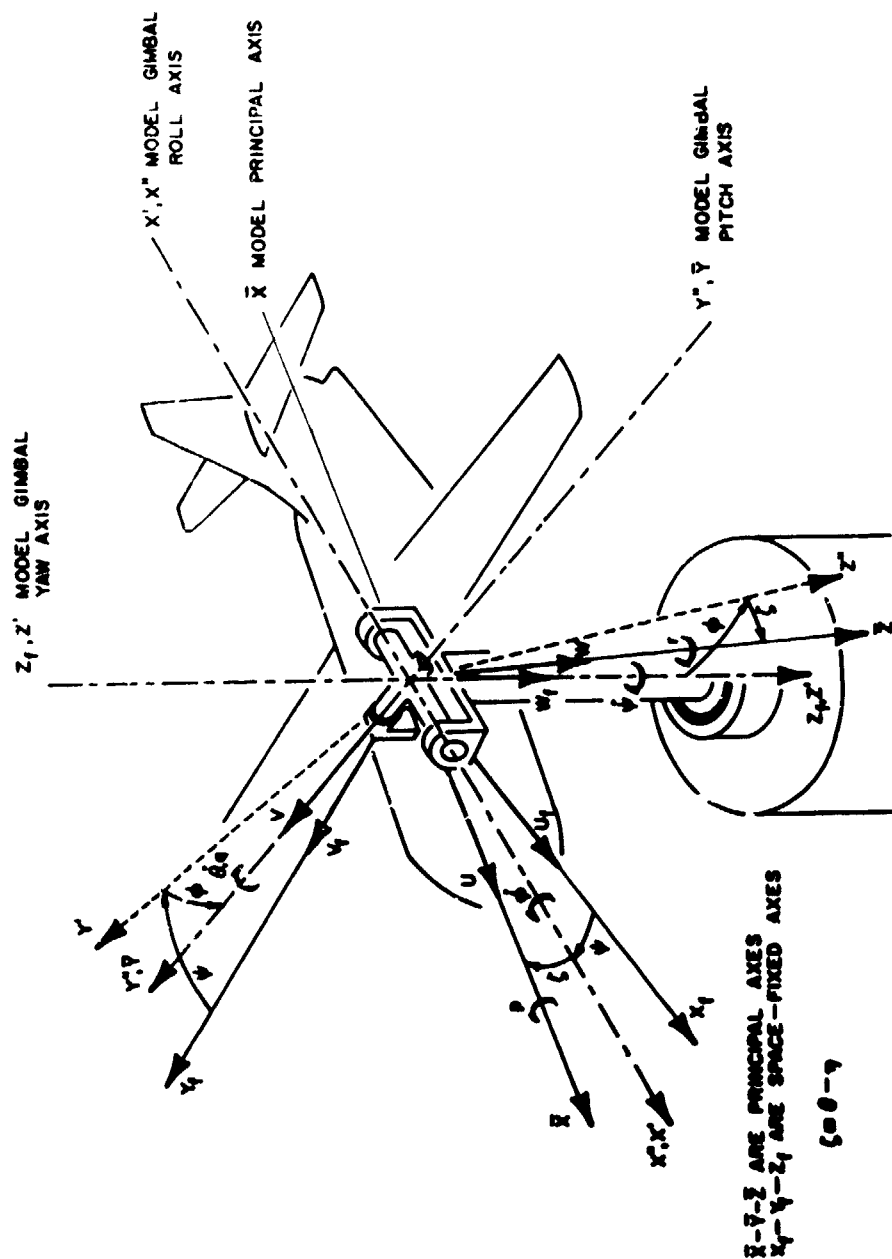


Figure 33.- Model axes systems and variables for lateral/directional descent tests.

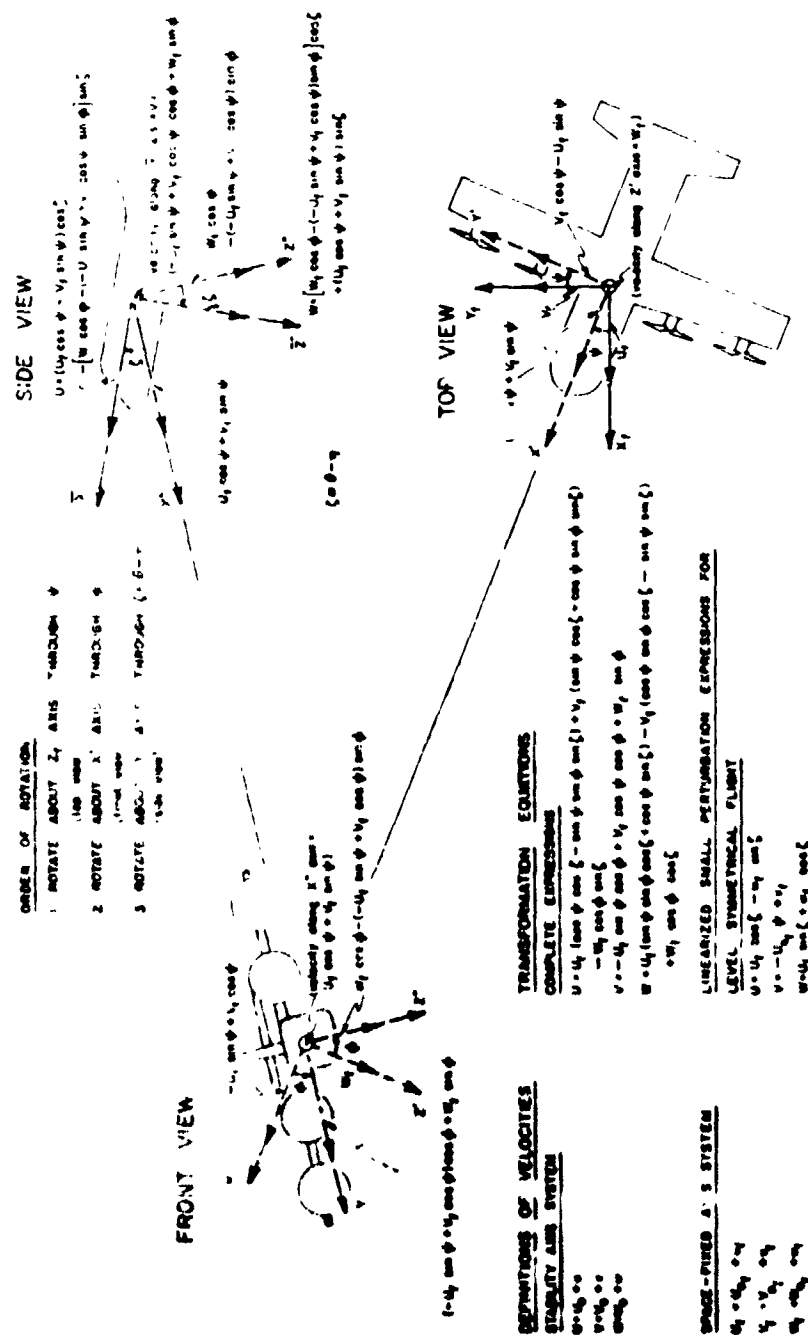


Figure 34.- Transformation of linear velocities from space-fixed to stability axis system for tilt-wing model gimbal system.

$\Phi - \psi$  mode data

$$\frac{\Phi}{\psi} = -0.63 - j 1.34$$

$$S = -0.17 + j 1.36$$

$\Phi$  lags  $\psi$  by  $115^\circ$

$$\frac{\Phi}{\psi} \text{ magnitude ratio} = 1.48$$

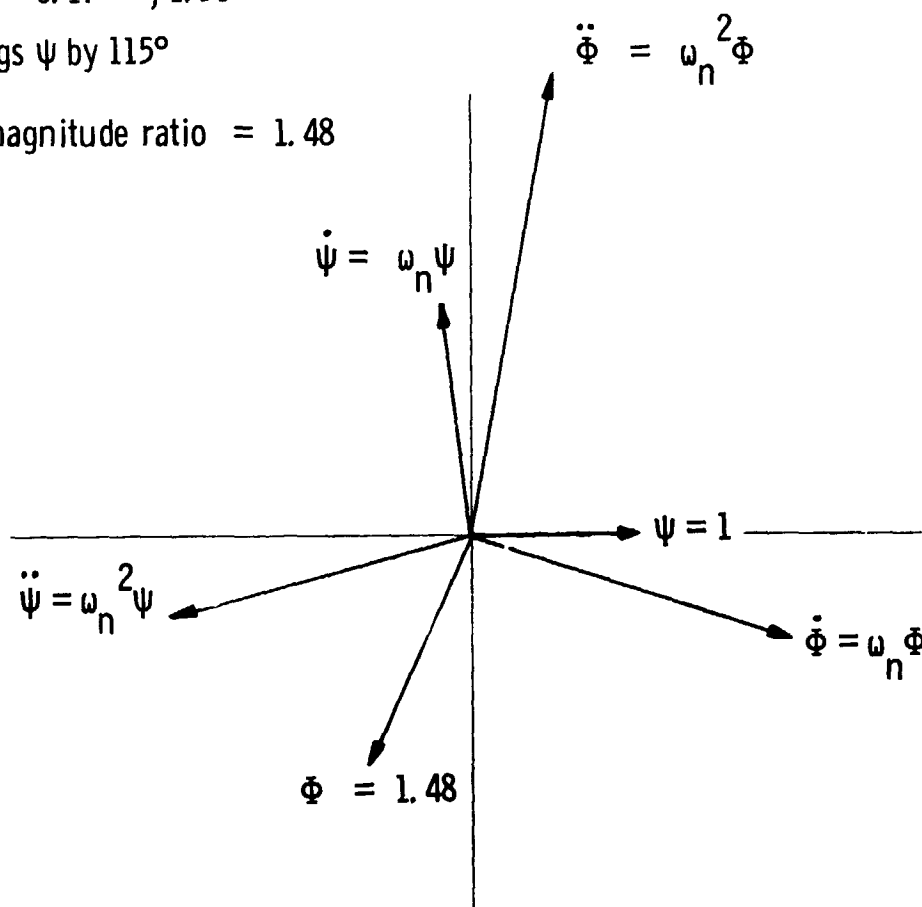


Figure 35.- Relationship between the  $\Phi$  and  $\psi$  time vectors and their derivatives for case 1.  $\theta = 0$ ,  $\beta.75R = 13.5^\circ$ ,  $\gamma = 0$ , and  $U_f = 17.6$  ft/sec.

Yaw moment equation:

$$\ddot{\psi} - N_{\dot{\psi}}\dot{\psi} - N_{\psi}\psi - N_{\dot{\phi}}\dot{\phi} - N_{\phi}\phi + \frac{P_{xz}}{I_z'}\ddot{\phi} = 0$$

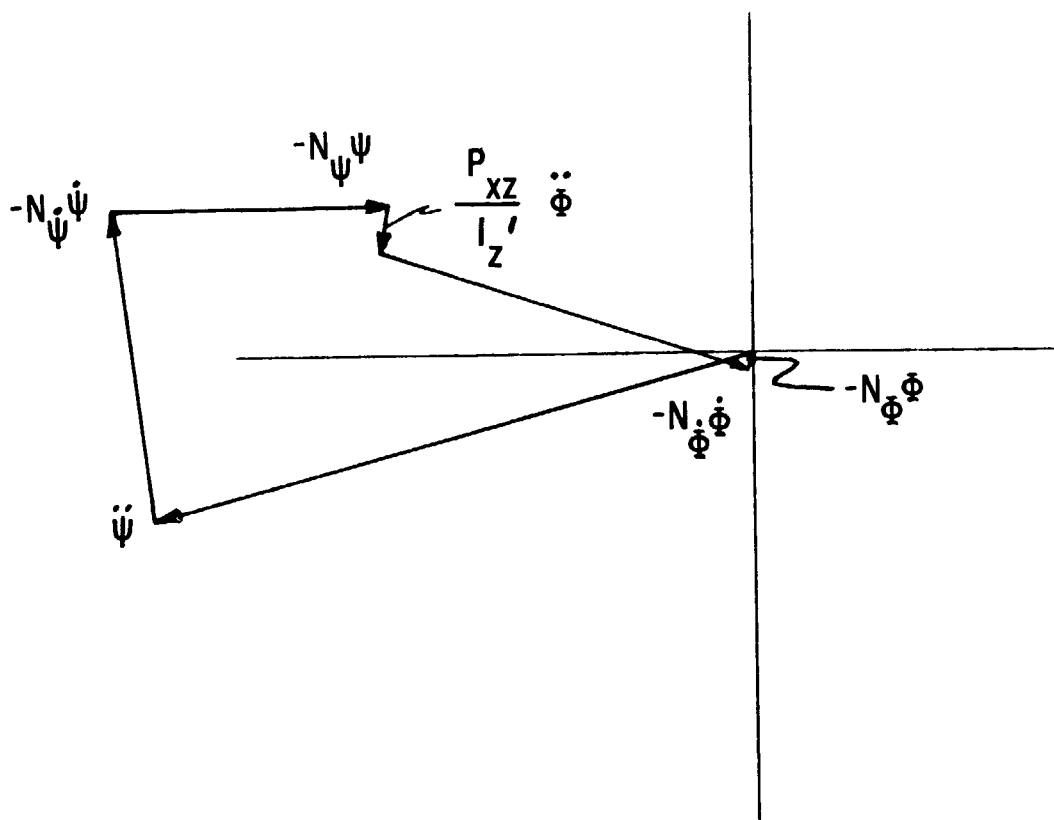


Figure 36.- Yawing moment vector polygon (Dutch-roll oscillation) representing two degrees-of-freedom ( $\phi$ - $\psi$ ) model data for case 1.  $\theta = 0$ ,  $\beta_{.75R} = 13.5^\circ$ ,  $\gamma = 0$ , and  $U_F = 17.6$  ft/sec.



Roll moment equation:

$$\ddot{\phi} - L_{\dot{\phi}} \dot{\phi} - L_{\dot{\psi}} \dot{\psi} - L_{\psi} \psi + \frac{P_{xz}}{I_x} \ddot{\psi} = 0$$

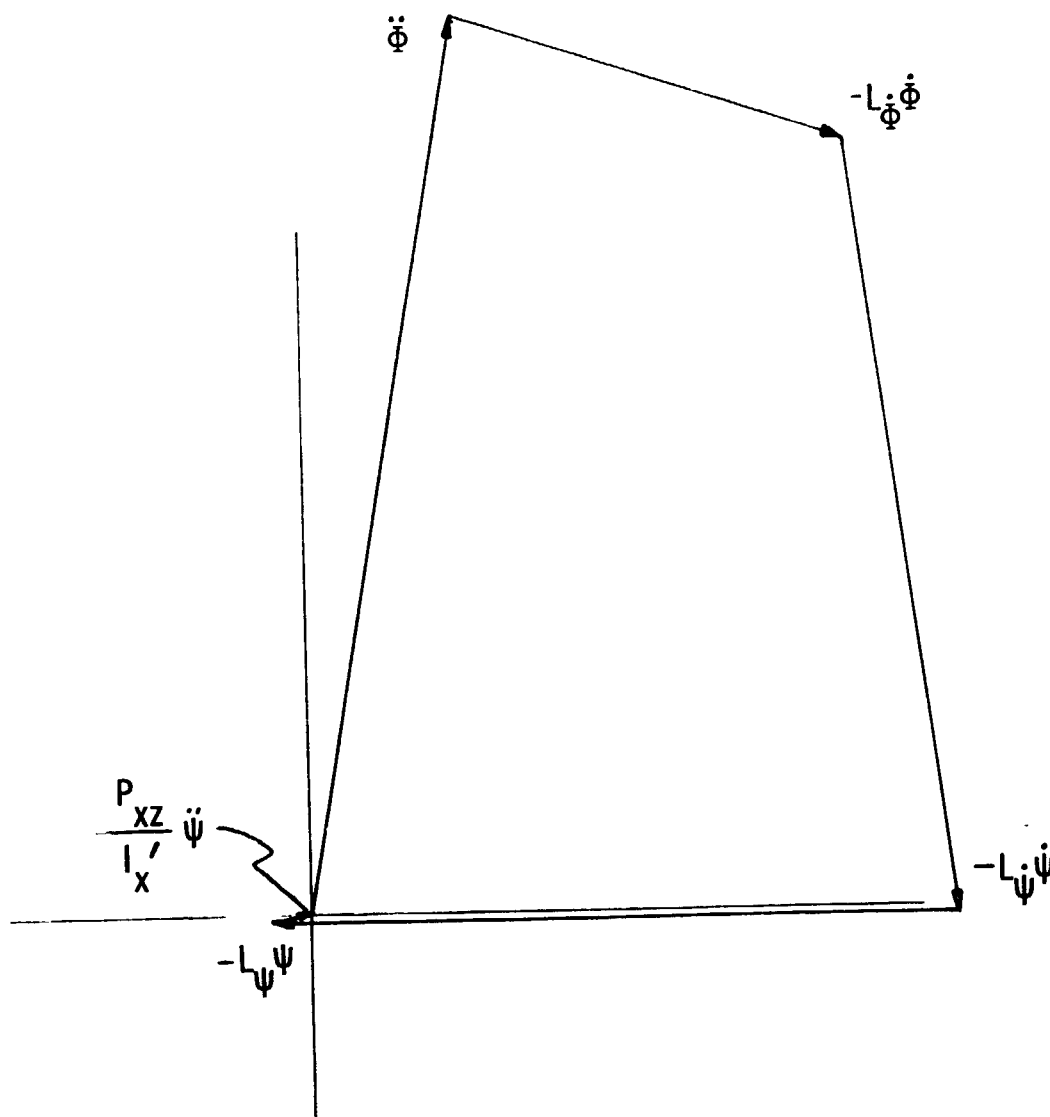


Figure 37.- Rolling moment vector polygon (Dutch-roll oscillation) representing two degrees-of-freedom ( $\phi$ - $\psi$ ) model data for case 1.  $\theta = 0$ ,  $\beta_{.75R} = 13.5^\circ$ ,  $\gamma = 0$ , and  $U_F = 17.6$  ft/sec.

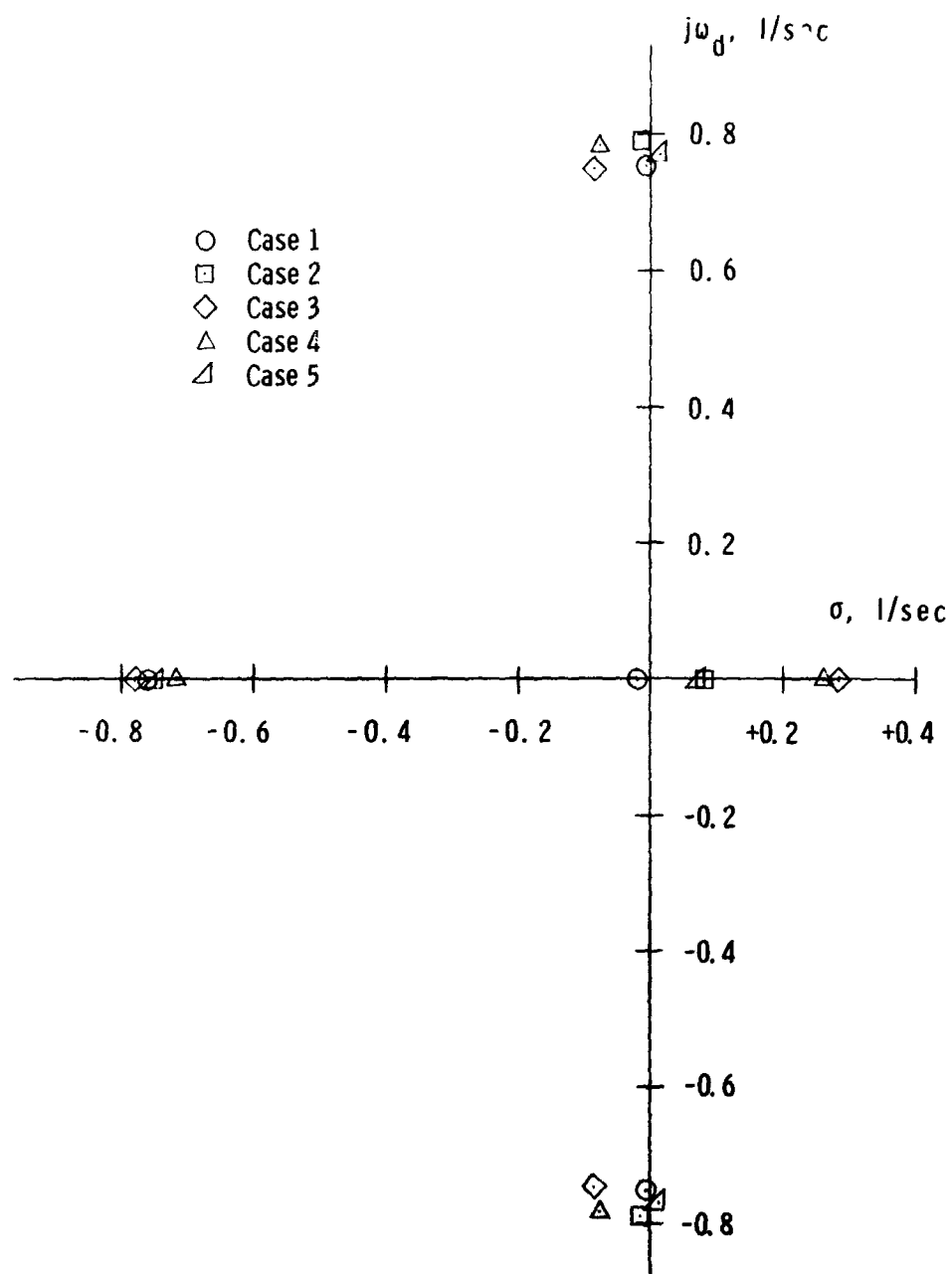


Figure 38.- Characteristic roots of the full-scale aircraft motion for each test case.